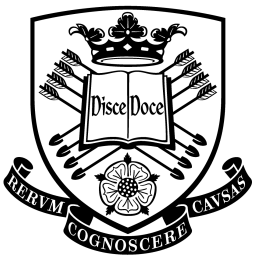

Using emerging technologies to reduce occupational radiation exposure in the ATLAS ID Decommissioning, and other high-radiation environments

Alice Margaret Cryer

October 2021

Acknowledgements

I would like to thank my supervisors Kristin Lohwasser and Hector Marin-Reyes for their guidance and support, as well as Richard French who supervised me for the first two years. Gabriel Kapellmann and Samantha Abrego for their invaluable support wrangling CAD models for the Virtual Reality Platform. Kirsty Veale and Martin Jaekel, our collaborators at ATLAS, and everyone at the Birmingham cyclotron for their help and support.

Abstract

Continuing to push back the frontiers of high energy physics requires colliders and detectors of increasing scale, operating at higher energies and intensities than ever before. The unavoidable byproduct of these experiments is an increase of radiation in the surrounding area. However, reliance on human interventions for such tasks is unsustainable and other methods must be investigated. This thesis will outline the use of emerging technologies to reduce occupational radiation exposure in the ATLAS ID Decommissioning, and other high-radiation environments. This work anticipated the addition of digital twins in the Virtual Reality Intervention Planning Platform; a benchmark radiation tolerance would provide users with a lifetime estimation useful for maintenance planning.

Table of Contents

List of Tables

List of Figures

Author Contribution

The Author's contribution to this work is set out in the final three chapters. A significant portion of the work was dedicated to creating the Virtual Reality Intervention Planning Platform: from the initial discussions to determine the scope of the project, its proof of concept and its application for creating dose estimates for the ATLAS ID decommissioning using motion capture. Separate research involving destructive radiation testing of a camera and a robotic manipulator are presented in the final chapter.

Declaration

I, the author, confirm that the Thesis is my own work. I am aware of the University's Guidance on the Use of Unfair Means. This work has not been previously been presented for an award at this, or any other, university.

1 Introduction

Continuing to push back the frontiers of high energy physics requires colliders and detectors of increasing scale, operating at higher energies and intensities than ever before. The unavoidable byproduct of these experiments is an increase of radiation in the surrounding area. Necessary maintenance and decommissioning work must be carried out on the machines within this hostile environment. However, reliance on human interventions for such tasks is unsustainable and other methods must be investigated.

The Organisation of European Nuclear Research, more commonly known as CERN, is the European particle physics laboratory located on the Franco-Swiss border between the city of Geneva and the Jura mountains. The organisation is made up of 23 member states, and collaborates with over 600 institutions worldwide. Cutting edge particle physics research is carried out at experiments across the CERN complex. The Large Hadron Collider (LHC), located at CERN, is the largest and highest energy proton/ion collider in the world. The ATLAS experiment at the LHC measures high energy collision and debris measured in detectors. Measuring tracks and closest to the collisions, with the harshest radiation exposure, is the Inner Detector (ID). It has received substantial radiation damage over the course of ATLAS operations; its technology has also deprecated during this time. The ID is planned to be replaced the start of the High Luminosity-LHC (HL-LHC), with the Inner Tracker (ITk), which is a new entirely silicon-based detector designed to operate within the higher radiation fluence of the HL-LHC operations. As the detector has been activated due to the incident radiation, its decommissioning needs to be carefully planned in order to avoid unnecessary and dangerous radiation exposure to the technicians carrying out the work.

Virtual Reality (VR) is an emerging technology that allows the user to disconnect from the physical world. This can be exploited to allow the exploration of hazardous environments with minimal risk. Base VR software often allows the addition of custom scripts, which add extra functionality for the user's needs. A virtual reality intervention planning platform was developed to reduce occupational radiation exposure in the ATLAS ID Decommissioning, and other high-radiation environments.

The thesis is structured as follows: This first chapter provides the introduces the context and motivation behind the work presented. The second chapter covers radiation interactions with matter. This starts with the theory and generalised cases of incident particles and the target material. From there, it reviews how incident radiation damages a silicon lattice - silicon being the main element used in the semiconductor sensors in the ATLAS detector systems. Following that is a subsection on radiation damage to living tissue. This explains how radiation affects living cells, the need for radiation protection protocols, and how CERN enacts radiation protection onsite.

The third chapter introduces the LHC, explaining how the collider works and the

motivation behind the planned upgrade to the HL-LHC. After that it will consider the ATLAS experiment in detail, with special attention to the ID and the mechanical structures of the experiment. It also covers the logistical aspects such as the detector's installation within the cavern, the different detector configurations for maintenance work, the rationale and plan for the ID decommissioning, and the method employed to estimate radiation levels for interventions.

The fourth chapter defines virtual reality in the context of this work. What is considered virtual reality, what is required for virtual reality to be effective, and the 'industry standards' that have been established in the field. This chapter also introduces the base software used for the Virtual Reality Intervention Planning Platform - Virtalis Visionary Render - its capabilities, and its strengths and weaknesses.

The fifth chapter covers the creation and proof of concept of a Virtual Reality Intervention Planning Platform for radiation dose estimation and intervention planning. It presents the conception and design of the platform, including the virtual dosimeters which track the users' doses in real time as they explore the virtual environment.

The sixth chapter goes over the addition of motion capture to the system. Motion capture was used to track a technician performing decommissioning tasks on an accurate Mock-up of the ID. This new location data provides an in-depth insight into the movements required to remove sections of the ID. This new angle complements the extant system; the results of the animated avatar's radiation exposure were returned to the ATLAS Inner Detector decommissioning group.

The seventh chapter comprises of the irradiation of a robotic manipulator and camera. This work was in preparation for digital twins to be included in the Virtual Reality platform; a benchmark radiation tolerance would provide users with a lifetime estimation useful for maintenance planning.

The eighth chapter provides a summary of the work, and is followed by the bibliography.

2 Radiation Interaction with Matter

This chapter will discuss the main mechanisms governing radiation-matter interactions, what effect these have on High Energy Physics experiments, and living tissue.

2.1 Particle interaction with matter

Radiation is a catch all term for any freely moving subatomic particle that can transfer energy to some recipient matter. Neutrinos will not be considered radiation in this work because they interact so rarely. Radiation types can be broadly categorised as:

- Heavy charged particles, eg. protons
- Light charged particles, eg. freely moving electrons
- High energy photons, eg. X-rays, Gamma rays
- Neutrons
- Other

2.1.1 Massive charged particle interactions

The manner in which incident radiation interacts with matter depends on the radiation's properties and its momentum, as well as the target material. For massive charged particles there are three main mechanisms for energy loss, and the dominant mechanism is dependant on the momentum of the incident particle. For particles with insufficient energy to ionise the target material, inelastic collisions with the target material will cause thermal excitation. For higher energy particles, ionisation and Bremsstrahlung losses (photons emitted when a charged particle is submitted to negative acceleration) dominate. In this energy domain, the energy loss per unit length, dE/dx, can be described by the Bethe-Bloch stopping power formula, shown in Equation 1.

$$-\left(\frac{dE}{dx}\right) = K\rho\frac{Z}{A}\frac{z^2}{\beta^2}\left[\frac{1}{2}\ln\frac{2m_ec^2\beta^2\gamma^2T_{max}}{I^2} - \beta^2 - \frac{\delta(\beta\gamma)}{2}\right] \tag{1}$$

where the parameters are as follows:

- $\boldsymbol{dE/dx}$ is the energy lost by the incident particle per unit length of absorbing material.
- $\boldsymbol{K} = 4\pi N_A r_e^2 m_e c^2 = 0.307 MeV g^{-1} cm^2$, where $\boldsymbol{N_A}$ is Avogardo's number, $\boldsymbol{r_e}$ is the classical radius of an electron.
- $\boldsymbol{z}$ charge of incident particle in natural units

- $\boldsymbol{\rho}$ is the density of the absorbing material
- $\boldsymbol{Z}$ is the atomic number of the absorbing material
- $\boldsymbol{A}$ is the relative atomic mass of absorbing material
- $\boldsymbol{m_e}$ is the mass of an electron
- $\boldsymbol{\beta}$ velocity of the incident particle in natural units
- $\boldsymbol{\gamma} = 1/\sqrt{1-\beta^2}$
- $\boldsymbol{T_{max}}$ is the maximum kinetic energy transfer in a single collision
- $\boldsymbol{I}$ mean excitation energy of the absorbing material
- $\boldsymbol{\delta(\beta\gamma)}$ density effect correction

The equation shows that the stopping power is dependant on the incident material via the Z/A term, however it does not depend on the mass of the incoming particle, only its charge. The mechanism of energy loss is in the Beth-Bloch range, where the incident particle has momentum between $0.1 < \beta\gamma < 500$. The incident particle loses kinetic energy by ionising atoms in the target material [1]. Bethe-Bloch is the only region where a material's stopping power is not dependant on the mass of the incident particle.

Particles at $\beta\gamma \approx 3.5$ are called minimum ionising particles. The rise following the minimum is due the increase in energy transferred to the material due to the effect of relativistic distortions in the electrostatic field of the incoming particle [1]. This levels off at higher momentum due to the density effect - where atoms in the path of the incoming particle will polarise, reducing the electrostatic field acting on the material's electrons and therefore the amount of energy lost [2]. The stopping power increases steeply once a charged particle energy falls below the minimum ionisation. In this energy range, knowing the energy of the incident particle is important in determining how far the particle will penetrate the target medium.

Fig. 1 shows the idealised case of anti-muons and copper. Anti-muons are used as they can demonstrate the energy loss mechanisms for heavy charged particles without other interactions with the target material. At $\beta\gamma > 500$, radiative losses from Bremsstrahlung photon emission become the dominating cause of energy loss of an incoming particle. This is where a charged particle is subjected to an acceleration by passing through an electric or magnetic field. The change in its kinetic energy is emitted as a photon.

Electrons are light charged particles, and have a higher charge-to-mass ratio than heavy charged particles. For electrons, Bremsstrahlung radiation dominates from much lower energies than their heavier counterparts, shown in Fig. 2.

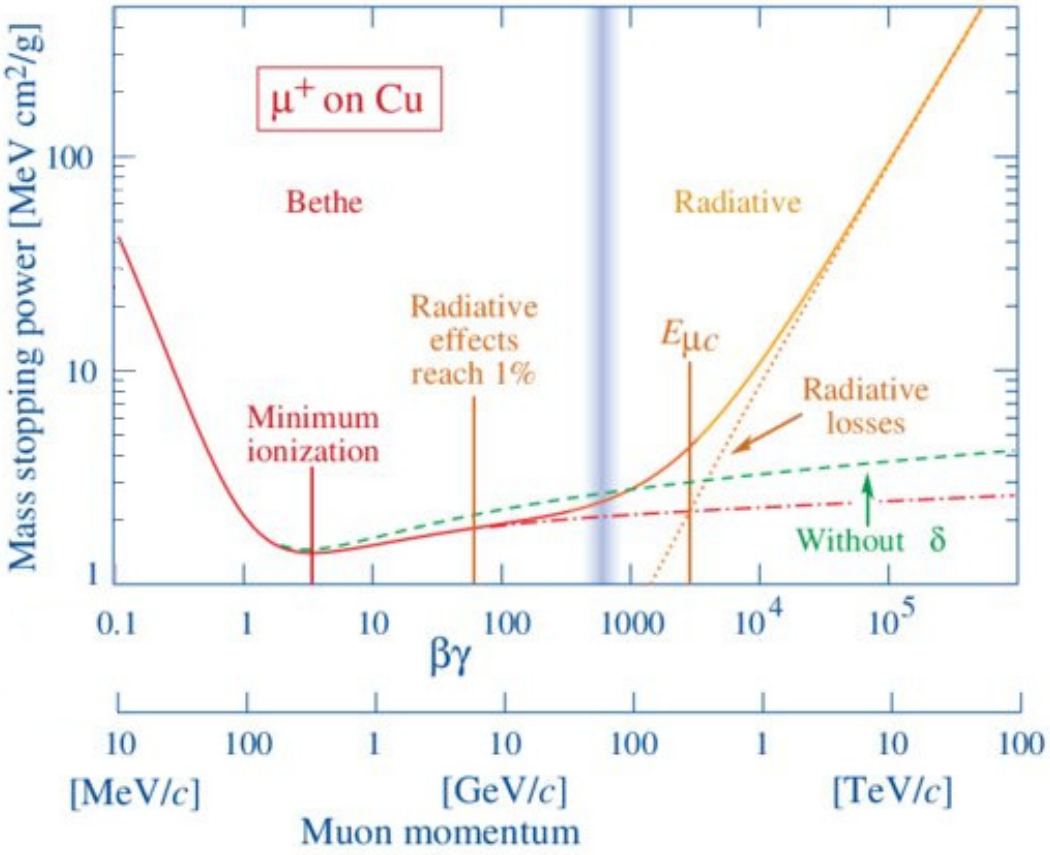

Figure 1: The stopping power of Cu for anti-muons, showing how the different terms of the Bethe Bloch formula dominate at different momenta. The graph covers the Bethe-Bloch and Radiative momentum ranges. Adapted from [3]

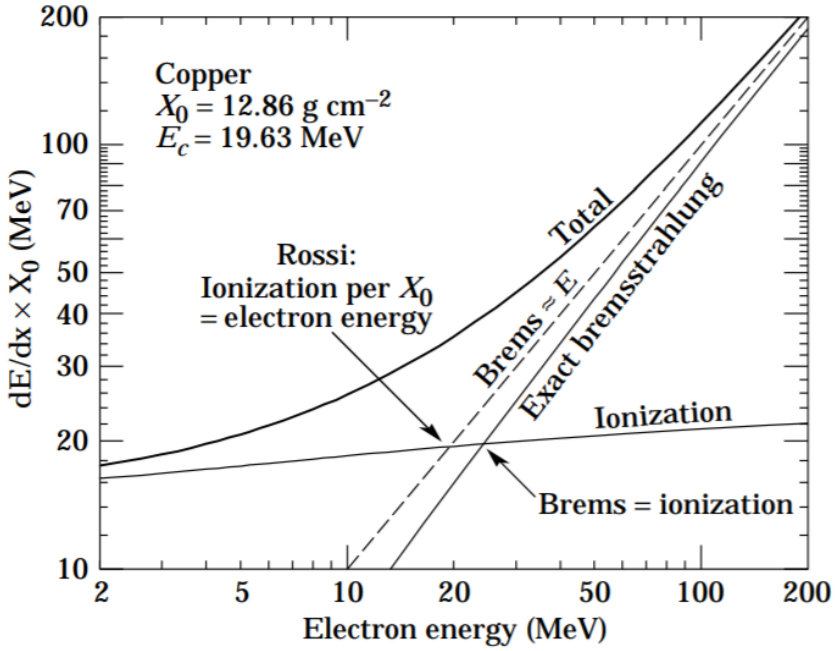

Figure 2: The stopping power of Cu for electrons, from [3]

2.1.2 Nucleon nuclear interactions

Neutrons can penetrate further than other radiation types due to their neutral charge, as they do not interact via the electromagnetic force and do not emit Bremsstrahlung radiation.

Fig. 3 shows the possible interactions between that occur when a neutron comes in contact with an atomic nucleus [4]:

- Elastic scattering: where the incident neutron transfers its kinetic energy to the target nucleus without exciting it. This is a common interaction between low-Z materials and fast neutrons.
- Inelastic scattering: where the incident neutron transfers some of its kinetic energy to the target nucleus and excites it. A gamma ray is produced when the target nucleus decays back to its ground state.
- Transmutation: where the incident neutron is absorbed by the target nucleus. As a result, the unstable nucleus ejects either a proton or a helium nucleus. This means the atom changes element.
- Radiative capture: The incident neutron is absorbed by the target nucleus, which is then excited. A gamma ray is produced when the target nucleus decays back to its ground state.

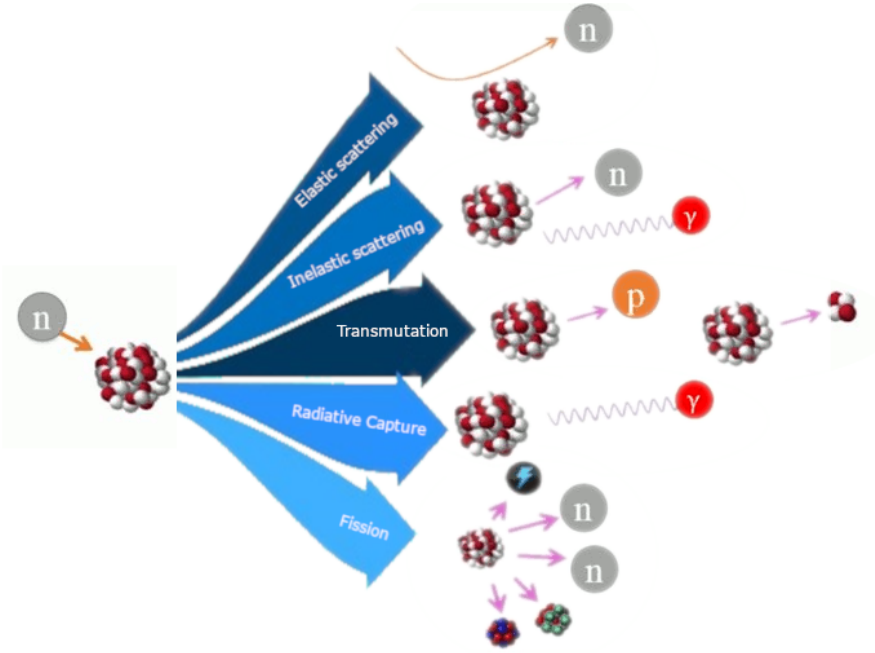

Figure 3: Neutron interactions with matter, adapted from [4]

- Fission: Fission can occur spontaneously for high-Z materials and thermal neutrons, however the cross section is small. Fission occurs when an atomic nucleus splits into two daughter elements (fission products), and releases free neutrons. Unlike transmutation, the daughter elements of fission interactions are of roughly equal mass. Neutron bombardment can induce fission when the incident neutron excites the nucleus and overcomes the fission barrier, the minimum energy required for the nucleus to split.

All interactions above, except elastic collision between an incident neutron and the target atomic nuclei, create an excited 'compound nucleus' which is inherently unstable. The timing of the 'de-excitation' to its ground state is variable. Depending on the type of interaction, the compound nucleus falling back to its ground state can emit gamma rays, neutrons, helium nuclei or electrons. These non-elastic interactions induce radioactivity in the target material. This is also known as neutron activation, where the target material is made radioactive, or 'activated' by the incident neutrons. The cross section of neutron interactions means that activation is energy dependent. The daughter products emitted as the nucleus falls back to its ground state will go on to interact with other nuclei, creating interaction chains.

The half-life of neutron activation depends on the activated material, and the decay has a distinct signature such that neutron activation analysis is used to identify element concentrations in a sample. For example, ^{30}Si(n,γ)^{31}Si has a half-life of 157 min, and emits a

gamma ray of 1.2 MeV as it decays [5], [6].

Spallation occurs when an energetic heavy charged particle - commonly a proton - splits an atomic nucleus, releasing neutrons, protons and light nuclei. Because of this, spallation is exploited to create neutron beams for particle experiments called spallation neutron sources. The effect of the spallation mechanism sounds similar to fission, however any nucleus can be subjected to spallation. The process is driven by the energy of the incident charged particle, usually around 1 GeV [7] - this is much more energetic than thermal neutrons in fission interactions.

2.1.3 Electromagnetic radiation interactions

Photons passing through a medium will interact in three different ways:

- Photoelectric effect
- Compton scattering
- Pair production

The Photoelectric effect occurs when the incident photon energy is greater than the target material's electron binding energy. As a result, the photon is absorbed by the target, and an electron is emitted. The Photoelectric effect dominates for higher Z materials or low energy photons, which is why lead (Z=82) is used in gamma ray shielding.

Compton scattering is an inelastic collision, where an incident photon is scattered by a charged particle, more commonly outer shell electrons. The probability of Compton scattering in a material depends on the electron density which is proportional to Z/A, and varies with photon energy. The amount of energy the photon loses in the scattering depends on the scattering angle.

Photons with energy greater than 1.022 MeV can undergo pair production, where the photon decays into a electron-positron pair. Due to the conservation of momentum, this process can only occur when the photon is in proximity to matter. The positron will annihilate with an electron, releasing two gamma rays at 0.511 MeV, which may then interact further in the material.

Unlike particle beams, photons do not deposit energy gradually as they pass through matter so they do not have a defined stopping distance like massive particles. However, the intensity of a photon beam will be attenuated while traversing the irradiated medium as individual photons interact. High energy gamma rays are highly penetrative; they are not charged particles. Fig. 4 shows that photons are more likely to interact at low energy.

It is not always the incident radiation that does the most damage to a material, but the dispersion of secondary particles following the primary interaction. Such particles include

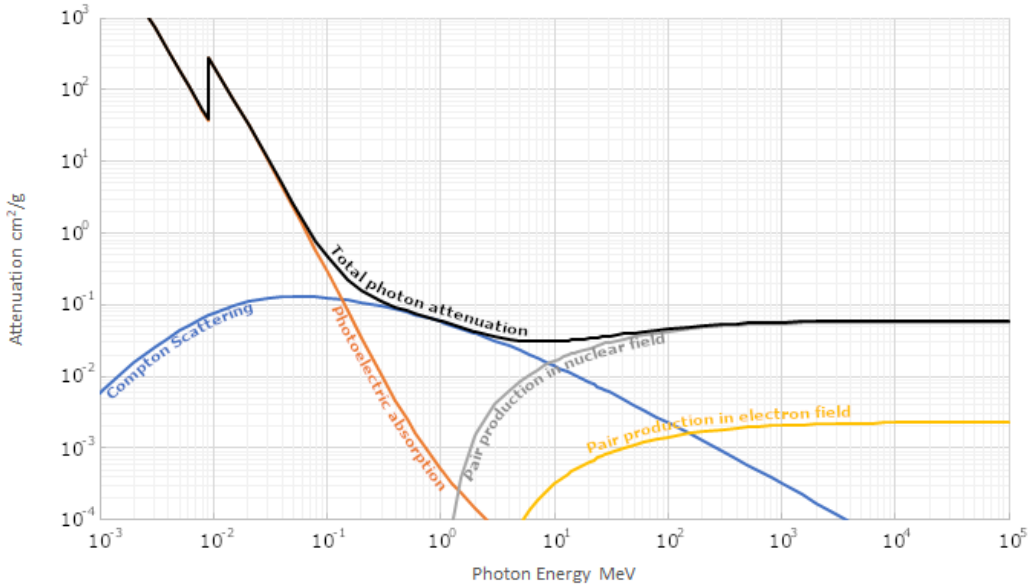

Figure 4: Photon attenuation in Cu, data from NIST XCOM database [8]

ionised electrons, photons emitted through Bremsstrahlung, or particles produced through neutron interactions. For neutron spallation sources, creating these secondary particles is the objective. However, in other cases, these "knock-on" particles are unwanted and will continue onto interact with the surrounding matter. At high energies these can create chains of secondary interactions. The energy deposited by radiation from interactions with matter can cause changes to the interacting material and ultimately damage it.

The initial particle collisions inside the ATLAS detector are very high energy. The energy is rapidly dispersed, either directly deposited into the detector material, or through particle decays. Figure 5 shows the spectra of particle fluences by kinetic energy for —z— $\approx$ 50 cm and r $\approx$ 10 cm point in the ATLAS Cavern. A significant portion of the particle fluence through the detector are charged particles. However, only hours after a high-luminosity[i] run, the background radiation is a mixed radiation field composed of 80% neutral components (n, γ, etc) and 20% charged particles [10]. Without the continual particle fluence from the high energy collisions, the background radiation in the ATLAS cavern reduces significantly over time, and the remaining radiation is the afterglow from the activated detector components.

2.2 Silicon detector physics

This section will explore how an ideal silicon-based particle detector works. It will review what semiconductors are, why their use is favourable for electronics in general, what is special about PN junctions, and how these are used in silicon sensors.

[i]Luminosity will be explored in chapter 3.1

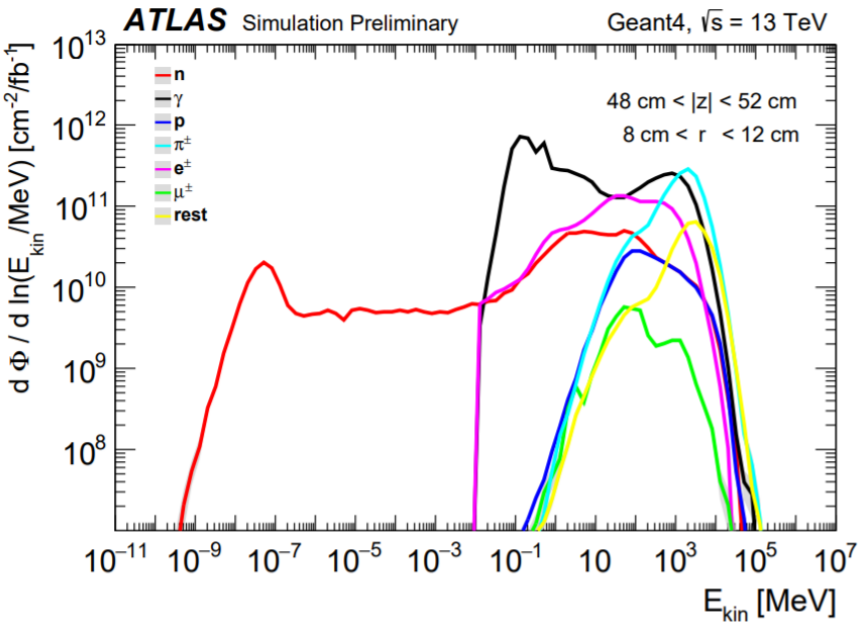

Figure 5: Particle fluences as a function of their kinetic energy. The simulation of the ATLAS detector was run in GEANT4 with parameters typical for Run-2 at $\sqrt{s} = 13$ TeV. The neutron fluence is shown from $E > 10^{-11}$ MeV, other particle spectra start from 10^{-2} MeV. The spectra correspond to a location in space inside the inner detector, at —z— ≈ 50 cm and r ≈ 10 cm. The grey bands indicate statistical uncertainties. Taken from [9]

Quantum theory states that electrons around a nucleus can only occupy discrete energy levels. The energy bands closest to the nucleus are all filled by electrons, while those at the highest energies are empty. The electric conductivity of a material is determined by the properties of the two energy bands at the limit of electron occupation - the valence band and the conduction bands. At Absolute zero, all the electrons are in the lowest possible energy configuration. In this case, the valence band is the highest energy level that is still occupied by electrons and the conduction band is one level higher and is the lowest energy band that is unoccupied. Since electrons can only occupy discrete energy levels, the difference in energy between the conduction and valence bands can be determined. This is called the "band gap".

A material is an electrical insulator if the band gap is large enough that thermal energy would be insufficient to excite electrons from the valence band to the conduction band. By contrast, an electrical conductor has no band gap, because the conduction band and the valence band overlap. For electrical conductors, exciting electrons into the conduction band requires minimal energy expenditure and can be achieved through thermal excitation alone. Semiconductors exist in the middle-ground between insulator and conductor. The conduction and valence bands are separate, however their band gap is not as significant as for insulators. Thermal energy is enough to excite some electrons to the conduction band.

Silicon has a favourable band gap for electronics (E=1.124 eV), which can be modified with dopants. It is an abundant element, and its oxide SiO_2 is naturally occurring. The silicon lattice is held together using covalent bonds. These bonds occur ideally between elements that are both close together on the periodic table and non-metals.

Silicon on its own is an electronic insulator. Adding doping elements increases the number of free electrons (donors), or free 'holes' (acceptors), depending on their own intrinsic properties. Holes are the 'missing' electrons from the atomic shells. Holes are an imaginary construct, as it is easier to conceptualise pseudo positive particles moving to pair up with electrons, than the shifting of electrons through a crystal lattice, repulsed by the excess of free electrons from the other side of the junction.

PN junctions are crucial building blocks to most electronic systems. By definition, PN junctions are the juxtaposition of a P-type doped semiconductor and an N-type doped semiconductor. At the interface, the surface holes of the positive P-type semiconductor pair up with the surface electrons in the negative N-type semiconductor. This creates a neutral zone at the interface of the two lattices, called the depletion region, with no free moving charge carriers.

There are three options using a PN junction, depending on how the voltage across the junction is applied, called bias:

- **No voltage across the junction / no bias:** Some charge carriers may cross the depletion region, and the amount depends on temperature (thermal recombination).

However there is no current flow as the junction is not connected to a circuit.

- **Positive bias:** The PN junction is said to be in positive bias when the voltage across it reduces the energy required for electrons to cross the band gap. If the bias voltage is more than the band-gap potential, the charge carriers get pushed across the depletion region, allowing current to flow. This is accomplished by connecting the negative voltage to the N-region and positive voltage to the P-region.

- **Reverse bias:** The PN junction is said to be in reverse bias when the electric potential increases the energy required to cross the band gap. This is accomplished by connecting the positive voltage to the N-region and negative voltage to the P-region. The inverse voltage carries excess electrons away from the lattice and recombines holes with electrons. The result increases the depletion region and the band-gap potential. An electric field forms across the depletion region of a PN junction in reverse bias, and there is a negligible current flow which is known as the leakage current. The depletion breakdown voltage, or just depletion voltage, is the limit at which the PN junction will start to markedly conduct in reverse.

In an unbiased PN junction, a particle passing through generates circa 10^4 electrons, compared to the 10^8 free charges in the lattice [11][ii]. Therefore the number of free charge carriers must be artificially decreased for a signal to be significant and measurable. This can be achieved by cooling the lattice - impractical for large detectors - or by using the PN junction in reverse bias. A PN junction in reverse bias has large depletion region with no free moving particles, and an electric field across it. As a particle travels through the junction, it deposits kinetic energy creating electron-hole pairs - either directly ionising atoms, or indirectly with ionising photons emitted from Bremsstrahlung. These ionised particles do not recombine, as the E field across the depletion region forces the opposing charges to separate and drift to opposite sides of the junction. These charges are detectable as a spike in electric current; a signal for every ionising particle that passes through the junction [12]. The two types of silicon detectors used in the ATLAS ID and relevant to this work are Pixel and Strip detectors: Pixel sensors are arranged in a 2D array, and the charge of an incident particle is collected within an area of 1mm^2 or smaller. A pixel typical pixel sensor includes 2800 channels [11]. Since pixels provide the highest granularity [13], they are used where there is the highest density of charged particles, which is the detectors closest to the interaction point. While the principle of a depleted PN junction used for both pixel and strip detectors, silicon strip sensors differ geometrically from pixel sensors. In Strip detectors, and the sensing area is an approximate 1D strip (16 μm wide for the sensors in the SCT in the ATLAS ID [14]). Data on the second

[ii]These are representative numbers of room-temperature undepleted silicon, the actual numbers would be dependant on the specific properties of the sensor

dimension is facilitated by juxtaposing the strip detectors with different orientations [15]. Strip sensors typically require between 500 to 800 channels [11].

Charge collection efficiency (CCE) is the term for the ratio between the detected collected charge and the idealised (theoretical) collected charge from an incident particle. The ideal value is 1.0. A decrease in CCE is a good indication of radiation damage to the silicon lattice. A signal can cross the width of a sensor, 300 μm, in 8 ns if the charges are unimpeded [11].

This chapter presented the ideal case for silicon particle detectors. However, when particles interact with the detector outside of the depletion region, it can cause damage to the silicon crystal lattice which has knock-on effects to the detector itself.

2.3 Radiation Damage to Silicon-based High Energy Physics detectors

Particle interactions are desired inside particle detectors. However, in silicon-based detectors, a particle only creates a signal within the depletion region of a PN junction. An incident particle deposits enough energy for electrons in the lattice to cross the band-gap from the valence to the conduction band - creating electron-hole pairs in the PN junction's depletion region. The electric field across the junction exerts a force on the electrons, causing them to cross the depletion region. This electric current is the particle's signal. Other interactions of an incident particle with the bulk detector material can cause structural defects in the silicon crystal lattice. These defects have knock-on effects with charge creation and carrier mobility, which interferes with signal detection.

Radiation damage is usually categorised by the charge of the incident particle: Ionising radiation (Total Ionizing Dose), from charged particle interactions, and Non-Ionising radiation (Non-Ionising Energy Loss) from neutral particle interactions. This section will discuss firstly how silicon sensors are used to detect sub-atomic particles, secondly how both ionising and non-ionising radiation damage the silicon sensors inside a particle detector, and finally the knock-on effect on the detector's functionality. This feeds into the motivation for this work: why the ATLAS Inner Detector needs upgrading.

2.3.1 Effect of radiation on silicon sensors

Non-Ionising and Ionising radiation damages silicon sensors in different ways. Bulk damage to the silicon lattice is caused by Non-Ionising Energy Loss (NIEL), while ionising radiation damages the lattice surface.

2.3.1.1 Damage caused by Non-Ionising Energy Loss

NIEL damage occurs when there is the transfer of energy and momentum to the nuclei of the semiconductor lattice from incident radiation. It encompasses both: the immediate damage from the ballistic kinetic energy transferred from the incident particle directly to the silicon

lattice, as well as the damage caused indirectly from the ensuing annealing process. The annealing process refers to the mobility and transformation of radiation-caused defects in the silicon lattice. These can lead to spontaneous repairs, or exacerbation of the damage [16].

Microscopically, direct NIEL damage occurs when an elastic collision from an incoming particle displaces an atom from its normal lattice position. The ejected atom is known as a primary knock-on, which, with enough energy, may cause a cascade of atomic displacements before eventually coming to rest. This creates vacancies in the formerly occupied space; and interstitial atoms, where the displaced atoms occupy a space outside normal lattice positioning. Some simple point defects are illustrated in Fig. 6. This stochastic process can result in many different complex changes to the lattice structure: A short-distance interstitial-vacancy defect is called a Frenkel pair. Di-vacancies V_2 and triple vacancies V_3 are vacancies left by the displacement of multiple adjacent atoms. Di-interstitials are two adjacent interstitial atoms. Silicon is a very reactive element. Interstitial silicon atoms can bond with impurities, creating molecules with different energy states, or impurities can fall into silicon vacancies, changing their properties as a dopant [12].

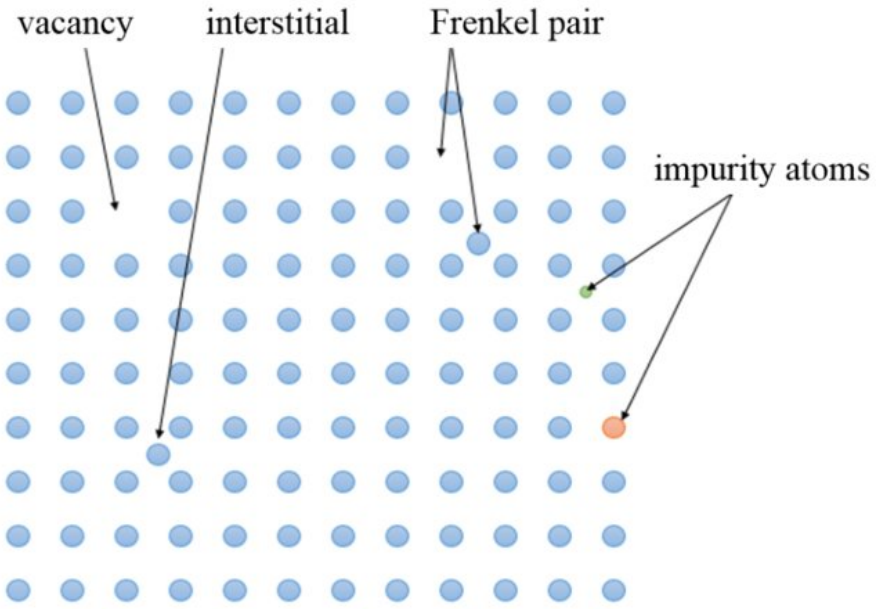

Figure 6: A schematic representation of Vacancy, Interstitial, Frenkel pair, and impurity point defects in a crystal lattice, from [4]

These microscopic defects distort the lattice structure, generating new energy levels within the band-gap. As they build up through continuous radiation bombardment, signal electrons increasingly struggle to dissimulate effectively through the sensor. This shifts the macroscopic properties of the sensor, affecting the depletion voltage, leakage current and charge collection efficiency (see chap- 2.2).

The annealing process diffuses defects within the lattice. This is dependant on temperature. Diffusion of interstitials and vacancies through the lattice is favourable at T > 150 K. Annealing can be beneficial; Frenkel pair recombination is an example where the lattice is repaired spontaneously through annealing. This effect can be exploited, as Frenkel pair defects are short-range and very mobile, meaning recombination happens within a short time frame. Complex defects are less likely to anneal advantageously (similarly, a bone knitting together without a splint is unlikely to be set correctly). The movements of particle defects through a lattice is temperature dependant, and larger and more complicated defects have a slower rate of diffusion. The propagation of such complex defects can be 'frozen out' by cooling the lattice, preventing further damage and mitigating the evolution of the sensor's properties [12].

NIEL damage is normally expressed in 1 MeV neutron equivalent (neq) fluence, where fluence is a flux of particles. 1 MeV neq fluence (Si) is a comparison unit, here relating specifically to Silicon. The unit equates an arbitrary particle fluence with the fluence of 1 MeV neutrons required to cause the same amount of damage.

2.3.1.2 Ionising radiation

Ionising radiation damage causes damage to the surface of a silicon sensor, i.e. damage to the oxidised SiO_2 layer or the Si-SiO_2 interface. Total Ionising Dose (TID) is the total accumulated amount of absorbed ionising radiation specified at a particular dose rate exposure at +25°C. As SiO_2 is an electric insulator, the creation of electron-hole pairs is not always reversible. Electrons in SiO_2 are very mobile, and quickly move from the oxide layer. Holes diffuse slower, and remain trapped at the Si-SiO_2 interface, creating a layer of charge. In some cases the holes will generate traps for electrons in the Si layer. This increases the band voltage, while increasing the inter-strip capacitance and decreasing the inter-strip resistance [12]. TID is measured in Grays (Gy), the derived SI unit for absorbed ionising radiation, which in base SI units is 1 Gy = 1 J/kg, 1 Joule per kilogram of absorbing material.

2.3.2 Macroscopic effect of radiation damage on the particle detector

Radiation damage to a particle detector is predominantly inflicted by non-ionising radiation. Displacement damage is the catch-all term for cumulative long-term NIEL damage, and is characterised as product of the NIEL damage from a particle and its fluence. It is quantified by comparing the damage to a known quantity - in the case of silicon-based detectors, this comparison is to 1 MeV neutron equivalent fluence (Si), the damage caused by 1 MeV neutrons on a silicon lattice. The displacement damage is the summation of the products of each incident particle fluence and the NIEL damage they caused. Displacement damage refers to three important changes to the silicon sensor parameters in the detector [12], [17], [18]:

- The removal of doping impurities, by creating complex molecules or by filling vacancies, changes the effective doping density of the P- and N-type semiconductors. This changes the depletion voltage - the voltage at which the PN junction is fully depleted and therefore in reverse bias. The maximum depletion voltage is limited by breakdown, where current flows across the depletion region while the PN junction is in reverse bias.

- The formation of mid-gap states within the band-gap act like stepping stones, facilitating the movement of electrons across the depletion region. This leads to increased leakage current across the depletion region of the reverse-bias PN junctions. This causes noise in the detector and lowers the signal-to-noise ratio, making signals harder to detect.

- The formation of energy levels close to the edge of the band-gap allow charge trapping. After an event, instead of reaching the valence or conduction band, a signal charge is held in this intermediate energy level. The depletion region has few free charge carriers, so this signal charge can be trapped longer than the sensor read-out time, meaning the signal is not measured. This changes the charge collection efficiency of the sensor, as the overall size of the signal seen by the detector is reduced.

Displacement damage deteriorates the performance of a silicon detector depending on the accumulated NIEL damage, which is correlated to the duration of the detector's operation. Shifting the characteristics of the silicon sensors causes the larger particle detector to become less efficient. Therefore, the effect displacement damage has on the characteristics of a silicon sensor has been the focus of many studies.

There are two prominent models for estimating how radiation damage affects ATLAS silicon sensors: the Hamburg Model [19] and the Sheffield-Harper Model [20]. Using these models, it is possible to predict the evolution in sensor characteristics. Eventually, the silicon lattice in the sensors will be too damaged for the sensor to function. The progressive radiation damage to the silicon sensors was accounted for in the ATLAS detector specification and design parameters. Before their installation, sensors were tested to characterise their functionality over the experiment's expected lifetime particle fluence. This was crucial to guarantee that radiation damage did not become a significant issue to the detector performance over time [21]. However, the HL-LHC upgrade (see chap 3.1) will significantly increase the particle fluence through the detector - and the ID was not designed to meet these new requirements. As the ID has reached the end of its expected lifetime and has already incurred significant radiation damage, it is unsuitable for future operations in the HL-LHC and must therefore be upgraded.

In Fig. 7, the average leakage current of the ATLAS Pixel Modules as measured during 2010-2012 data taking is shown as a function of integrated luminosity - accumulated data and thus radiation fluence, see section 3.1 - and compared to predictions from the Hamburg Model. This clearly shows the correlation between radiation fluence and damage to the detector.

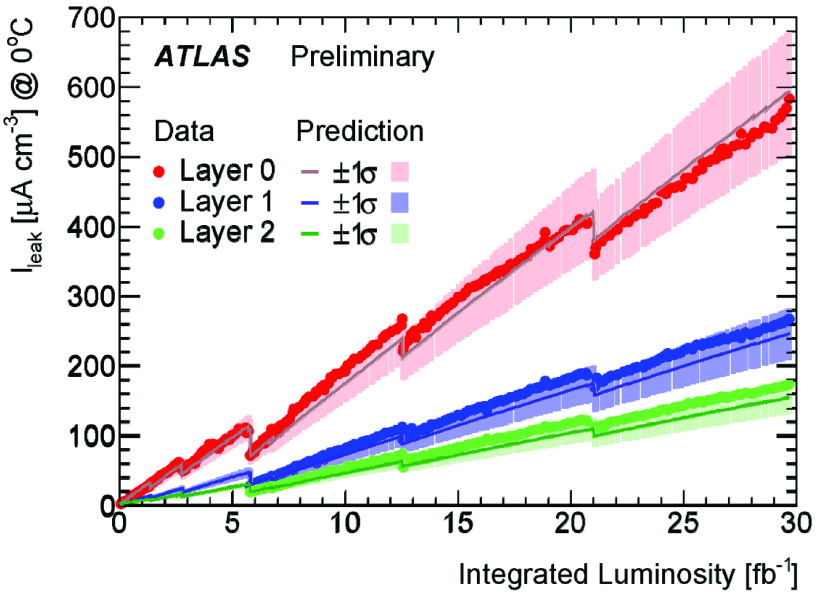

Figure 7: ATLAS Pixel Module Leakage current as a function of integrated LHC luminosity. Prediction lines based on the Hamburg model are included. Discontinuities are a result of annealing during the LHC cooling shutdowns [22]

An increase in leakage current increases the background noise and worsens the detector's the signal-to-noise ratio. The leakage current scales with radiation fluence. As the radiation damage to the detector increases, the leakage current also increases. The flow of electricity through the detector is partially dissipated as heat. Resistivity is temperature dependant, so the thermal energy (as excited electrons in the silicon lattice) facilitates more leakage current to flow through the junction. A certain amount of excess heat is can be managed by the ATLAS cooling system and cryogenics, however this is not a permanent solution as the radiation fluence and therefore leakage current will only increase while the detector is operating. Eventually the excess heat will exceed the capabilities of the cooling system, leading to a positive feedback loop of current begetting heat begetting current. This is called thermal runaway. As the end of the cycle is often the destruction of the component, the anticipated onset of thermal runaway is one of the decisive factors determining a silicon detector's lifetime.

Defects within the silicon lattice caused by radiation damage can act as acceptors or donors. This causes a change in effective doping concentration which is proportional to the radiation fluence. N-type silicon is susceptible to the creation of excess acceptors, leading to type inversion where it becomes p-type silicon [23]. Fig. 8 shows the evolution of the IBL's depletion voltage over the detector's operation, from its installation, until the end of

2016. The black curve is the Hamburg model simulation of the parameter's evolution. The measurements of the depletion voltage using the bias voltage scan method largely agree with the simulation. The graph shows the sensors undergoing type inversion [24], and causes the full depletion voltage of the sensor to increase.

In order to keep the detector sensitive, the voltage applied to the sensors must be increased to maintain the depletion region. This limits the detector's lifetime as the depletion voltage cannot be increased beyond the breakdown voltage of the sensor [23].

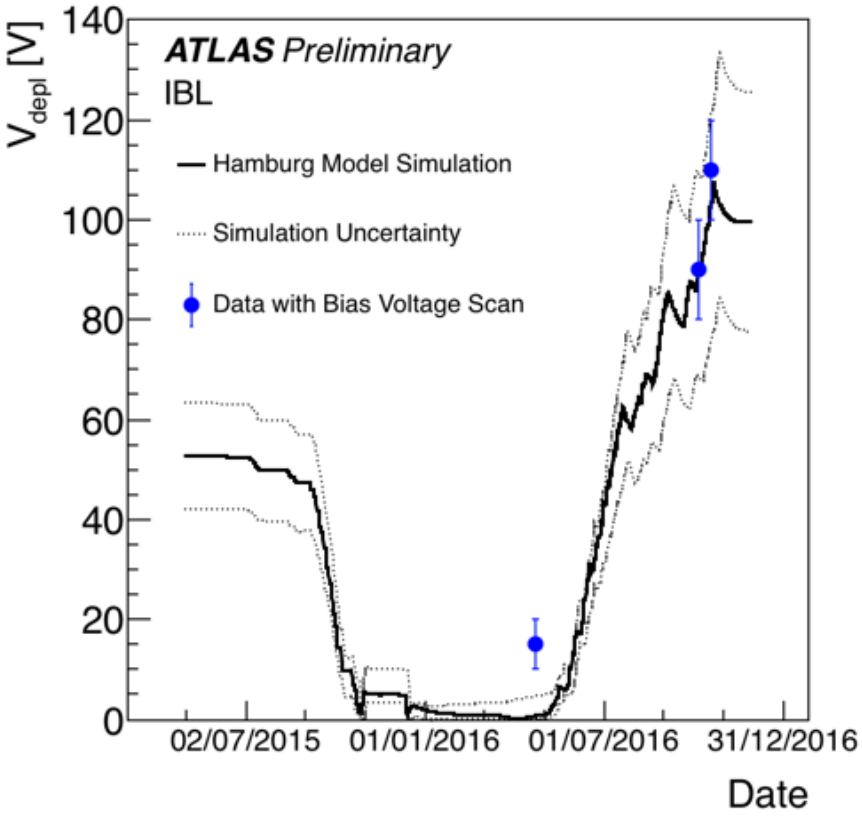

Figure 8: Simulated depletion voltage of the ATLAS IBL according to the Hamburg model, as a function of time from its installation until 2016. The shown simulation uses the central values of the fitted introduction rates; uncertainty band results from varying the parameters within their uncertainty in addition to a 10% uncertainty in the initial doping concentration. The blue points are measurements of the depletion voltage using the bias voltage scan method [25].

2.4 Radiation damage to living tissue

This section is will describe the effect of radiation on living organisms. There are three main parts: the first will explain how radiation interacts within a human cell, and how

this can disrupt its natural processes. The second part will present the Sievert, which is the predominant unit quantifying radiation exposure, and touch on the consequences of high-level exposure. The third part will review CERN's own radiation protection measures. The observance of these measures is a deciding factor in the execution of the ATLAS Inner Detector decommissioning, which leads to the work set out in this thesis.

2.4.1 Effect of radiation on the human body

Radiation can cause damage in cells of living tissue. It can disrupt cell operations either directly via primary or secondary collisions causing single or double breaks in the DNA double helix; or by creating chemically toxic free radicals inside the cell (such as hydrogen peroxide H_2O_2) which themselves disrupt the DNA strands shown in Fig. 9 [26]. Radiation is not limited to damaging only the DNA of a cell, however other types of cell damage are less likely to induce long term health effects. The body resolves the issue regardless of the cause, and so these other types of radiation-induces cell damage is not a focus of radiation protection.

There are two categories of radiation exposure of concern:

- High level exposure leading to large-scale immediate cell death, radiation burns, Acute Radiation Syndrome, and death. Exposure time is acute (hours) or protracted (days) [28].
- Chronic low level exposure where the effects of radiation damage to an individual's DNA culminate over a long period of time (years, lifetime), leading to diseases such as cancer.

In acute high level exposure cases, the radiation levels are the Grays order-of-magnitude for a full-body dose[iii]. Acute Radiation Syndrome or ARS is the term for the illness following high level full-body radiation exposure greater than 1 Gy [28]. For a patient with ARS, it is too late for protective measures and mitigating the long term effects of their radiation exposure is not a priority. ARS can involve any or all of the gastrointestinal, haematopoietic, and neurovascular anatomical systems. Symptoms of ARS include headaches, vomiting, diarrhoea, and fever [26], as well as beta-radiation burns [29]. Radiation burns present an elevated risk of infection, and radiation damage to bone marrow suppresses body's white cell count [30]. Severe radiation burns were a significant factor in the morbidity and mortality of ARS patients following the Chernobyl disaster [29]. 134 people were treated for ARS, having incurred doses between $0.8 - 16$ Gy. There were 28 'short-term' deaths within 112 days of the accident [29]. A similar radiation dose to those involved in the accident is incurred by the CMOS camera in the benchmarking test in Chap 7.

By contrast, radiation protection focuses on the other radiation exposure scenario: low level exposure over a long period of time. It aims to mitigate the long term effects of radiation

[iii] Potential lethal doses are measured in Grays over Sieverts

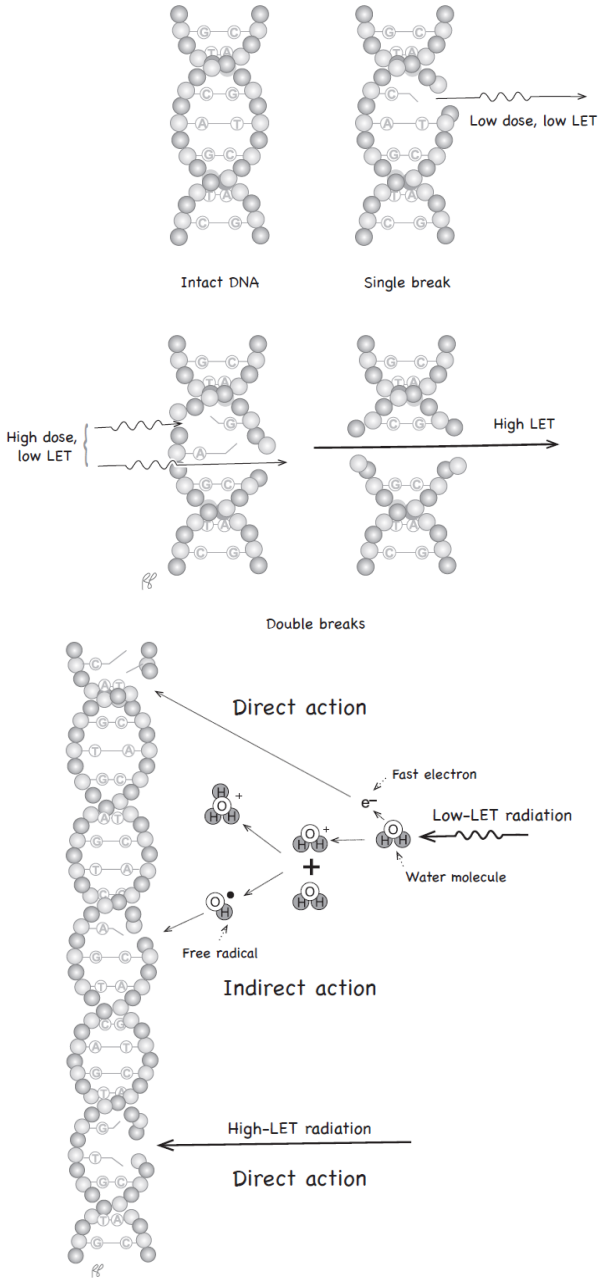

Figure 9: Radiation damage to DNA strands (taken from Essentials of Nuclear Medicine Physics and Instrumentation [26]). Linear energy transfer (LET) defined as the energy of an incident charged particle deposits into a single target. For large targets, this is closely related to the stopping power. However, in the case of smaller targets such as living cells, it is possible that secondary particles created in the primary interaction will carry some of the energy away from the target, meaning the interaction energy is not fully absorbed [27]. LET is most often expressed in keV/μm.

exposure - such the development of cancer from corrupted DNA. The risk of developing cancer from radiation exposure is widely accepted as Linear No Threshold (LNT) [26]. This means there is no safe lower limit to radiation exposure, as the probability of developing cancer increases with each incident of radiation exposure and is proportional to the dose incurred. This is a concern to any facility with a low-level radiation environment requiring human intervention, such as the ATLAS ID decommissioning. DNA damage incurred by incident radiation is discussed in more detail below.

Damage to the DNA bases or single strand breaks are relatively easy for the cell to mend, as there is an intact template from the opposite strand to ensure the genetic integrity of the repair. Double strand breaks are less common than single strand breaks, however they are more prone to misrepair and are therefore more likely to cause adverse biological effects, including cell death [31]. The possible outcomes of radiation damage to a cell are shown in Fig. 10. In most cases, the cell repair is completely successful and the cell will continue to operate normally. However, successful reparation of an irradiated cell depends on the location and extent of the damage. Each act of repair (including of non-radiation related injuries) has a chance of accidental mutation. In some cases, the cell dies from the radiation, either immediately (within hours) or by inhibiting mitosis, the ability of a cell to divide and reproduce [32]. These cases do not lead to long-term consequences unless the number of cell deaths becomes significant to either the organ or the wider human body. More concerning effects occur when a failed cell repair causes cells to reproduce uncontrollably, leading to diseases such as cancer.

Cell survival to radiation damage is dependent on many different variables. These include: radiation type, energy, dose rate; fractionation (when the dose is incurred in several discrete fractions over a number of days, for example in cancer treatment); the target's cell cycle stage, oxygen saturation, and mitotic rate. This leads to different tissue types having different radiosensitivities [31].

2.4.2 The implementation of the Sievert as a unit of risk

As previously discussed, cellular survival rates after radiation damage depend on several variables that affect the statistical outcome. The key factors can be reduced to the type of tissue irradiated and the type of radiation involved.

Biological radiation risk also understands that there are two exposure scenarios for biological systems:

- Acute exposure to (non-lethal) high-level radiation
- Chronic exposure to low-level radiation

Both these scenarios must be accounted for to quantify radiation risk within one functional

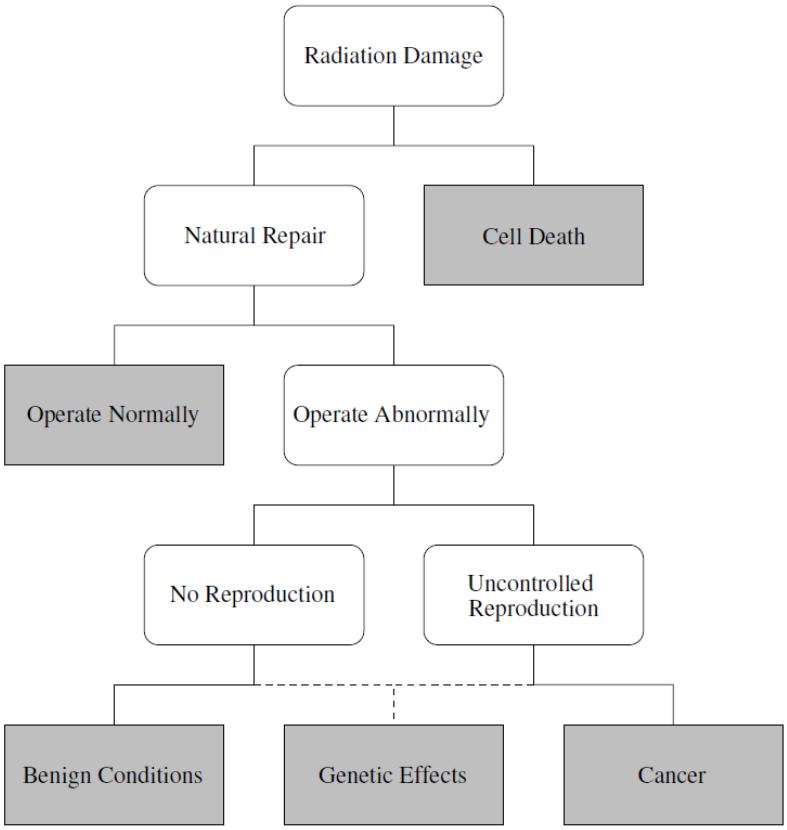

Figure 10: Consequence Tree of cell exposure to radiation (taken from [27])

Examples of Radiation Exposure	
Exposure event	Radiation dose
Consuming 100g Brazil nuts	10 μSv [33]
Panoramic dental X-ray	19 μSv [34]
Flight London to Sydney	0.2 mSv [33]
Mammogram	0.5 mSv [34]
Average annual exposure in the UK (background radiation, not including medical or occupational exposure)	2.3 mSv [33]
1 year cabin crew occupational exposure	2.4 mSv [33]
Chest CT	6.6 mSv [34]

Table 1: A list of commonplace radiation exposure scenarios and the dose incurred in ascending order

and versatile variable. Dosimetry is the measurement of ionising radiation absorbed by an object, commonly the human body [26]. Sieverts (Sv) measure the equivalent dose. Equivalent dose is a calculated value, which is obtained by multiplying the absorbed dose (Gy) by a weighting factor. The weighting factor is dependent on the type of radiation absorbed. For different types of radiation, the radiation in Sieverts is calculated individually per type, then summed. Sievert is also used to express the effective dose, which is the equivalent dose multiplied by another weighting factor to take in account the tissue type of the absorbing material (ie lungs, skin, bladder etc). Effective dose is mostly used in medical settings, where radiation is targeted to specific areas of the body. The Sievert was created to measure risk of long term biological damage due to radiation exposure, e.g. developing cancer, and take into account radiation type and tissue radiosensitivity. Localised radiation exposure is more common than full body exposure, however the scope of this work is interested in full body exposure to background radiation in highly irradiated areas, therefore whole body irradiation is more pertinent. Radiation levels are often quoted in Sv/hour, as a radiation measurement in Sieverts is a better indicator for how dangerous the radiation levels are, and hours are a useful unit to determine time limits on workers.

Radiation metrology instruments do not measure Sieverts directly. Instead they measure Grays, and rely on calibration to display the measurement in Sieverts. These must be re-calibrated when the Sievert weighting factors are updated. In this respect, the Sievert is a mathematical construct. It is important to note that weighting factors alone do not determine danger; gamma rays are more penetrative and cause more damage than brief exposure to alpha particles, which can't penetrate through the dead skin cells in the outer epidermis[iv]. It is generally accepted that risk of developing cancer is linear no-threshold (LNT) with lifetime dose exposure. There is an estimated 1% increase in cancer risk per 100 mSv exposure [26].

[iv] This is not the case if the alpha particles are ingested

2007 ICRP Weighting factors	
Type of Radiation	**Weighting factor**
Photons, all energies	1
Electrons muons, all energies	1
Protons and charged pions	2
Alpha particles, fissile fragments, heavy ions	20
Neutrons:	$w_R = \begin{cases} E_n < 1MeV & 2.5 + 18.2e^{-ln[E_n]^2/6} \\ 1MeV \leq E_n \geq 50MeV & 5.0 + 17.0e^{-ln[E_n]^2/6} \\ 50MeV < E_n & 2.5 + 3.25e^{-ln[E_n]^2/6} \end{cases}$

Table 2: 2007 ICRP Gray to Sievert conversion weighting factors [35]

The International Commission on Radiological Protection (ICRP) use computational phantoms, or references of the average human, to calculate the weighting factor. In 2007, the ICRP issued new guidelines [35] for the weighting factor radiation, see table 2.

Potentially lethal acute radiation exposure is not measured in Sieverts, but in Grays. For an acute irradiation of > 1 Gy, radiation sickness is a much more immediate medical concern than increased cancer risk. An acute irradiation of < 1 Gy is unlikely to be lethal unless the person was already seriously ill, however a full body irradiation dose of 3.5 Gy has a 50% likelihood of survival 60 days post irradiation without medical intervention [36]. While there have been cases of survival at higher doses, > 8 Gy acute exposure is lethal in most cases, and the International Atomic Energy Agency (IAEA) recommends symptomatic treatments only [26].

2.4.3 CERN radiation protection protocols

Radiation protection (RP) covers any health and safety related regulations and procedures concerning exposure to radiation. RP always aims to optimise radiation exposure to be as low as possible as well as mitigate any chances of accidental exposure. Radiation exposure limits are defined as a person's planned exposure to multiple regulated sources. It does not apply in emergency situations or for medical patients. Radiation constraints are defined as all exposure occurrences, of either radiation workers or the general public, to a specified radiation source.

Radiation safety and protection at CERN is a large concern. In Switzerland and France, radiation exposure to workers is limited to 20 mSv/year [37]. CERN categorises workers into two groups, depending on their annual expected exposure rate. Those liable to receive a dose higher than 6 mSv/year in their occupation (Category A), and those not (Category B). However, CERN aims to keep all worker doses below 3 mSv/year and by default all workers at CERN are category B unless specified otherwise [38], [39].

CERN's radiation protection protocols follow the ubiquitous As Low As Reasonably Achievable principle (ALARA), to optimise dose rates. The ALARA concept is the

fundamental principle of radiation protection, and has been the international standard for optimising radiation protection since it was first introduced in 1977 [40]. CERN monitors the individual doses and the collective dose of its workers. The collective dose is the total sum of all their individual doses for a specified work intervention. It is expressed in the units *Man Sv*. Distortions or manipulation of radiation exposure data due to the presence of a single extraordinary high-exposure individual or by bloating the number of workers in the group to include low-exposure staff such as administrative personnel, are prevented by monitoring both the collective dose of an intervention as well as the individual doses of the personnel involved[41].

CERN has five radiation area classifications: Supervised, Simple, Limited Stay, Very High and Prohibited, shown in table 3. Admission to these areas requires a dosimeter. In the first area classification, this dosimeter can be passive or active. The other areas require a personal active dosimeter, which is clocked in and out when entering a radiation area. There is no admission into the Prohibited areas [42].

Area classification	**Dose Limit (year^{-1})**	**Ambient dose equivalent rate**	
		Work Place	**Low Occupancy**
Non-designated	1 mSv	0.5 μSv/h	2.5 μSv/h
Supervised	6 mSv	3 μSv/h	15 μSv/h
Simple	20 mSv	10 μSv/h	50 μSv/h
Limited Stay	20 mSv	-	2 mSv/h
Very High	20 mSv	-	100 mSv/h
Prohibited	20 mSv	-	$>$ 100 mSv/h

Table 3: Cern Radiation Area classifications from [42]

The areas classified at CERN in table 3 at CERN can be considered either **work place** or **low occupancy**. Low occupancy areas are defined as any non-permanently occupied location, such as corridors, stairwells, parking, toilets, etc. It is understood that an individual spends less than 20% of their working time in these low occupancy areas. Working hours are set at 2000 hours per year [43].

Interventions in radiation areas are classified into three tiers, with different requirements for individual total dose H_i, and collective dose H_c. Collective dose is measured in Man-Sievert (Man Sv), it is the sum of all individual total doses. It is used as an optimisation and comparison tool for occupational exposure, as minimising the collective dose necessitates optimising the number of personnel, and their individual radiation exposure while carrying out the work.

- Tier I: $H_c < 500$ Man μSv; $H_i < 100$ μSv;
- Tier II: $H_c < 5$ Man mSv; $H_i < 1$ mSv;

- Tier III: $H_c > 5$ Man mSv; $H_i > 1$ mSv;

Tier III requires approval from Radiation Protection, and must be signed off by the ALARA committee before work can begin [43].

As seen previously in chapter 2, neutron interactions with atomic nuclei can induce radioactivity in the target material. This means the detector is a radiation source, and creates a significantly higher level of background radiation around it than occurs naturally. This radiation presents a significant obstacle for personnel wanting to physically interact with the detector. The reasons for caution will be explored further in the next section (chap. 2.4), and methods for estimating the radiation levels in the ATLAS cavern are presented in chap. 3.3.3.

3 The ATLAS Experiment at the LHC

The Standard Model [44] is one of the most successful models in particle physics, describing how twelve fundamental particles (six quarks, six leptons, divided into three generations) and their corresponding anti-particles interact with the electromagnetic, strong and weak forces, conveyed by bosons. The Standard Model predicted the existence of W, Z, Gluon, and Higgs bosons, as well as the top and charm quarks. While it gives a lot of detail about the fundamental particles and their properties, there are some parameters that require experimental data to be quantified as well as other phenomena that needs to be explained.

The aim of the LHC, and its associated experiments such as the ATLAS detector experiment, is to provide experimental data on particle properties as well as search for new Beyond the Standard Model physics.

This chapter will give an overview of the LHC machine and its planned upgrade schedule, and the ATLAS detector, its constituent sub-detectors and the cavern in which it sits. The work in this thesis concerns the partial decommissioning of the ATLAS detector as part of the LHC upgrade. The setup of the detector and the background radiation in the ATLAS cavern are the main factors for the proposed work.

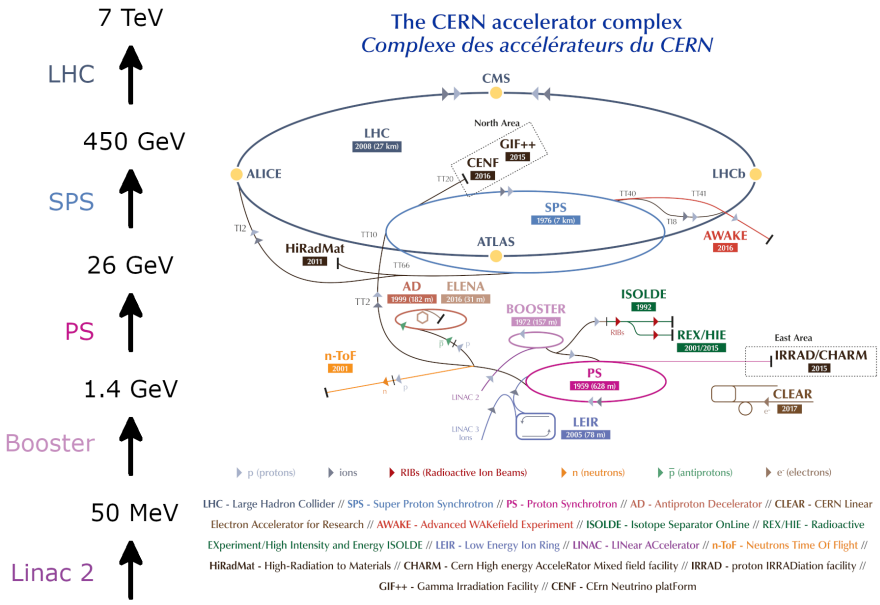

Figure 11: Map of the CERN accelerator complex with increase in proton energy as it travels through LINAC2, Booster, Proton Sychrotron, Super Proton Synchrotron, and LHC ring. Adapted from [45]

3.1 The Large Hadron Collider

The LHC is the most recent particle accelerator built at CERN. It is 27km in circumference, and is the largest of its kind in the world. Two proton beams of 6.5 TeV travel in opposite directions around the machine. Around the synchrotron ring there are the four 'interaction points' where the beams intersect; and surrounding these are the 4 main experiments of the LHC: ATLAS, CMS, LHCb, and ALICE.

The LHC particle beam is not continuous, instead it is a stream of particle bunches, which can be characterised as a Gaussian distribution. An LHC beam is made of 2'808 bunches, spaced 25 ns (7.5 m) apart, with 1.15×10^{11} protons per bunch.

The LHC beam is kept on its circular trajectory using superconductor dipole magnets, the strength of which limits the maximum energy of the particles stored in the ring. The LHC dipole magnets create 8.33 T. A malfunction or poor performance of a single steering magnet would undermine the performance of the whole machine.

The magnetic field is ramped up as the particles accelerate to keep the radius of their orbit constant. Besides the dipole magnets, the LHC also has two types of quadrupole magnets which are used for beam optics. Protons repel each other due to their positive electric charge, which causes the bunches in the beam to distend over time. The quadrupole magnets refocus the bunches, making the beam easier to steer, and increases the probability of collisions at the interaction points.

Head-on particle collisions can be described by the centre mass energy equation:

$$E_{CM}^2 = (E_1 + E_2)^2 \tag{2}$$

The LHC can accelerate protons to 7 TeV meaning the centre-of-mass energy of the collision is 14 TeV.

Collisions at particle accelerators are measured using "luminosity". There are two type of luminosity that can be discussed: instantaneous and integrated luminosity. Instantaneous luminosity is the collision rate per unit area, and is defined as inverse barn per second, where 1 barn = 10^{-28}m^2. Integrated luminosity is the time integral of the instantaneous luminosity, and is measured in inverse barns.

Quantum interactions are governed by probability, so a large number of collisions increases the likelihood of a rare interaction. The event rate of collisions in a particle accelerator is defined as:

$$R_{event} = \sigma \int_{t_0}^{t_1} L(t)\, dt \tag{3}$$

where σ is the cross section, and L(t) the instantaneous luminosity [46]. Cross section is a measure of probability, a property intrinsic to the event; so to increase their event rate, particle accelerators aim to maximise their luminosity. This means luminosity is one of the

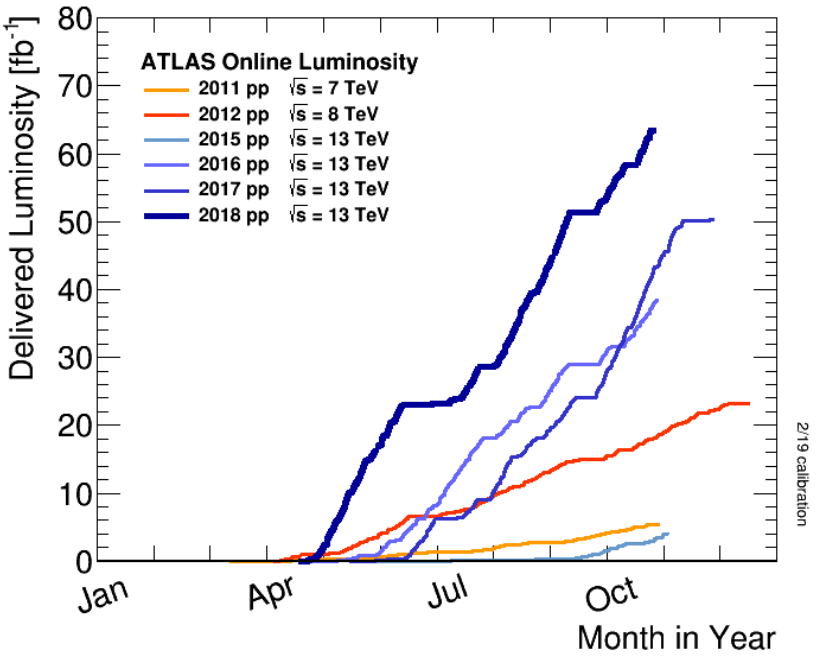

Figure 12: Integrated luminosity at the ATLAS detector versus time 2011-2018, taken from [47]

most important design factor when commissioning particle accelerators. The luminosity of two colliding proton beams is expressed as:

$$L = \frac{N_p^2 f_r N_b}{4\pi s_x s_z} \tag{4}$$

where N_p is number of protons per bunch, N_b is the number of bunches, f_r is the frequency of revolution and s_x and s_z are the dimensions of the gaussian shaped beam. The LHC has a design luminosity of 1×10^{34} cm^{-2}s^{-1} [46], and reached a peak of 2.1×10^{34} cm^{-2}s^{-1} in Run 2.

Fig. 12 shows the evolution of integrated luminosity over the course of a year. There is a clear difference in slope between the initial runs at lower energy and the later ones. However, the energy of the beams and the luminosity are not related. Over time physicists learn how to manipulate the beams to get the smallest interaction point which equation 4 shows will increase the luminosity from the machine [48].

The LHC is expected to have three periods of data over its lifetime, interspersed with Long Shutdowns (LS) for general detector maintenance and staggered upgrades.

1. Run 1 ran from 2010-2012 with a beam energy of 7 TeV, and instantaneous luminosity peaked at L = 7.5×10^{33} cm^{-2}s^{-1}. At the end of Run 1, the integrated luminosity was $\int Ldt = 30$ fb^{-1} [49].

2. Run 2 ran from 2015-2018 with a beam energy of 13 TeV, the instantaneous luminosity peaked at $L = 2 \times 10^{34}$ cm^{-2}s^{-1} [47]. At the end of Run 2, the integrated luminosity was 140 fb^{-1} [46].

3. Run 3 is planned to run from 2021-2023 with a beam energy of 14 TeV, the instantaneous luminosity peaked at $L = 2 \times 10^{34}$ cm^{-2}s^{-1} [46]. At the end of Run 3, the integrated luminosity is expected to be 300 fb^{-1} [49].

During Long Shutdown 3 (LS3) after Run 3, the collider will upgrade to the High Luminosity LHC (HL-LHC). The HL-LHC aims to operate at an instantaneous luminosity of up to $L = 7.5 \times 10^{34}$ cm^{-2}s^{-1}. The target integrated luminosity is 3000 fb^{-1} over the HL-LHC's 10 year lifetime [46]. This is ten times the expected integrated luminosity after Run 3.

The significant increase in luminosity requires major upgrades to the LHC and its detectors to accommodate the higher particle fluence. The work presented in this thesis was done for the upcoming ATLAS Inner Detector decommissioning during the LS3 shutdown, part of the ATLAS upgrade in preparation for the HL-LHC.

3.2 The ATLAS Detector

The ATLAS detector [13] shown in Fig. 13, was completed in 2008. The detector is 46 m long, and 25 m in diameter. It is cylindrically symmetrical around the collision point and covers a solid angle of almost 4π. It is a large multipurpose detector which is formed of multiple sub-detectors, each devoted to particle identification and tracking.

These are:

- The Inner Detector (ID) [50], itself composed of three sub-detectors: the Pixel Tracker [51], SemiConductor Tracker (SCT), and Transition Radiation Tracker (TRT) [52]
- Four calorimeters: Liquid Argon (EM, Hadronic endcap and Forward) [53] and Tile [54]
- Muon spectrometer [13]
- Three forward detectors - two which measure luminosity, and one which characterises heavy-ion events [13].

Each of the sub-detectors has a specific role and works complementary to the others. Particles travelling through the detector leave behind a unique signature, which can only be identified by combining the data from the different sub-detectors.

The detector and sub-detectors can be divided into three regions: the central barrel and two endcaps either side. The barrel is cylindrical and sits around the collision point. The endcaps are disk shaped and are 'forwards' from the collision point (from the proton's frame

of reference). Only one of the partons inside a proton interacts in a collision and is scattered at large angles. The remnants decay into a hadron shower in the forwards direction. The ID is the closest to the collision point, so the ID endcap takes the brunt of the hadron showers. The ID endcap is the most irradiated section of the ATLAS detector (and therefore it is the most radioactive, see chapter 2.1.2).

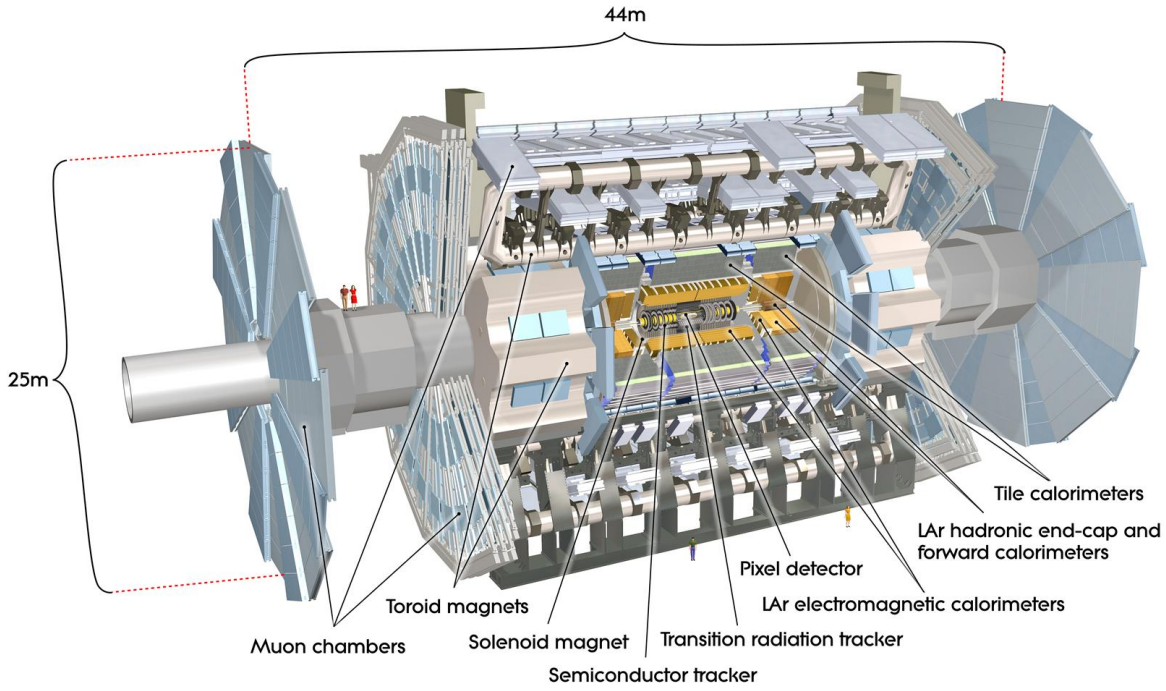

Figure 13: Cut-away of the ATLAS detector [55]

The following section will discuss the different ATLAS sub-detectors. It will start with the sub-detector closest to the collision point, the Pixel tracker in the Inner Detector, and move outwards layer by layer.

3.2.1 The Inner Detector

The Inner Detector tracks charged particles and measures their momentum. The Inner Detector is composed of three sub-detectors which can be seen in Fig. 14: the Pixel tracker and the Semiconductor Tracker (SCT), which are both silicon based detectors, and the Transition Radiation Tracker (TRT) which uses straw drift tubes. The ID is built around the interaction point with a cylindrical central barrel region, and two disk-shaped endcap sections on either end.

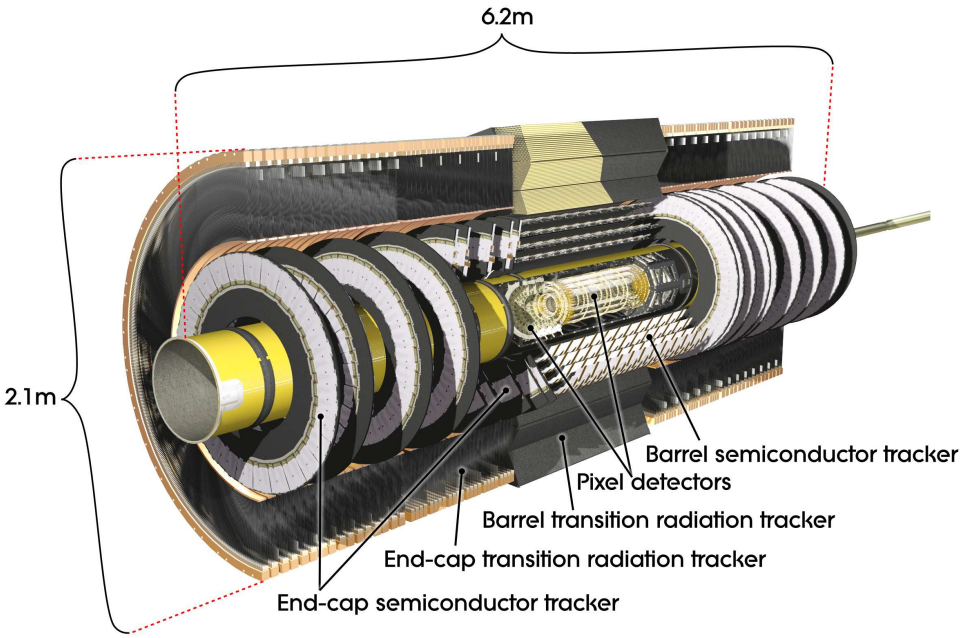

Figure 14: Cut-away of the Inner Detector, from [56]

Sub-detector	**Section**	**Inner Radius [mm]**	**Outer Radius [mm]**	**Length [mm]**	**Number of Layers**
Beampipe		25	29		
Pixel and IBL	Envelope	31.0	241.0	$0 < \|z\| < 3092$	
	Barrel	33.25	122.5	$0 < \|z\| < 400.5$	4
	Endcap	88.8	149.6	$495 < \|z\| < 650$	3
SCT	Envelope barrel	255	549	$0 < \|z\| < 805$	
	Envelope endcap	251	610	$810 < \|z\| < 2797$	
	Barrel	299	514	$0 < \|z\| < 749$	4
	Endcap	275	560	$839 < \|z\| < 2735$	9
TRT	Envelope barrel	554	1082	$0 < \|z\| < 780$	
	Envelope endcap	617	1106	$827 < \|z\| < 2744$	
	Barrel	563	1066	$0 < \|z\| < 712$	73 straw planes
	Endcap	644	1004	$848 < \|z\| < 2710$	160 straw planes
Total ID Envelope		0	1150	$0 < \|z\| < 3512$	

Table 4: Geometry parameters of the Inner Detector. Table taken from [13], however the parameters of Pixel which include the IBL where taken from [57].

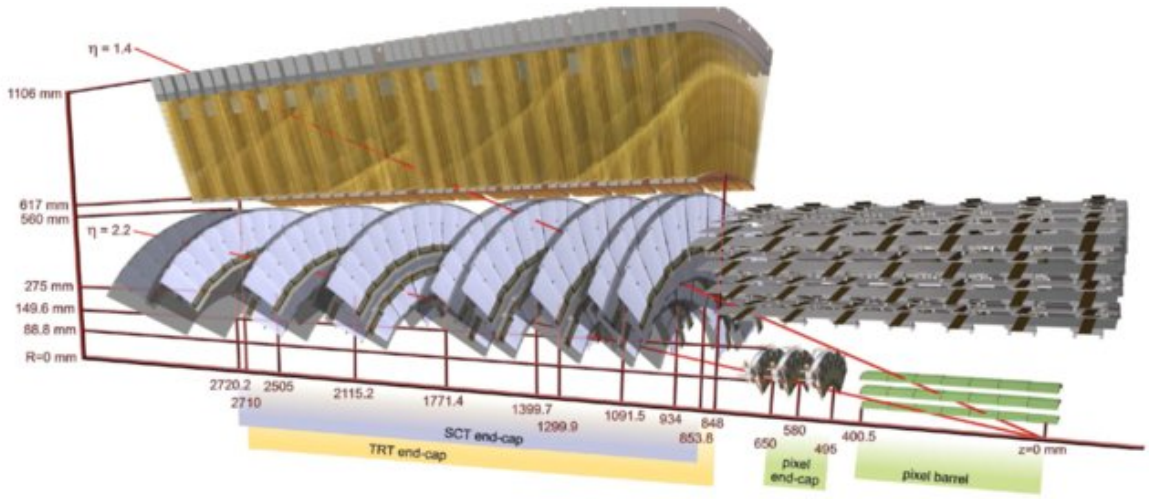

Figure 15: Cut-away of the Inner Detector barrel and endcap regions[58]

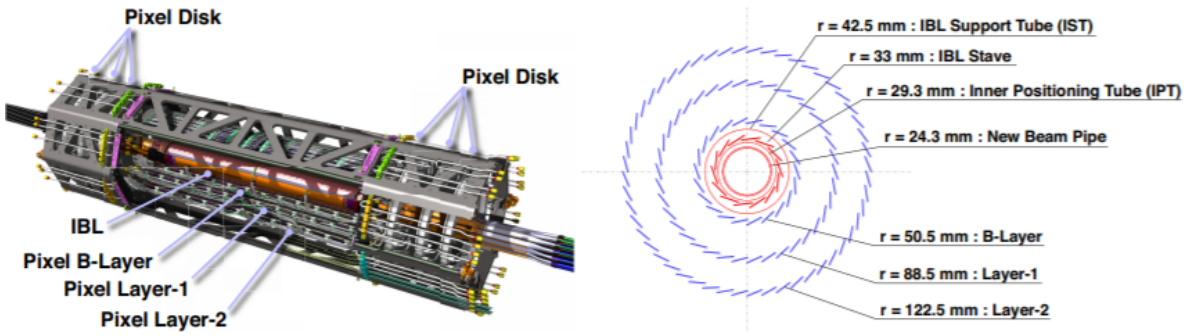

Figure 16: Cut-away of the Pixel Tracker and IBL, showing the Pixel's octagonal support structure and transverse diagram of the barrel layers, from [59]

3.2.1.1 Pixel Tracker

The Pixel is the innermost ID sub-detector, and the closest to the interaction point. It uses silicon pixel sensors to provide the finest granularity of the charged particle trajectories. It is 1.44 m long and 0.43 m in diameter, and is formed of four barrel layers: the Insertable B-Layer (IBL) inserted in 2014, Layer 0, Layer 1, Layer 2; and two identical endcap regions with 3 layers each on either side of the barrel. The barrel layers are cylindrical with sensors mounted parallel to the beam axis. The endcap layers are disk shaped, and have sensors mounted perpendicular to the beam axis.

The IBL uses two types of modules to cope with the higher radiation fluence being closest to the interaction: planar double chip modules, and 3D single chip modules [57], [60]. Twelve planar double chip modules are mounted centrally on each stave, with four 3D single chip modules on each extremity [59]. The Pixel detector is mechanically supported by staves (in the barrel region) and disk sectors (in the endcap) on which the detector modules are mounted [51]. These outer support structures can be seen in Fig. 16. The inner support structures are made of rigid low-activation materials like carbon foam [57] and carbon fibre [51]. The vacuum beampipe inside the Inner Detector is made of beryllium [13]. The support structures provide the framework for the detector's architecture. Electrical, optical, and cooling services are routed through Patch Panel 1 at the end of the Pixel Support Tube (the outermost support structure for the Pixel tracker) [51].

3.2.1.2 Semiconductor Tracker

The SCT is the second-innermost sub-detector. It measures the momentum and vertex position needed for event reconstruction. Both the SCT and Pixel tracker detect particles using the principle of a depleted PN junction, though the semiconductor tracker uses silicon microstrip sensors instead of pixels [61].

The SCT is 1.5 m long and 1.1 m in diameter, and is comprised of four concentric barrels and two endcap regions of nine disks each. The SCT has more room for a structured support, so its sensors are not mounted on staves and disk sectors, instead the barrel modules are mounted onto a cylinder, shown in Fig. 17. The SCT Barrel layers have a total of 2112 modules. Each module is composed of 4 single sided strip modules (64 $\times$ 63.5 mm each), glued back-to-back to create a double-sided 64 $\times$ 128 mm unit [50]. The endcap modules are arc-shaped, and require five different sized sensors due to the complex geometry [62].

3.2.1.3 Transition Radiation Tracker

The TRT is the outermost of the Inner Detector subsystems. It is a straw tracker detector, composed of 4mm straw-like tubes filled with a Xenon-based gas mixture.

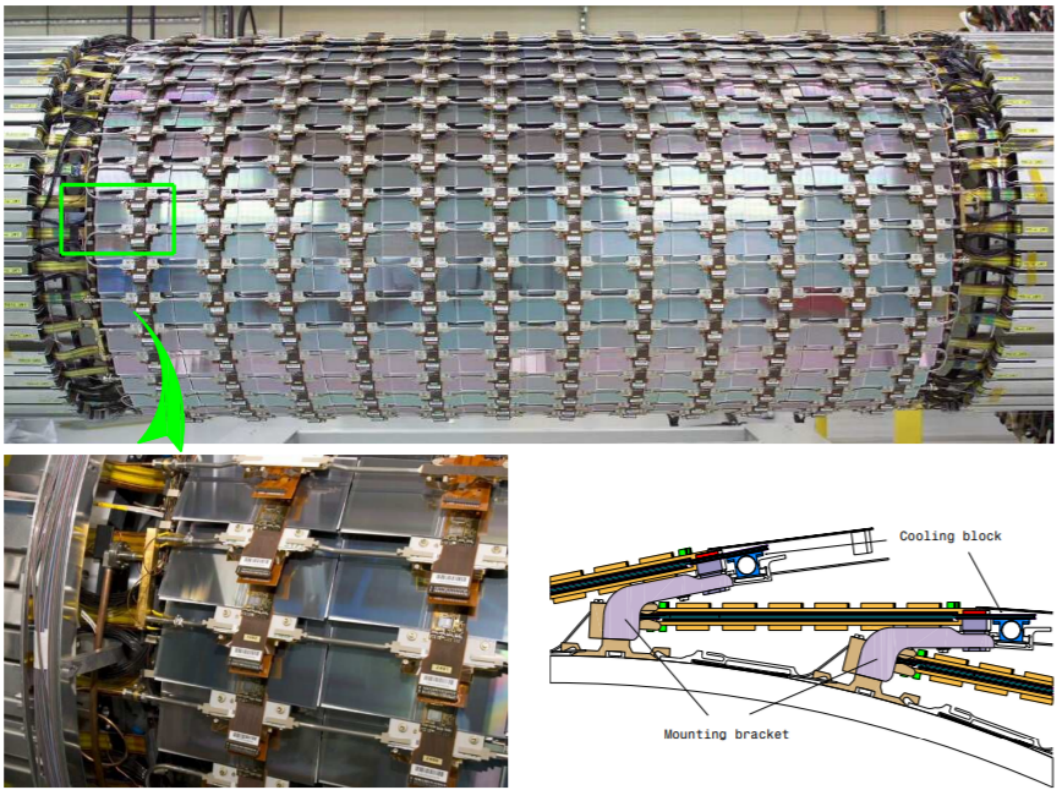

Figure 17: The SCT barrel, with close up of the mounted barrel modules, and diagram of the mounting brackets. From [13]

Charged particles travelling through the gas create ion pairs. The E-field across the region exerts a force on the ions, preventing recombination and causing them to drift to the electrodes at the edge of the region. This creates a detectable current, and is interpreted as a signal by the detector.

The TRT provides two types of information. Like the Pixel and SCT, it makes position measurements, providing additional information for particle tracking [63]. The construction of the TRT barrel is supported mechanically by the Barrel Support System (BSS) space-frame which also acts as mechanical support for the SCT [13]. The barrel of the TRT covers $|\eta| < 1.0$, and its straws are laid parallel to the beam axis.

The TRT endcap is made of wheels where the straw tubes are configured radially like spokes of a bicycle. The endcaps were constructed in planes, each with four layers of straws. These assemblies were then paired together to create an eight-plane independent unit [64]. The straw tubes do not have the rate capability to cope with the anticipated HL-LHC luminosity, the TRT would reach 100% occupancy, affecting the detectors efficiency [65].

The Inner detector was designed to run for 10 years at $L = 1 \times 10^{34}\text{cm}^{-2}\text{s}^{-1}$. It first exceeded these design parameters in 2016. The ID has suffered significant radiation damage from the LHC collisions. The Pixel was designed to withstand an integrated luminosity of 400 fb^{-1}, and the SCT to withstand 700 fb^{-1}. The ID integrated luminosity limit of the ID is expected to be reached in 2023, after which the operation of the machine cannot be guaranteed [65]. There are significant concerns about thermal runaway within the ID, as well as the hit efficiency decreasing to inoperable levels. Other concerns prompting its removal and the upgrade to the ITk are the bandwidth saturation, occupancy, and the performance of the trigger system.

To ensure the ATLAS detector remains effective for the HL-LHC, the entire Inner Detector (Pixel, SCT and TRT) will be replaced with an entirely silicon-based detector, the ITk. The new detector is designed to last 10 years, at $L = 7.5 \times 10^{34}\text{cm}^{-2}\text{s}^{-1}$.

3.2.2 The Outer Components

This section with give a brief overview of the outer components of the ATLAS detector: the electromagnetic and hadronic calorimeters, the toroid magnet, and the muon spectrometer. These components will be kept for the HL-LHC, however the front-end electronics need to be upgraded to cope with the new radiation, trigger, and read-out performance criteria [66].

Around the Inner Detector is the Solenoid Magnet, which creates a magnetic field of 2.0 T across the ID. This bends charged particles, helping with particle identification and momentum measurements. It shares a vacuum vessel with the Liquid Argon (LAr) electromagnetic (EM) calorimeter, and the two were combined before being installed in the ATLAS cavern.

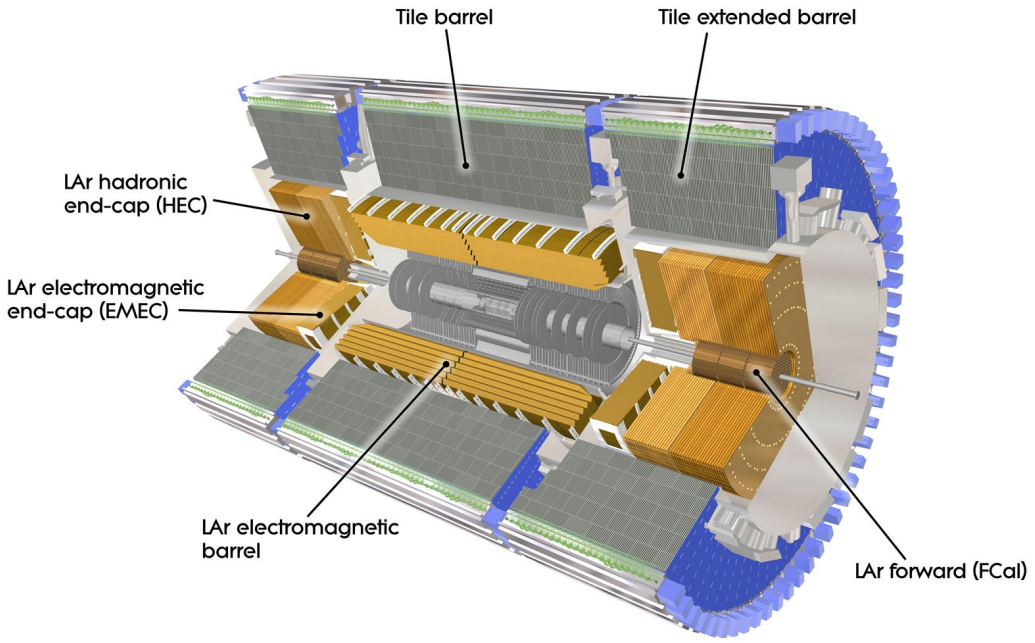

Figure 18: Cut-away of the Liquid Argon and Tile Calorimeters, from [67]

Calorimeters measure the energy of incoming particles. By definition this is a destructive measurement; the particles measured in the calorimeter are absorbed and do not penetrate further into outer layers of the detector [68]. The LAr EM calorimeter is the innermost calorimeter (Fig 18). It detects and measures the energy of electrons and photons, primarily through creating particle showers using Bremsstrahlung or pair production (see also chapter 2). Electrons and photons are much more likely to create particle showers than hadrons, therefore they will be absorbed into the first calorimeter with which they interact.

Hadronic calorimeters absorb the particles left after the EM calorimeter, except muons and neutrinos. Hadronic showers do have an EM component, however the electrons and photons originating from the initial pp event were absorbed in the EM calorimeter, any found in the Hadronic calorimeter must have been produced by a hadron shower.

The Tile Calorimeter is a scintillation calorimeter. Unlike the LAr calorimeters which detect electric charge as the signal, scintillation calorimeters collect the signal in the form of light [54].

The LAr forward calorimeters have three layers. The first of the forward calorimeters (FCal1) is an LAr-Copper EM calorimeter, the same material components as the LAr hadronic endcap. The second and third forward calorimeters (FCal2, FCal3) are LAr-Tungsten. A copper alloy plug was mounted behind the third forward calorimeter to reduce background noise to the muon spectrometer [69]. The forward calorimeters have been activated, and

contribute to the background radiation in the cavern. However, due to timing and logistical concerns, the FCal is not being replaced as part of the HL-LHC upgrades. Instead, a smaller calorimeter (the Mini-FCal) will be inserted in front of the FCal to compensate for the projected problems running to FCal at HL-LHC luminosities [70].

Around all of this sits the Toroid Magnet. An image of the eight barrel toroidal magnets is arguably the ATLAS detector's most iconic photo (Fig. 19). The Toroid magnet creates a 4T magnetic field [13]. The remaining charged particles (muons) traversing the field are subject to the Lorentz force, causing their trajectory to bend. The rate of curvature of the trajectory facilitates their momentum measurement in the muon spectrometer.

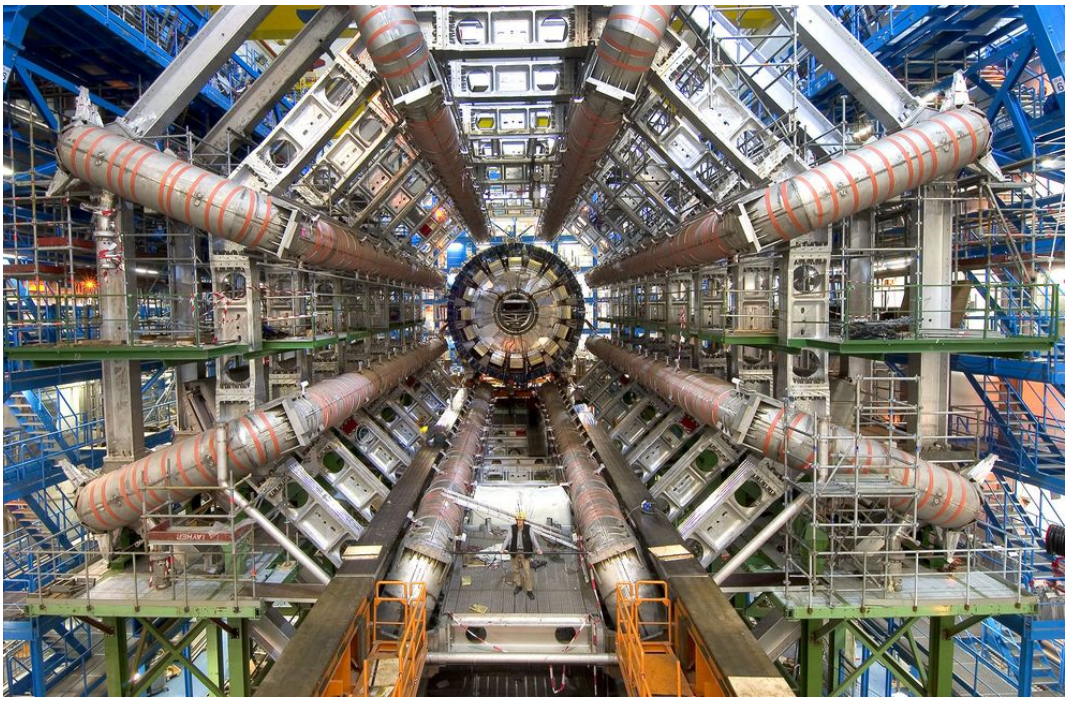

Figure 19: Photo of the eight barrel Toroid magnets (front) awaiting the installation of the barrel calorimeter (behind). The calorimeter will be pushed forward using stainless steel rails (bottom). A man stands to scale. From [71]

Muons are detected through each level of the detector, however all other interacting particles have been absorbed in the calorimeters, so muon chambers are used to differentiate muons from other particle signals and to measure their momentum to a higher precision.

3.3 The ATLAS detector installation, maintenance and ID decommissioning

This section gives an overview of the ATLAS cavern, how the detector was installed, the logistics of technical works of maintenance, as well as the planned ID decommissioning.

3.3.1 The ATLAS cavern

The ATLAS detector sits in experimental cavern UX15 100m below the surface. The cavern is 53 m long, 30 wide and 35 m tall [72]. It is surrounded by access shafts, service ducts and other smaller areas used for ATLAS services. USA15 which houses the ATLAS electronics, is far enough from the main cavern to allow personnel constant access even during high luminosity beam-on. The access shafts are blocked by large concrete plugs during run time, to shield surface building SX1 and the surrounding area from the radiation [73]. The construction of the detector was done in-situ, with pieces being lowered down the access shafts and subsequently installed.

3.3.2 Installing the ATLAS detector

Work officially begun on the installation of the ATLAS detector in 2003 with the inauguration of the ATLAS cavern. The work was completed in October 2008 and the first collisions begun in 2009. The installation of the ATLAS detector can be split into five phases.

1. Cavern infrastructure and mechanical support for the detector
2. Barrel Toroid and Barrel Calorimetry
3. Endcap Calorimetry and Muon Barrel Chambers
4. Muon Big wheels, Inner Detector, and Completion of Muon Barrel
5. Endcap Toroid and Muon Small Wheels

The ATLAS detector takes up most of the available space in the cavern. As its installation progressed, the available space became more and more restricted and some installed pieces were subsequently moved aside to make room for incoming components.

Phase 1: Before work on the detector itself could begin, the necessary infrastructure and support structures in the main cavern needed to be installed. These included overhead cranes, ventilation, lighting and electricity; as well as bed plates and support feet to provide the mechanical support on which the detector was constructed.

Phase 2: Several different sub-detectors were in assembled and installed in parallel, taking advantage of the space of the empty cavern.

The barrel Toroid coils were lowered into the cavern using the PX14 shaft on side A (shown in Fig. 20), beginning October 2004. The Toroid magnet was the first sub component to be installed and took up the centre of the cavern. Muon chambers were also installed in parallel, specifically those that were situated in between the ATLAS feet and struts.

The lower half of Tile barrel Calorimeter was assembled in the cavern on a temporary structure on side C, beside the Toroid coils. Once finished the LAr calorimeter cryostat

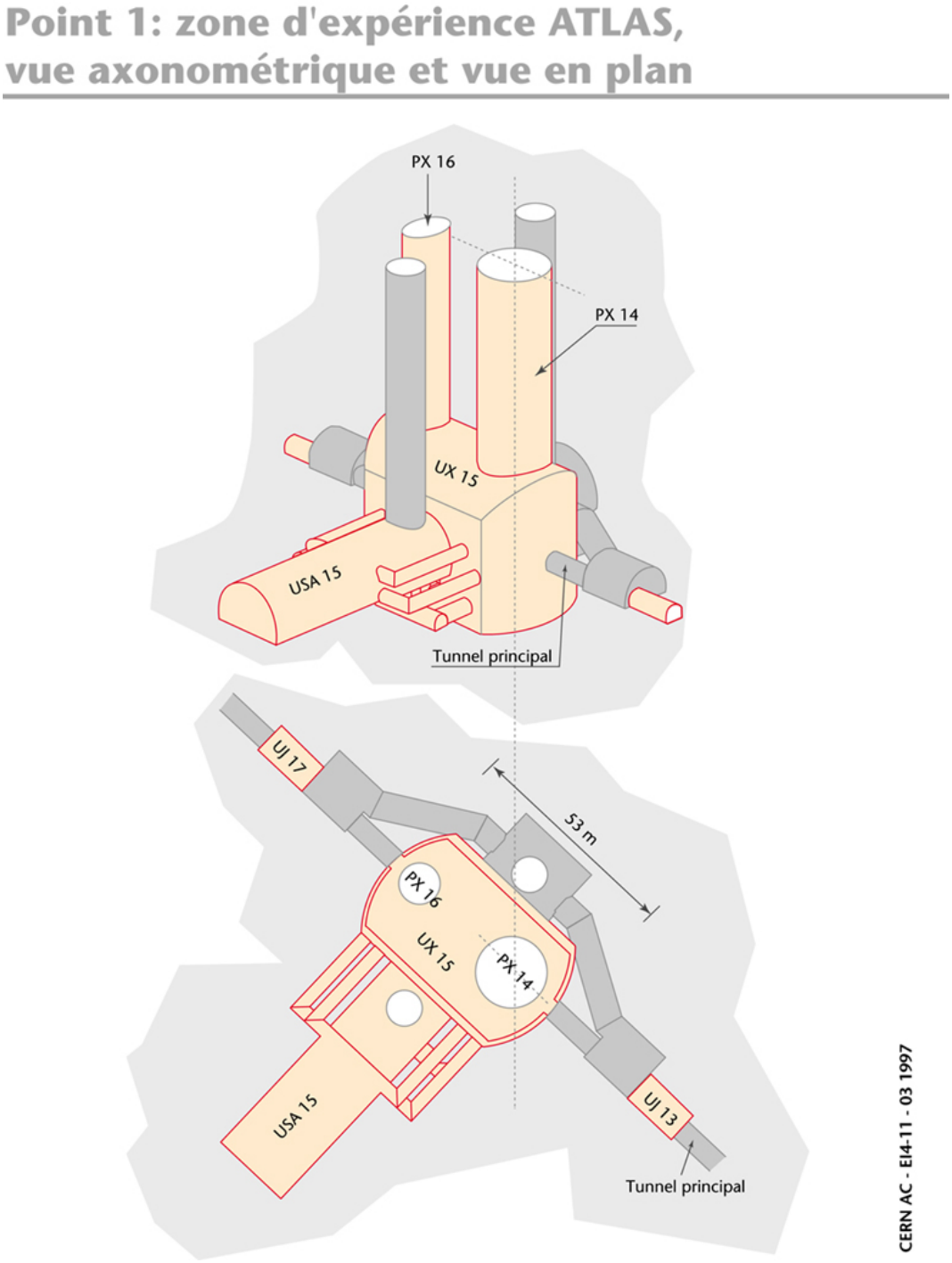

Figure 20: The ATLAS cavern UX15 and the surrounding access shafts and service tunnels. USA15 houses ATLAS electronics away from the high radiation levels of the main detector. From [74]

chamber was placed onto this half-cradle. The Tile barrel assembly was then continued until the whole barrel Calorimeter was complete and was installed inside the Toroid coils in October 2005.

Phase 3: The Endcap calorimeter began assembly in the space liberated by the barrel Calorimeter on side C, and was installed inside the Toroid barrel in February 2006.

On side A, installation of the muon barrel chambers started, and the second endcap calorimeter was assembled, however its installation was delayed in favour of testing the magnetic field of the Solenoid Magnet.

Phase 4: After this, in August 2006 the Inner Detector barrel (SCT and TRT only) was installed inside the bore of the calorimeter cryostat (side A). Space is now much diminished and the calorimeter endcap had to be moved partially inside the Toroid to allow space for the continued installation for the muon barrel chambers. The muon Big Wheel on side A started in January 2007, before the calorimeter endcap was moved back to allow the Inner Detector endcap to be lowered.

On side C, the Muon Big Wheels began installation April 2006, and finished 11 months later. The Big Wheels were then pushed back for the lowering and installation of the Inner Detector endcap. The final muon barrel chambers were installed, and the Big Wheels moved into position, closing the barrel on side C.

The SCT and TRT barrel were installed together as they share the BSS as their mechanical support. The Pixel's mechanical support structure is the Pixel Support Tube (PST). The barrel of the PST was inserted into the SCT, and its endcap pieces were installed hanging in the empty space. The SCT/TRT endcaps were then installed around it. The Pixel itself was assembled externally as one whole piece. It transferred into the PST from another support tube used for transport, called the Dummy Support Tube (DST). The two SCT/TRT endcaps, the Pixel, and the central beampipe section were installed in May-June 2007.

Phase 5: The Endcap Toroids were lowered into place in July 2007, and connection of their services and cooling was completed shortly afterwards [76], [77]. The Muon Small Wheels were installed spring-summer 2008, in parallel to completion of the Pixel detector services [78].

The detector was fully installed in time for the first LHC test beams in 2008, however certain subsystems were switched off [78].

3.3.3 Estimating radiation levels in the ATLAS Cavern

In-depth knowledge of the radiation is crucial both from a general detector health standpoint, but also for running any maintenance operations.

Simulation studies are used to predict where the radiation fluence will be concentrated. The simulations are then supported with Radiation Monitoring (Radmon) [79] and other

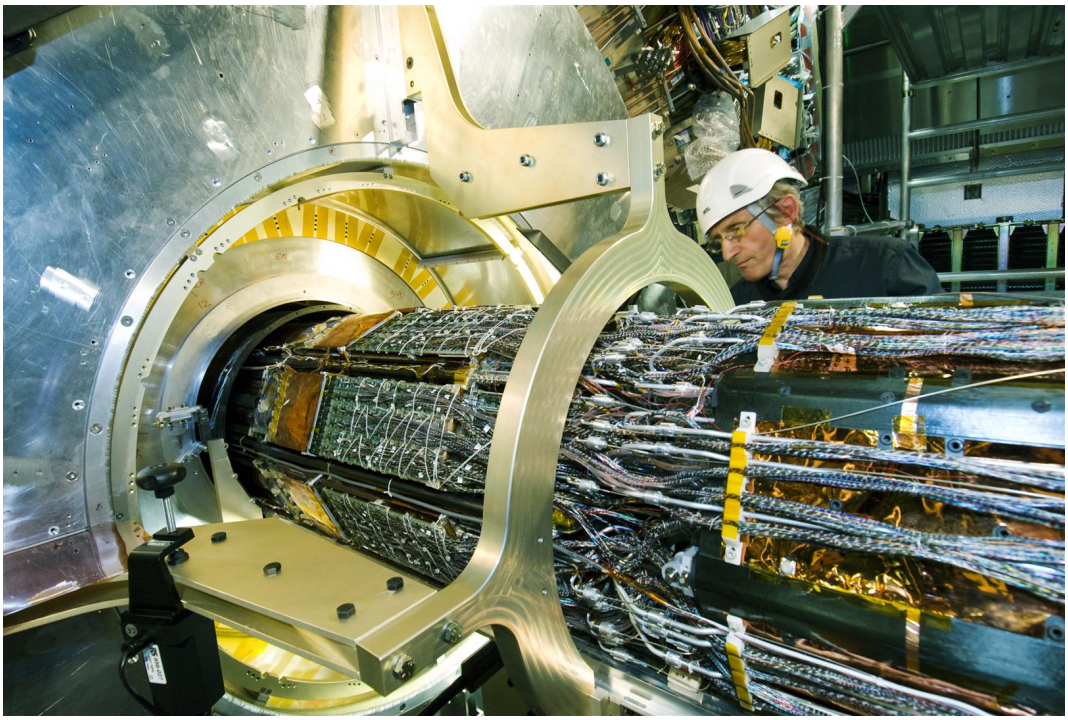

Figure 21: Photo of the Pixel barrel insertion, with Pixel support ring. From [75]

studies [10]. They are also used to verify the design of detectors and their components by giving insight into operating parameters and necessary lifetime radiation tolerance [80].

CERN's radiation protection team uses FLUKA to conduct activation studies of the ATLAS cavern, in preparation of significant intervention works such as the LS3 shutdown. FLUktuierende KAskade or FLUKA is a particle transport code that simulates nuclear and sub-nuclear particle interactions through complex geometries [81]. FLUKA uses the Monte Carlo method to calculate physics processes. Monte Carlo simulations are used extensively when modelling fundamentally stochastic phenomena, such as particle interactions.

FLUKA calculates each individual particle's trajectory and randomly samples its 'fate' from all the possible outcomes from physics processes; the probability of each process selection is determined by its cross section [82], [83]. When rerunning individual calculations, the results will vary slightly due to the stochastic variables inherent to the Monte Carlo approach. A simulation run with a large number of samples will have a more stable result. Therefore to have enough data for a significant result, the simulation effectively repeats each calculation multiple times each with new pseudo-randomised sampling [84], [85]. By contrast, a deterministic simulation will return the same result for each iteration, and reruns will offer no new information.

The simulations of the background radiation in the ATLAS cavern are computationally demanding. The ATLAS experiment experiences $\approx 10^9$ particle collisions per second during

beam on, and has been running since 2010. The simulations also depend heavily on the LHC run parameters - centre-of-mass energy of the collisions,instantaneous luminosity, etc - as well as the anticipated cooldown time before the ID decommissioning starts. Unfortunately, these are also highly susceptible to change, making previous simulation results redundant.

The data from these simulations are issued in the form of radiation maps. These maps cover a quadrant of the detector. The detector is symmetrical along the Z axis and the XY plane, it is assumed that the background radiation will be equally symmetrical. Per ATLAS detector nomenclature, the coordinate system used is cylindrical (R, ϕ, Z), with the origin at the collision point and the Z-axis along the beamline. The radiation dose maps are given in μSv/h and have 10 cm resolution in R and Z, with the dose smeared in ϕ.

Radiation studies continue to give insight into the Atlas detector - the material activation, shielding efficiency, as well as help predict background radiation levels that would affect access to the underground areas. As radiation cools down over long time periods, it is important to know how much background radiation will continue to linger after beam-off and maintenance/decommissioning work.

Until 2013, the detector was anticipated to have a radiation field of 180 μSv/hr 1 m from the beam axis, and 1.1 mSv/h at 10 cm from the beam axis at Long Shutdown 3 [80]. As seen in chap 2.4.3, CERN classifies anything above 3 μSv/h as a controlled area. These radiation levels qualify as a limited stay-controlled area, with the legal requirement of personnel exposure restricted to 20 mSv/year. This would severely curb the duration of human intervention allowed during the decommissioning. In this case robotic systems would be needed be used, and research into their development was carried out [86]. The access scenarios with dose rates marked can be seen in Fig. 24. These dose rates would mean unavoidable high dose exposure to workers during standard access/short opening. Operating using large opening could potentially reduce the radiation exposure, however this would limit the work to one side of the detector. In 2013 the results of more advanced simulations were published. These have revised the radiation estimates downwards, and is now anticipated to be 10 μSv/h 1 m from the beam axis, a factor of 18 lower than the 2003 estimates [87]. This is primarily due to more advanced modelling of the detector and taking into account self-shielding effects, where the outer components of the detector shield workers from a higher activated inner segment. The ID was not designed to be decommissioned using remote handling, and the technology is still in development. The requirements for dexterity, radiation tolerance, and strength would be a steep challenge for robotic solution to fulfil. The decommissioning of the ID also needs to be completed within a certain time frame to allow the installation of the ITk before the scheduled HL-LHC switch on. The revision of the expected dose rates meant that human presence was a viable option for the ID decommissioning. Given the high risk presented by the remote handling option, a human-based intervention was preferred. This work was initially meant to assess the radiation tolerance of robotic manipulators for the

ATLAS decommissioning. Following the new radiation estimates, this was changed instead to look at how emerging technologies can be used to minimise occupational radiation exposure.

However, while these new estimates allow more extended human intervention, future high luminosity colliders will need to anticipate robotic intervention when considering decommissioning, and incorporate this into the design of the equipment.

Due to the complexity, the time required to carry out the work, and the high level of radiation involved, the decommissioning is a Tier III intervention, (see chapter 2.4.3). Preparation for the upgrade and planning each section of work in high detail is necessary to get approval from the ALARA committee.

3.3.4 Decommissioning the ATLAS Inner Detector

As CERN prepares for the HL-LHC, several detectors need to be upgraded. The new components are designed to take full advantage of the increased luminosity. For ATLAS, this means replacing the existing Inner Detector (ID) with the new Inner Tracker (ITk), among other upgrades. The ID was designed to meet the requirements of the LHC over its lifetime - by LS3 it will have incurred significant radiation damage, and reached the end of its expected lifetime. As the HL-LHC will significantly increase the number of collisions and the fluence of particles through the detector, the ID must be upgraded to the ITk to meet the new requirements.

Decommissioning the ATLAS ID presents a unique challenge. No previous experiment decommissioned has been run for this long with such a high particle fluence. As a consequence, the radioactivity induced in the material of the experiment is much more intense than previously seen. Each intervention must be signed off by CERN's overarching Radiation Protection team before it can go ahead, however the timeline for the shutdown is strict. Due to the high levels of background radiation, personnel cannot be in the ATLAS cavern while the LHC machine is running, so any overruns in the ATLAS upgrade work will have a knock-on effect the entire LHC and all its dependencies. The cavern also requires cooldown time before the radiation levels are low enough for technicians enter.

Each section of the ATLAS detector has been designed to join together seamlessly. This is to allow the opening of the detector to facilitate maintenance work. There are two types of opening, **Standard** and **Large**. These two different configurations are shown in Fig. 22. Only a quarter of the detector is shown, as the detector is mirrored at the collision point and along the beam axis. For comparison with the setup for the different openings, Fig. 22a shows the detector closed and ready for particle collisions. In comparison, the Standard Opening shown in Fig. 22b, shows how the Endcap Toroid and Big Wheels are moved to the end of the cavern. The Endcap calorimeters are pushed to the end of the toroid loops (not depicted) to create space to access the Inner Detector. For the Large Opening, shown in Fig. 22c, the

Endcap Toroid is pushed out of the beam axis, into a side cavern, and the small wheel is lifted to the surface. This allows the Endcap Calorimeter to be pushed outside the toroid loops and onto a support cradle. This frees up around 12 m of space between the Endcap and Barrel Calorimeters. Similarly to the Standard Opening, a platform and scaffold are put in place in the gap, however the Large Opening has more space to lower components onto the platform. The Endcap on its cradle, the toroid loops and the platform are shown in Fig 23.

The major steps for the removal of the ATLAS ID have been listed in order below. Broadly, the decommissioning steps resemble a reverse order of the steps taken to install the ID, see chapter 3.3.

The work will be carried out with a Large Opening on Side C and Standard opening on Side A. The opening configurations are shown in Fig. 22. The ID Endplate cover will be removed to expose the services leading to Patch Panel 1. The services to each sub-component (data cables, cooling systems, power infrastructure, etc.) will be removed before the component itself. The beampipe, IBL and Pixel were constructed as self-contained units and will be removed whole. However the SCT/TRT can be divided into three pieces: the barrel and two endcaps, and will be removed in these sections accordingly.

The removal will be conducted from the innermost sub-component outwards, starting with the beampipe. Removal of the beampipe, IBL and Pixel will be on Side C, each with their own dedicated extraction tool. The Pixel will be moved from the Pixel Support Tube (PST) inside the SCT barrel, to the Dummy Support Tube (DST) for removal and transport. The preparatory steps to the removal of the beampipe, IBL, and the Pixel detector, are the steps of the ID decommissioning expected to have the largest radiation exposure. The beampipe, IBL and Pixel are the most irradiated and activated parts of the ID. They cannot be removed immediately, as their services - wiring, cooling tubes, etc, need to be removed beforehand, shown in Fig. 27. This is anticipated to be the highest occupational radiation exposure.

Figure 25 shows the steps of removing these services within the virtual environment created for this work (see Chapter 5), and 26, show the addition of rails and the dummy support tube which will be installed to facilitate the removal of the beampipe, IBL, and the ID Pixel. As these sections are a significant radiation source, once removed there is a significant drop in background radiation. As shown in Fig. 27, the beampipe, IBL, and Pixel cannot be removed without first removing their associated services. For this reason, the removal of the services are the most concerning part of the decommissioning from a radiological standpoint, and therefore are the focus of dose estimation for this thesis (see chapter 6).

The SCT/TRT Endcaps will be removed after the beampipe, IBL, Pixel. In order to facilitate this, the SCT/TRT services will also need to be removed beforehand (see Fig. 27, and 28. Firstly the SCT/TRT Endcap will be removed on Side C. The detector will then be changed to Large Opening on Side A for the SCT/TRT Endcap removal on that side. The PST will be left hanging in the air on both sides, and will be removed next (see Fig.

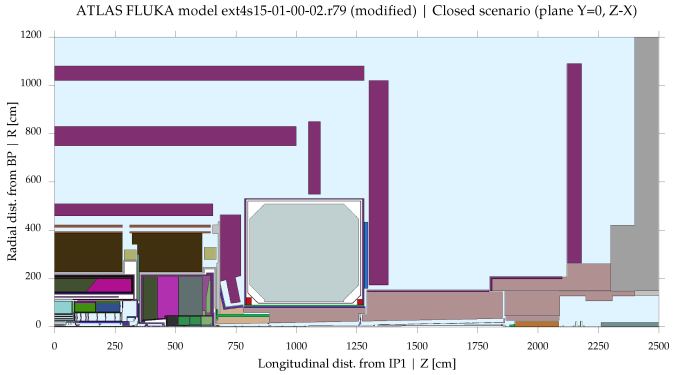

(a) Quadrant of the ATLAS Detector when closed and ready for beam on. The Endcap Toroid is represented by the grey square. The purple sections are the muon chambers. The ID is in the bottom left corner, between 0 and circa 300 cm along the Z axis, and 0 and circia 100 cm radially.

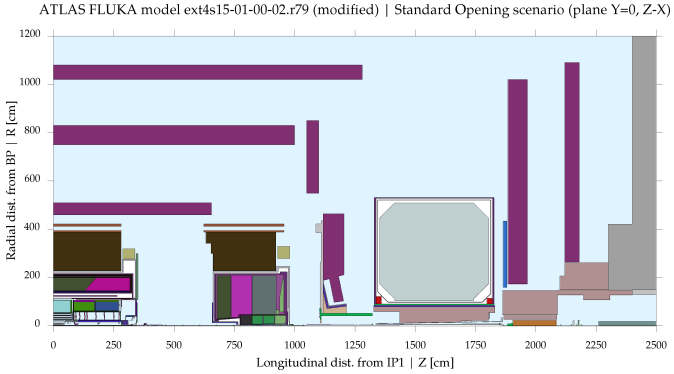

(b) Quadrant of the ATLAS detector in its Standard opening configuration, the Endcap Toroid and Big Wheels are pushed to the end of the cavern. Next, the Endcap Calorimeter and Small Wheel are moved to the end of the toroid loops. This creates a 3m gap between the Endcap and Barrel Calorimeters for access in which there is a platform, and a 1m-wide scaffold erected directly against the detector barrel and Inner Detector. All components are only moved along the z axis (along the beamline)

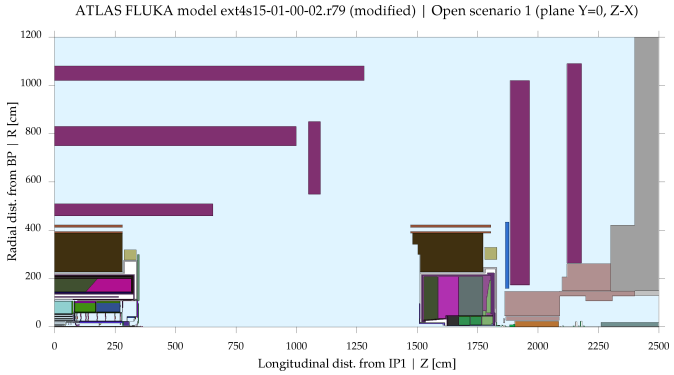

(c) Quadrant of the ATLAS in its Large opening. The Big Wheel and Endcap Toroid have been pushed back to the end of the cavern. The Endcap Toroid has been pushed into a side cavern. The Small Wheel has been lifted to the surface. Both are no longer visible on the schematic. The forward and endcap calorimeters are then pushed into the space left by the Endcap Toroid at the end of the cavern.

Figure 22: Different configurations of the ATLAS detector, to allow access for maintenance, taken from [88]

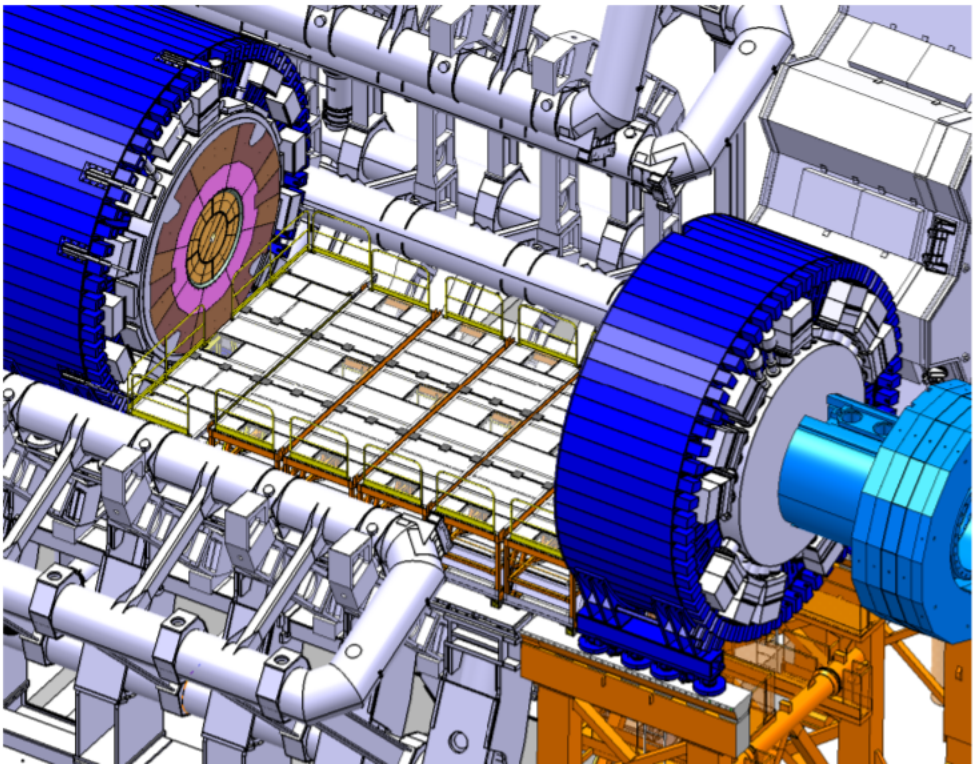

Figure 23: 3D render of ATLAS Large opening for the LS3 shutdown, both small wheels have been lifted to the surface. A platform floor has been installed for ID activities, however the scaffold to reach the ID is missing. Taken from [89]

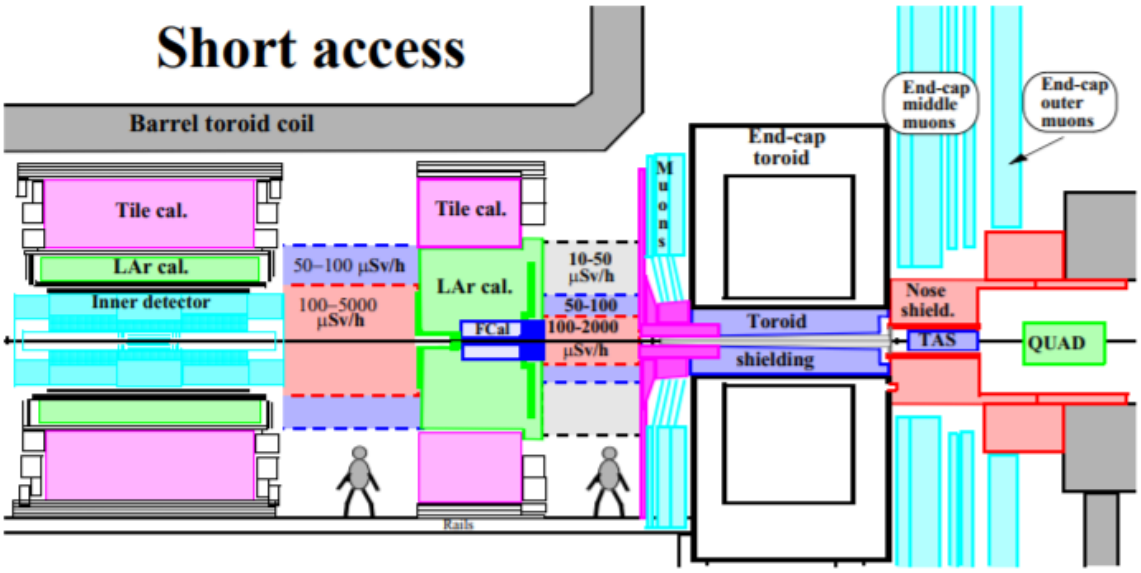

(a) The inner region of the ATLAS Standard opening scenario with radiation estimates from 10 years of operations at 10^{34} cm^{-2}s-1 and 5 days cooling. The beampipe is still in place. Taken from [13] (2008)

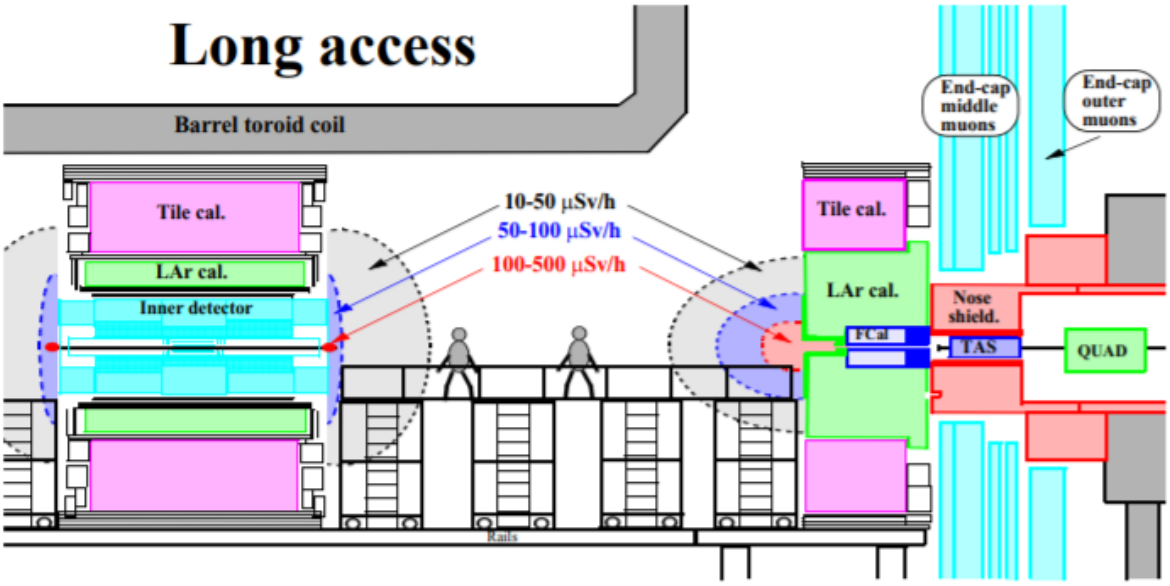

(b) ATLAS Large opening with radiation estimates from 10 years of operations at 10^{34} cm^{-2}s-1. Only the ID section of the beampipe is in place. Taken from [13] (2008)

Figure 24: Different opening configurations of the ATLAS detector with radiation estimations, taken from [13]

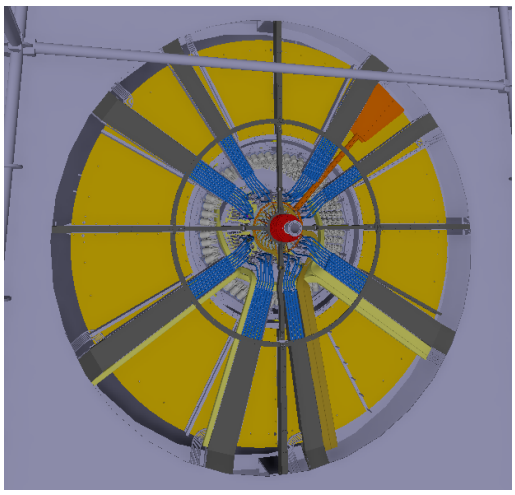

(a) The Inner Detector intact

(b) ID with the Endplate nose and Beampipe support removed

(c) ID with the outer ring removed

(d) ID with the heater trays removed

Figure 25

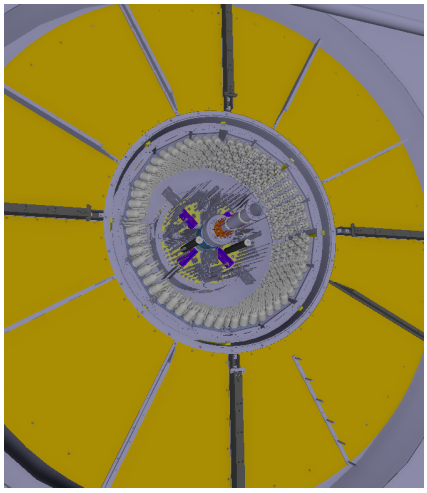

(a) ID with the Pixel services removed

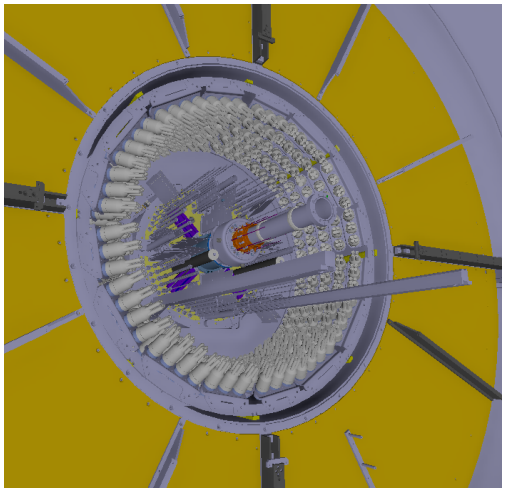

(b) ID with the pixel support tube rails

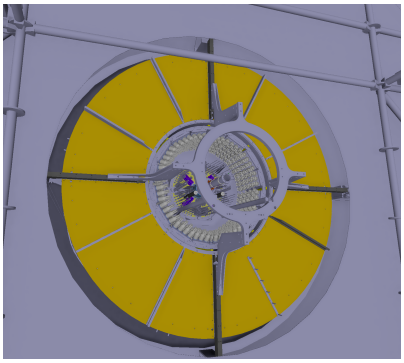

(c) ID with the Support ring added

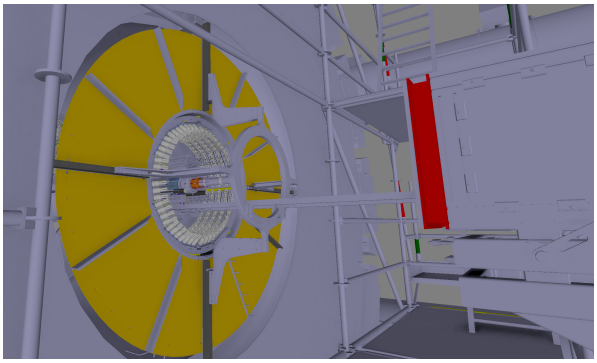

(d) ID with the transition rails and the dummy support tube in place

Figure 26

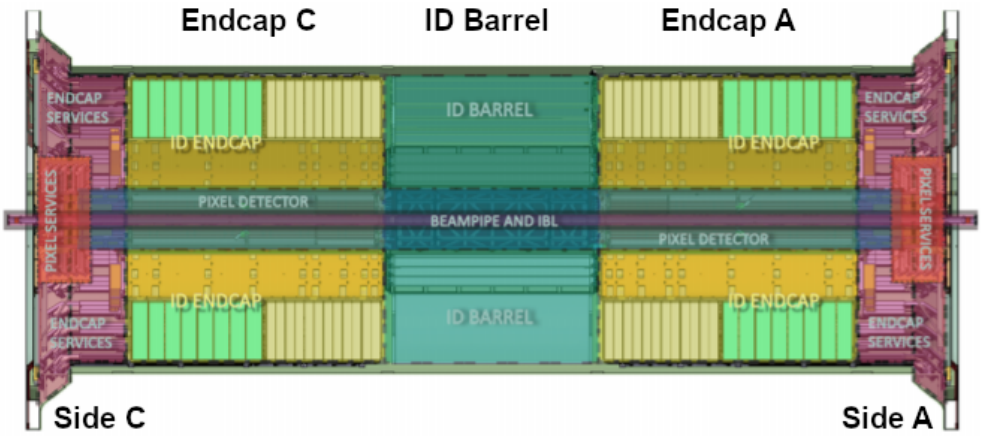

Figure 27: Cut-away of the ATLAS Inner Detector. The ID is segmented to illustrate how it will be dismantled. The SCT and TRT divided into three segments, two endcaps and the barrel. The Beampipe and Pixel are both self-contained and will be removed as whole units. Image from [87]

Figure 28: Photo of the ID barrel services with the cover removed, taken from [88]

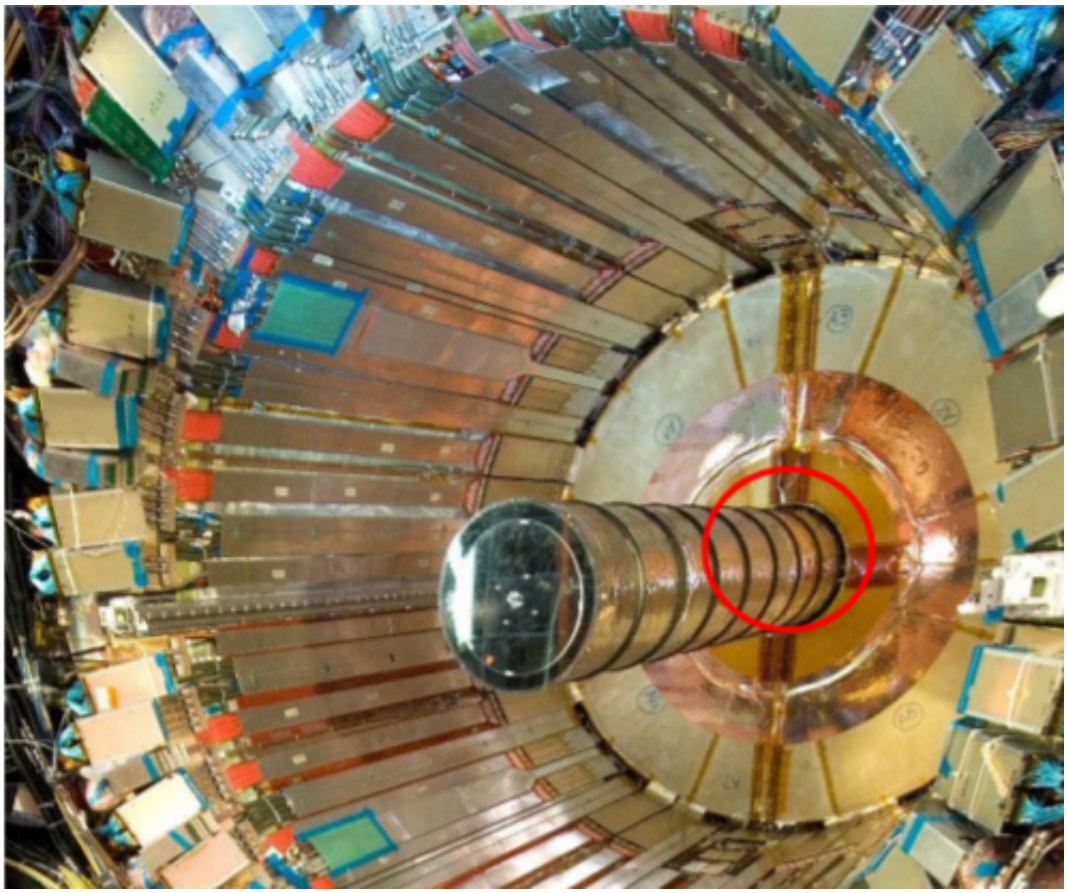

Figure 29: The PST hanging within the empty ID endcap during the ID installation, taken from [88]

29). Following which, the SCT/TRT barrel will be removed on Side A. After that has been accomplished, the entire ID will have been removed, ready for the new ITk to be installed for the HL-LHC.

4 Defining Virtual Reality

Virtual Reality (VR) is a multimedia visualisation technique where users experience and participate in an artificial surrogate 3D audio-visual (and sometimes tactile) environment. These virtual environments are computer generated; user interaction is generally aided by peripheral devices such as headsets and hand controllers [90].

There are many different types of computer-aided 'artificial' realities, and their definitions have migrated as technology advances. This work will use the taxonomy of Flavián et al. (2018) [91], who propose the spectrum of realities shown in Fig. 30. Their classification of digital realities is as follows: The 'real environment' is what we experience every day unaided by technological peripherals. In Augmented Reality, digital content is overlaid onto the physical world, 'augmenting' the user's perception. Augmented Virtuality is a lesser-used term, where physical objects are inserted into a Virtual environment, such as a sofa in a living room. For both Augmented Reality and Augmented Virtuality, (parts of) the physical world is both visible and relevant. Virtual Reality displaces the user to a virtual, completely digital, environment. Mixed Reality blends physical and virtual objects seamlessly - a stricter definition than previous works. Extended Reality is an umbrella term for Virtual Reality, Augmented Reality, Telepresence, and other related technologies.

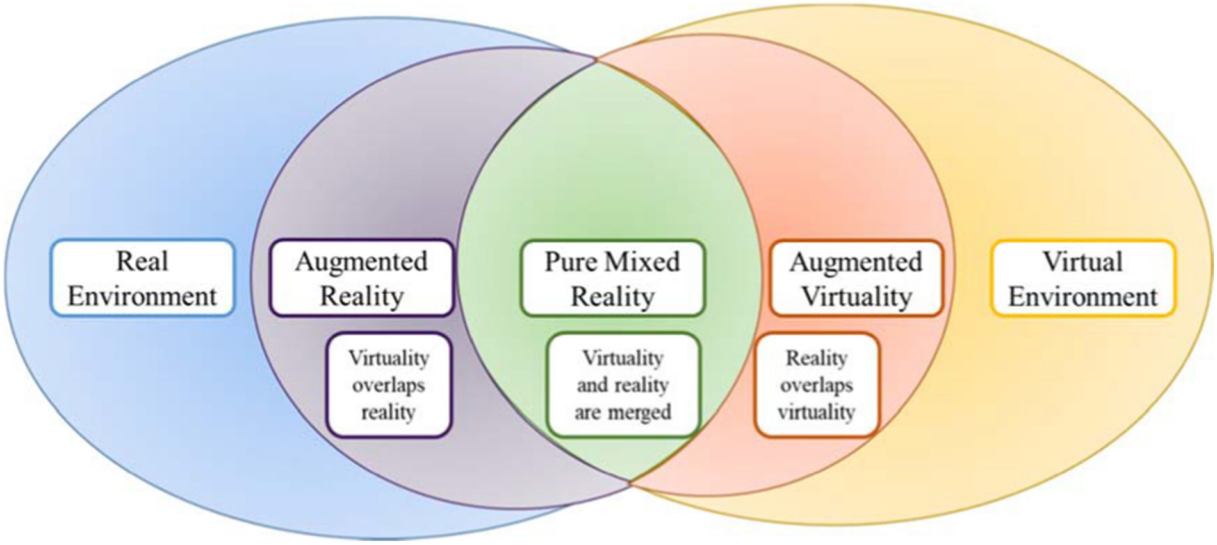

Figure 30: A Venn diagram showing the taxonomy of realities from Physical to Virtual from [91]

This work concentrates on Virtual Reality, where the user is disconnected from their physical surroundings. The aspects that define Virtual Reality, as opposed to other computer-aided realities, will be explored in this chapter. It will also give an overview of the base software used in this thesis: Virtalis Visionary Render [92].

There are 4 main aspects of Virtual Reality, and they feed into each other [93]. Each aspect will be briefly summarised, and then expanded on in their own subsection.

- **The virtual environment**: this is the artificial world constructed by a computer, commonly called a Computer Mediated Environment. It has a certain 3D space, it is populated by 3D objects, and there are rules that govern it (for example, a physics engine that implements physics concepts in the virtual environment, such as gravity, light, and object rigidity). Virtual Reality is the name for the interactive medium which presents the virtual environment to the user.

- **Sensory Feedback**: This is where VR straddles the line between physical reality and imagination. A person perceives physical reality on their own through sensory feedback such as sight and touch. An world that is purely imaginary (only constructed mentally) must be created with limited sensory information, while guided by an narrator or creator external to that world. In Virtual Reality, the user explores an artificial environment with sensory feedback. The virtual world experienced is directly built by the creator to reflect their vision and the user can explore this through sensory feedback.

- **Presence and Immersion**: With current technologies, a user is not likely to confuse physical and virtual realities, however immersion permits a suspension of disbelief to give a psychological 'sense of presence' when inside a virtual environment.

- **Interactivity and the free agency of the user**: The user's presence and actions have an effect on the virtual environment. This is the difference between Virtual Reality and Animation. Virtual Reality allows the user to explore and authentically interact with the environment at will, while animation is a passive experience and all actions are predetermined. Without user interaction, Virtual Reality is reduced to an animation of a computer rendered environment.

4.1 The Virtual Environment

Virtual environments have similar basic concepts and structures as open-world computer games. The environment most commonly consists of 3D Euclidean space and physics phenomena. The physics phenomena are governed by a physics engine and can include: light dispersal, gravity, Newtonian mechanics and fluid dynamics. A 'scene' is an instance of a virtual environment; referring to the visual scenario in VR, from the viewpoint of the user.

The difference between *virtual environment* and other similar terms like *virtual world* is still debated [94], [95]. This thesis will simply use virtual environment to avoid excessive jargon.

4.1.1 Assemblies

Assemblies are computer generated rigid-body objects that populate a virtual environment. Top-level assemblies are objects that exist independently of each other within the virtual environment. They can be comprised of an infinite number of child assemblies. A child assembly depends on its parent and can inherit certain properties. For example: the location and orientation of top-level assemblies are stored according to the world-coordinate system, whereas the placement of a child assembly is determined by its location and orientation relative to its parent. Each assembly (whether top-level or not) has its own relative, or local, coordinate system which only affects its children.

Local coordinate positioning is useful for grouping virtual objects together in a logical manner. When examining a car in virtual reality, conceivably the top-level assembly would be the whole car - which is to say, the collective grouping of each of the car components, like the engine, chassis, or suspension. Child assemblies would be the inner workings, such as a piston, or valve. These child assemblies could exist as top-level assemblies independent of the whole car, however this will later cause problems if the car needs to be rotated or translated within the virtual environment, as they lack the child-parent association assuring their relative positions within the car remain unchanged.

Most often, assemblies are created in software specifically aimed at Computer Aided Design (CAD) such as SolidWorks [96], and imported into another application geared towards VR interaction, like Virtalis Visionary Render [92].

4.1.2 Human avatars

For most VR environments, human avatars are implemented as a specific type of assembly. Instead of a multiple-rigid-body polyhedron, the humanoid shape is approximated by a structural skeleton with a deformable mesh covering.

External orientation and location of the avatar are set at the Pelvis, also sometimes called Root. From there, each joint of the skeleton are determined as a distance and angle from its predecessor. The skeletal structure of a human avatar is shown in Fig. 31. The number of articulated vertebrae can vary depending on the origin of the data. The solids representing the limbs are purely visual aides, the skeleton is invisible except as the underlying structure for the mesh overlay. Human avatars and their articulation are important to the motion capture algorithms employed in Chapter 6.1.2. Understanding how the avatars are located and orientated within the virtual environment is crucial for an accurate radiation dose estimation, see Chapter 5.3 and Chapter 6.2

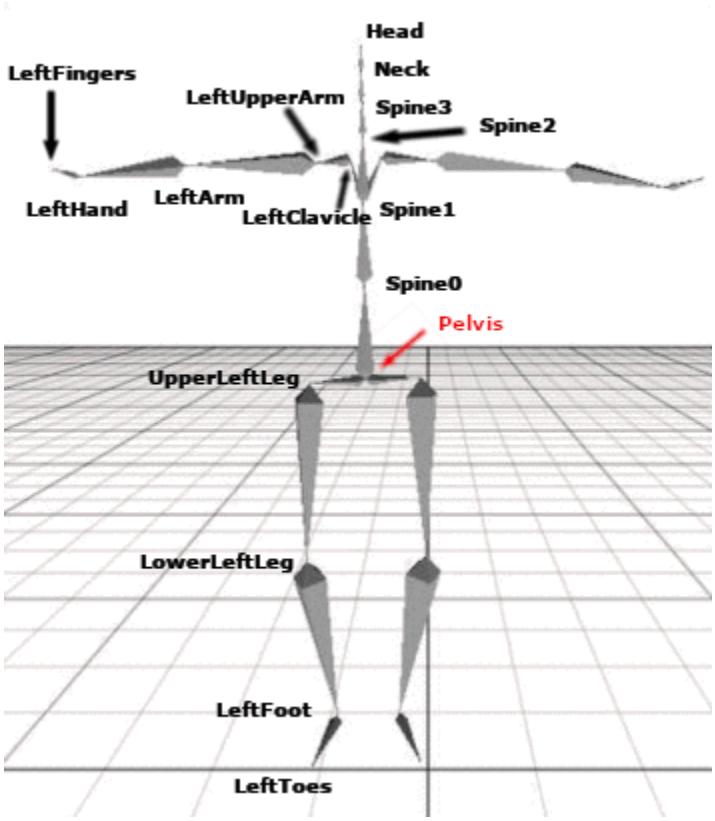

Figure 31: Skeletal model from Phasespace Recap2 software (colour inverted), with joints labelled.

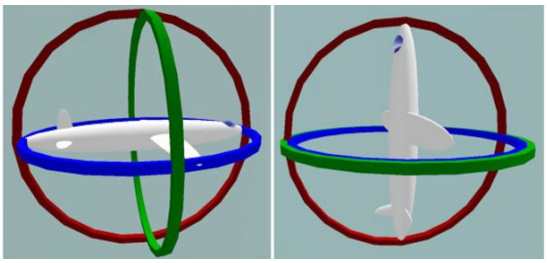

Figure 32: On the left: a normal 3 gimbal system. On the right: Two axes of rotation are aligned on the same plane, the system degenerates to 2 degrees of rotational freedom. Taken from [97].

4.1.3 Coordinate systems

Most Virtual environments use a 3D Cartesian coordinate system. However, 3D angles can be defined in multiple ways. Euler angles are a 3D rotation with respect to a fixed coordinate system, and are represented by three angles applied in succession to specific axes. Euler angles must be applied in the correct order, and to the chosen axes, to recreate the angle correctly. In addition, Euler angles can create a scenario where two of the rotation axes align and the system degenerates into a 2D system. This is known as Gimbal Lock and causes a three-gimbal system to lose a degree of freedom known, shown in Fig. 32.

Another method to define 3D angles are quaternions. A quaternion is a four-vector comprised of a real scalar term and an imaginary vector term. Euler's rotation theory postulates that any sequence of rotations about a fixed point can be simplified to one rotation of angle θ about a single vector-axis $\overrightarrow{u}$. Quaternions take advantage of this, and express the rotation as a complex number incorporating the Euler axis and the rotation θ, as shown in equations 5 and 6.

$$\mathbf{q} = \cos\frac{\theta}{2} + \left(u_x\mathbf{i} + u_y\mathbf{j} + u_z\mathbf{k}\right)\sin\frac{\theta}{2} \tag{5}$$

$$\mathbf{q} = e^{\theta/2\left(u_x\mathbf{i}+u_y\mathbf{j}+u_z\mathbf{k}\right)} \tag{6}$$

where

$$\mathbf{i}^2 = \mathbf{j}^2 = \mathbf{k}^2 = \mathbf{ijk} = -1 \tag{7}$$

This approach to 3D angles avoids Gimbal Lock, and avoids problems applying the angles in the correct order, as the axis information is contained within the quaternion value.

The conversion between yaw-pitch-roll applied to the z, y' and x" axes (ψ, θ, ϕ) Euler angles, and quaternions $\mathbf{q} = (q_i, q_j, q_k, q_r)$ is as follows:

$$q_i = \sin\frac{\phi}{2}\cos\frac{\theta}{2}\cos\frac{\psi}{2} - \cos\frac{\phi}{2}\sin\frac{\theta}{2}\sin\frac{\psi}{2}$$

$$q_j = \cos\frac{\phi}{2}\sin\frac{\theta}{2}\cos\frac{\psi}{2} + \sin\frac{\phi}{2}\cos\frac{\theta}{2}\sin\frac{\psi}{2}$$
$$q_k = \cos\frac{\phi}{2}\cos\frac{\theta}{2}\sin\frac{\psi}{2} - \sin\frac{\phi}{2}\sin\frac{\theta}{2}\cos\frac{\psi}{2}$$
$$q_r = \cos\frac{\phi}{2}\cos\frac{\theta}{2}\cos\frac{\psi}{2} + \sin\frac{\phi}{2}\sin\frac{\theta}{2}\sin\frac{\psi}{2}$$

4.2 Sensory Feedback Devices

Sensory devices are crucial to facilitate Human-Computer interaction and facilitating access to a Virtual environment. Besides the ubiquitous computer screen, keyboard and mouse, there are technologies specifically designed with 3D interactions in mind. The simplest navigation device is the 3D space-mouse, a joystick-like hand device that makes 3D navigation more intuitive than with an optical mouse. These are most often deployed with a computer screen setup.

The most obvious visual device is the head mounted display, or VR headset, which allows the user to view the virtual environment with an expanded field of view. Some headsets include headphones, permitting stereo auditory feedback. Hand controllers are the VR hardware equivalent of the space-mouse. They perform similar functions (navigation and interaction), however they are more suited to deployment with a VR headset as they are handheld and wireless. Some hand controllers have limited tactile feedback options like vibrations [98]. Tactile feedback is typically restricted to the hands through haptic gloves [99], though haptic shoes [100] and full body haptic suits do exist [101]. There is ongoing research into the faithful recreation of textures [102] and virtual ambient temperature [103], as well as more complex sensations such as humidity and air currents [104], [105]. Olfactory and gustatory feedback devices have also been developed to stimulate the users sense of smell and taste [106]. Naturally, the use of all these devices is restricted to platforms that support them.

4.3 Presence and Immersion

Immersion describes the vividness of an experience. It is a form of sensory deprivation, detaching a person from the physical world and immersing them instead in the mediated environment. In virtual environments, the quality of technology arbitrates the depth of immersion [107].

Presence is the psychological term for the 'sense of being there', the conviction of being located within a specific environment. There are several definitions outlining spatial 'presence'. These largely agree on the base concept, however different authors diverge on its boundaries [108]. The base concept states: Presence is an unconscious mental exercise that a person is continuously engaged in. Through sensory feedback cues, a person mentally constructs a credible spatial environment, and perceives themselves as located within that

same environment. The 'state of presence' is binary - either a person is convinced they are located within an environment or they are not [108]. It also stipulates that the user's perception of agency is restricted to their environment [109]. For example, if a user is 'present' in the virtual environment (and therefore oblivious to their physical surroundings), they can only conceive of actions based within the virtual environment.

The engagement of multiple senses increases the probability for a user to experience 'state of presence' [107], and although a user does not necessarily *require* external sensory feedback to obtain a 'state of presence' (known as the book problem), it does enrich the experience [108]. Multiple sensory feedback can be combined with interesting effects on the user, such as creating the illusion that a user's hand possessed a (functioning and responsive) sixth digit [110]. However sensory feedback must be congruent, i.e. overlapping information must be redundant. Any discrepancy between feedback has an adverse effect on the credibility of the scenario [110].

Some users of VR experience cybersickness. This is usually prompted by sensory mismatch and a visual–vestibular conflict [111], and studies have concluded an inverse relationship between cybersickness and presence - that is to say a person experiencing a more steady 'state of presence' is less likely to suffer from cybersickness, and a person experiencing subconsciously less convinced of the virtual scenario's authenticity is more likely to feel ill [112].

This relationship could explain why sudden interruptions to a VR experience are so disconcerting, such as when a user bumps into a physical wall not present in the virtual environment, or hears someone speak who has no virtual avatar. These jolts of physical awareness are in conflict with the self-localisation aspect of the user's sense of presence.

4.4 Interactivity

Since biblical times, free will has been seen as a fundamental human trait. Creating an artificial environment would therefore need to enable some measure of user agency, starting with the basic ability to navigate the virtual space at will. Some philosophers postulate that human experience is defined by social interactions with other humans. Without the presence of the 'other' the 'self' cannot be conceived [113].

Following this line of thought, virtual reality should enable social as well as environmental interactions. This can be accomplished with users coexisting in the same virtual environment (low socialisation), but also through voice chat, digitised facial expressions and body language (high socialisation).

5 Development of an Integrated System for Radiation Personnel Intervention Planning using Immersive Technologies

Virtual Reality disassociates the user and the physical environment. By creating a virtual facsimile of the ATLAS detector, a technician can practise the ID decommissioning - for training or radiation dose estimation purposes - without physical exposure to radiation. This chapter will present the VR platform developed to respond to this idea. Firstly, it will present the base hardware and software tools used for the platform, as well as the platform's scope and the main aims of its design. Secondly it will present the platform's proof of concept using the vault of the cyclotron at the University of Birmingham.

5.1 Virtalis Visionary Render

Virtalis Visionary Render 2.1.0 is the base software used in this thesis. It has a pre-loaded physics engine that can restrict users and objects to the laws of classical mechanics, and provides lighting and material effects. This creates a virtual 3D space which can then populated with CAD models. The software has only a limited capability to manipulate CAD objects when inside the environment. It can also create basic geometric volumes.

A user can interact with these virtual objects with either standard computer peripheral devices such as a mouse, or peripherals designed for virtual reality such as the HTC Vive headset and hand controllers, shown in Fig. 33. These peripherals are connected to Virtalis Visionary Render through the SteamVR interface [114]. Virtalis Visionary Render provides the ability to deploy custom Lua scripts that can modify the virtual scene. Lua is a high-level interpreted object-orientated programming language. It is embedded in Visionary Render and allows task automation and extends the functionality of the base platform. The scripts cannot directly alter how the base platform operates, however any task the user can accomplish can be automated by a Lua script - changing settings, moving or removing objects, modifying object properties, etc. Lua can also be used to import external data, from csv files for example. Custom Lua scripts make up the base of the intervention planning platform developed for this work. They provide all the automated functionality of the platform - the base dosimetry, the ability to reset the environment to its previous state, workstations to provide extra information etc. Lua scripts in Visionary Render can have different triggers, over which Visionary Render assumes complete control. There are set types of triggers, for example 'timed' where the script is executed periodically at user-defined intervals, and 'click' which will run when a user clicks the trigger object.

However there are limits to custom scripts in Visionary Render. The script can add functionality and automation to a scene, however it cannot change the platform itself. For

example, Lua scripts cannot create new script triggers, or change how Visionary Render renders the virtual scene. A script completes within a single frame - that is to say that the platform will not update the scene while the script is executing. Scripts that take too long to run are either killed by the software, or cause it to crash. Deployment of asynchronous scripts is not possible. Timing in Visionary Render is tied to the computer's internal clock, as well as run speed of scripts that are executed. Inefficient scripts can cause noticeable freezing of the scene during execution. The accuracy of the time delay between periodic script execution is also affected, as 'time' is frozen until the script has finished executing. Anything that should deploy while another script is running is executed after the script in-progress has finished. High frequency scripts are more susceptible to clock-based uncertainties as the execution time of the script becomes non-negligible compared to the wait time between script executions. Trigger functionality is prescriptive and cannot be altered or intercepted. Scripts can be disabled however.

Virtalis Visionary Render also allows multiple users to connect to the original 'master' copy of the virtual environment via the local network. This enables several people to interact within the same virtual environment, or scene, simultaneously.

The above describes the framework provided by Visionary Render as the base software, with the creation of extra functionalities possible with custom scripts within the scripting setup. Using existing technology and commercial-off-the-shelf hardware as the framework for a Virtual Reality platform provides a stable base level from which to work, as well as access to technical support.

5.2 Technical implementation of the Dosimetry Platform

This section will discuss the scope of the VR Intervention planning platform, its design and implementation.

Simulating an irradiated environment is a unique way to assess the environment without unnecessary exposure risk. The platform can be used for various radiation critical interventions, where detailed CAD drawings and radiation dose maps are readily available. The platform was designed with two distinct use cases in mind - intervention planning and intervention training. While the radiation dosimetry implementation is the same for both cases, there are additional functionalities aimed at a specific use case for the platform, which will be expanded on below. A VR headset and controllers allow an immersive experience of the rendered area. The system follows all personnel within the setup, tracking their movements and radiation dose. The platform deploys custom Lua scripts that provide access to an external csv dose map. The individual dosimeters periodically (every 0.125s) check users' location within the virtual environment and look up the dose associated with that point in space. The instantaneous dose and total dose, location data, time, and radiation map are

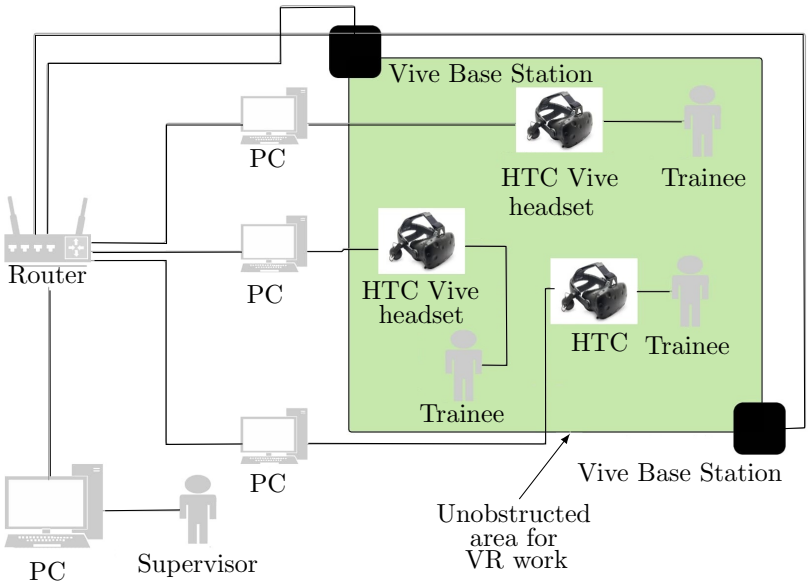

Figure 33: Diagram of the hardware setup for the Virtual Reality dosimeter. The HTC Vive headset uses two base-station towers that scan in infrared to track the user around an unobstructed physical area. The hand controllers allow the user to interact with the virtual environment, such as move virtual objects. For movements that would be too large for the delimited area, the Vive hand controllers can translate or teleport the user inside the virtual environment

logged in an external csv file, to allow for data auditing. The platform also displays the instantaneous dose and total dose of each users overall exposure on individual Heads-Up displays (HUDs). The HUDs are virtual GUI objects that are scripted to appear just in front of each worker's line of sight, but not to obstruct their view of the virtual environment as a whole.

Informative guidance points, also called workpoints, were conceived for an immersive training use case of the platform [115]. The guidance points show predetermined areas of intervention, with an estimated time required for work needed, and the associated radiation dose for that area. They comprise of a large green dot on the floor, with a floating billboard displaying relevant information (estimated time required for the work, radiation dose map, dose rate and estimated total dose exposure at approx. chest height, etc). These guidance points were designed to be interactive and be modified to better reflect intervention activities. The guidance points are moveable and the estimated time can be modified within the scene. The radiation information automatically updates when these parameters are modified. The functionality of the points was provided by custom Lua scripts, and the information displayed can be saved and loaded from an external file. The guidance points were re-purposed for the proof of concept - see chapter 5.3.

Motion capture and animation were used in the second use case of the VR platform: the review of radiation exposure from existing location data. An animated worker follows the 3D-motion path given by the motion capture coordinates, and its dosimeter performs the same task as with VR users, periodically looking up the instantaneous radiation dose based the location of the avatar's chest, and records their radiation exposure. This application allows for more intuitive identification of high risk areas, and offers a confirmation for other RP analyses [115].

In both use cases, the platform combines existing CAD models of the ATLAS detector with radiation dose maps from an improved radiation simulation (FLUKA). The 3D virtual environment created can lookup the instantaneous dose rate with respect to position - of users or virtual objects - within the environment. As activated components are removed from the detector, the radiation dose map is scripted to change accordingly.

In the process of developing the VR Intervention planning platform for this thesis, three virtual environments were created. The first was the location of the proof of concept - the Birmingham Cyclotron vault (see chap 5.3). The second is an accurate render of the ATLAS ID Mockup. The physical Mockup at CERN was created to train for the installation of the inner pixel detector, as well as to assess its wiring. The Mockup has subsequently been refurbished for the ID decommissioning. The Mockup provides an accurate stand in for the detector itself, including wiring and the surrounding scaffolding and platforms. This was a placeholder world for the platform's development, and will not feature further in this thesis. The last world is a large render of the detector itself. This was the final world created, and

into which the motion capture results were eventually imported. This was preferred over the Mockup as it provided a more detailed context for the data, as well as more accurately portraying the limits on the technician's field of vision (see chap 6).

The VR intervention planning platform was conceived and designed to give users the maximum amount of agency while in the environment [115]. Users can move and interact with the environment at will using either a VR headset with hand controllers, or a flat screen and 3D space-mouse. The aim was to provide a realistic environment to help plan one-time interventions where there is a significant dose risk, and no previous similar circumstances to exploit. A realistic facsimile where workers can practise jobs without physical exposure to radiation and supervisors can oversee the expected radiation doses for each intervention. As the application of the platform was centred around mimicking reality, some interactivity features were curbed or disabled on some object - this was to prevent users from performing unphysical actions such as resizing virtual objects.

Two distinct types of user were identified for the scope of this VR platform: the trainee and/or worker, and the trainer and/or supervisor. In every environment there is one supervisor using a flat screen computer display and 3D space-mouse, with the option of one or multiple workers immersed in the VR environment via headsets. The Heads Up Displays (HUDs) for the two types or user were customised to reflect their different needs.

The supervisor controls the environment, task allocation, trainees' starting conditions, and oversees the scene. They can control the environment using script-enabled buttons on their HUD. The supervisor HUD's environment-altering functionality is unique within the platform. The supervisor's scripts were designed to facilitate their job overseeing the scene with the workers. For example, one script resets the simulation, moving the scene's assemblies back to their initial configuration. Another script initialises every worker, moving them to their starting point and providing their dosimeters and logging scripts. The supervisor can start, pause and reset all dosimeters and logging activities. A screenshot of the supervisor's screen can be seen in Fig. 34, showing the buttons for the different custom scripts.

The supervisor shares the VR environment with the workers via Virtalis Visionary Render's network capability. This is limited to the local network, meaning that without the use of a VPN, by necessity the supervisor and workers will be in close proximity. A diagram of the hardware setup is provided by Fig. 33.

Workers can move and interact with the virtual environment freely - for example, moving objects. Each worker can see on their HUD their own integrated radiation dose and current instantaneous radiation dose - much the same as a physical personal dosimeter. They can control their own dosimeter, such as pause and reset if needed. It appears similar to the supervisor's HUD, though its functionality is very limited.

Fig. 35 shows an operational diagram depicting how the platform responds to different user actions, as well as the scripts working behind the scenes to provide the dosimetry functionality.

Visionary Render is constantly tracking the users within an open scene, while a custom script triggers every 0.125 s to lookup the dose in the user's location and update their dosimeter. The guidance points are created in locations set in an external file. The points were designed to be sequential, and only one point is visible at a time. A custom script triggers on approach, starting a timed script which will disable the point when the timer runs out. The next guidance point is then enabled, and the cycle continues. These guidance points are used in the platform's proof of concept, in section 5.3.

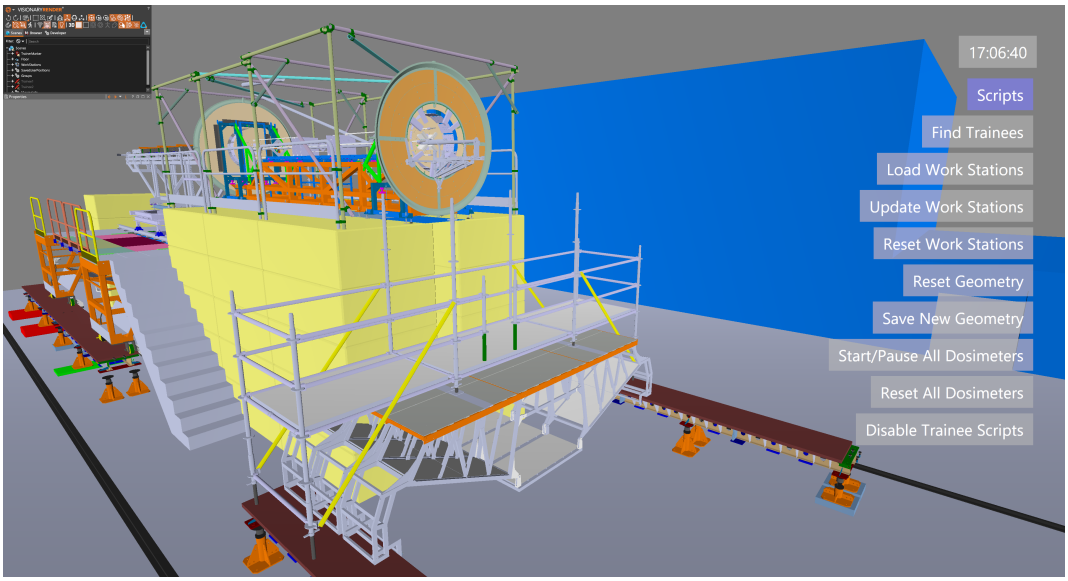

Figure 34: A supervisor overlooking the ATLAS virtual Mockup. On the right hand side the script buttons on their HUD are visible. Currently gravity is turned off.

Permanently saving the radiation dose map data inside Virtalis was not feasible. Instead, a script was created to load the data as needed from an external csv file. When the scene is opened, the first radiation dose map is loaded as a read-only 2D array variable (see chap: 3.3.3). During run-time other radiation dose maps can be loaded and swapped into the scenario. A change of radiation dose map can be triggered by any single or combination of predetermined events, such as a timer, or objects being moved. Dosimetry is implemented as a timed script that takes the user's location and looks up the appropriate radiation dose, and adding it to the user's running total. The platform's dosimetry is reliant on consistent and accurate timing. However, the uncertainty of timing in Visionary Render is heightened for timed scripts running at high frequency. This puts a minimum interval at which the dosimetry scripts can be triggered while still returning reliable results. Here, dosimetry scripts are triggered every 0.125 seconds.

User tasks are also stored in a csv file. Dynamic guidance points are created in predefined locations of the environment depending on the task setup. They appear as green disc-shaped

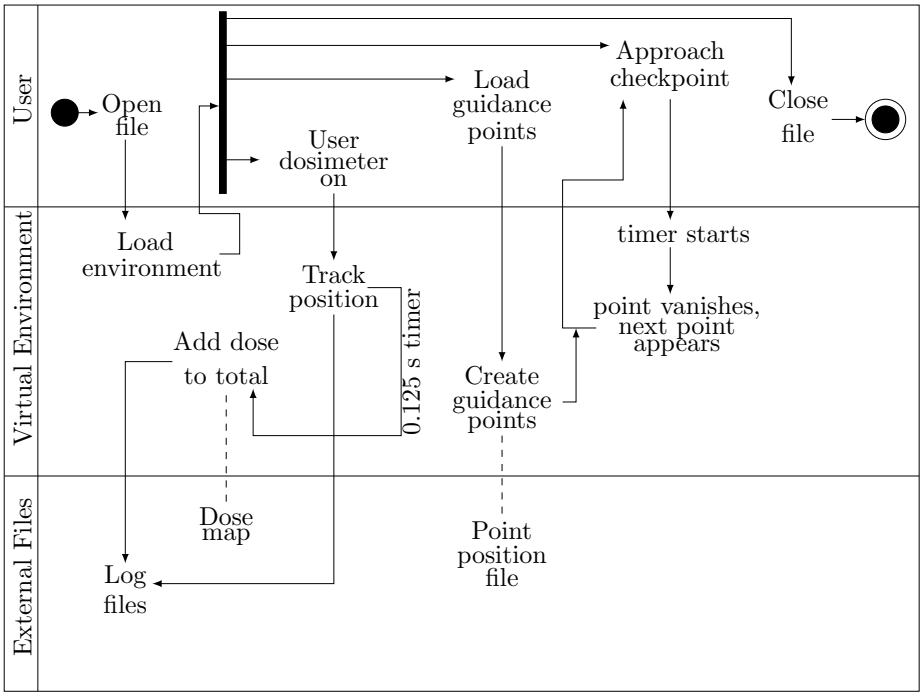

Figure 35: Non exhaustive operational diagram of user actions in the software.

Top: User actions, eg. turn on dosimeter.
Middle: Virtual Environment: behind-the-scenes scripts, eg. the dosimeter runs every 0.125 seconds.
Bottom: External Files: different external files accessed by the scripts, eg. the dosimeter logs position and dose data. Dotted lines denotes read-only (note for readability the actions to alter the guidance points and save changes to the point position file has not been represented).

floor markers inside the virtual environment, as shown in Fig. 36. The guidance points display relevant information regarding the task (the task's name, allocated time for the task's completion, the instantaneous radiation dose in that spot, a prediction of the radiation exposure, etc) on a virtual GUI display panel above them.

The guidance points are designed to be helpful information points, and also act as as guide to locating the next stage of the work. This is implemented by only having one guidance point - the one relevant to the user's task - visible at any one time. After a pre-defined interval, the current guidance point disappears, and the next guidance point appears. guidance points can be modified and their settings updated to tailor a situation, and provide as much or as little information to the workers as needed.

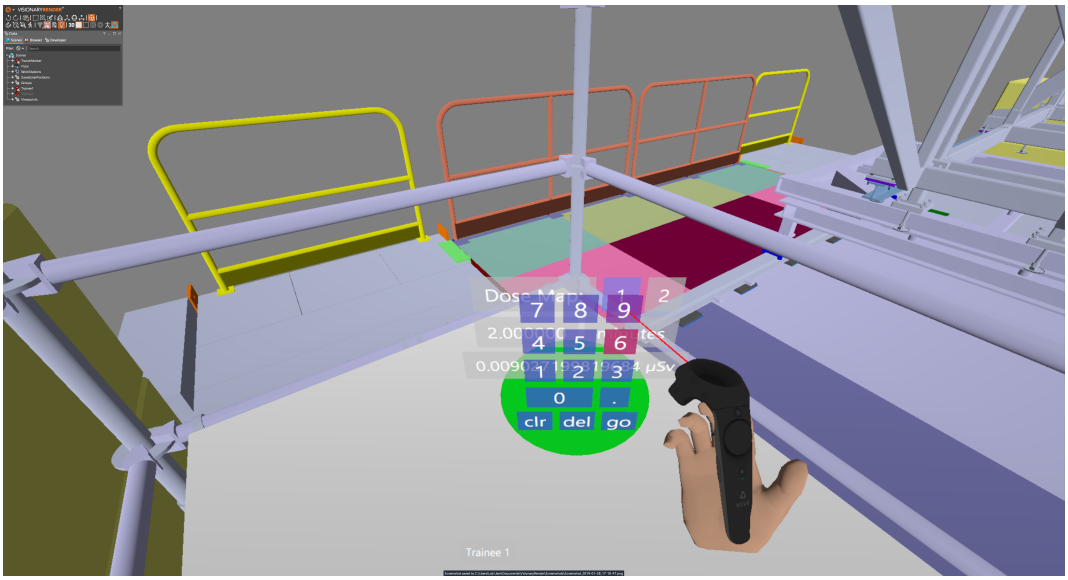

Figure 36: Working inside the VR. A guidance point being modified by a worker wearing a VR headset inside the ATLAS Mockup platform. The hand controller is visible, and the worker is changing the time estimate for the task associated with this guidance point. Once the input is confirmed, the guidance point will recalculate the dose estimate using the new time estimate. The worker HUD is collapsed out of the way at the bottom of the image.

5.3 Establishing proof of concept inside the Birmingham Cyclotron Vault

This section will discuss the work undertaken for the proof of concept of the VR intervention planning platform. Establishing the proof of concept required choosing an environment where both the geometry and radiation were known.

The concrete vault which houses the Scanditronix MC40 cyclotron at the University of Birmingham was chosen as the location for the proof of concept for its relatively small size, high radiation environment and ease of access. In order to prove the VR platform returned

reliable results, a circuit was planned through the vault. The instantaneous radiation dose and the integrated radiation dose of the virtual and physical walkthroughs were then compared to determine if the radiation exposure was comparable.

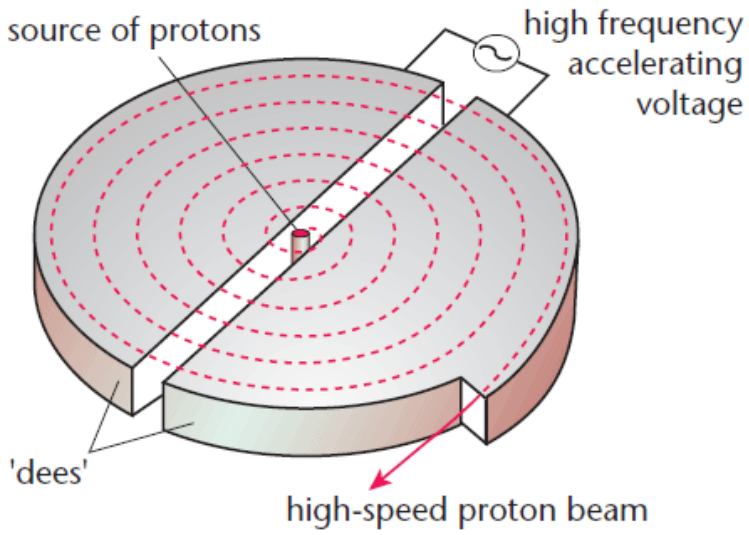

Figure 37: Diagram of a cyclotron, magnetic field not shown, taken from [116].

A cyclotron is a particle accelerator in which charged particles are accelerated as they orbit within a magnetic field. The circular area is divided into two D-shaped regions ("Dees"), one of which has an alternating potential applied, while the other is earthed, shown in Fig. 37. Protons are produced from an ion source near the centre of the cyclotron. A uniform magnetic field $\overrightarrow{B}$ exerts a force perpendicular to their direction of motion, the so-called Lorentz force. The protons therefore execute circular orbits within the magnetic field. The protons gain energy from the potential difference when they cross the gap between the two "Dees", increasing their velocity. This causes the radius of their orbit to increase. The protons spiral outwards, gaining energy and velocity on each orbit.

The irradiation facility in the Medical Physics department uses the cyclotron to produce a beam of protons of energy up to 40 MeV. It was commissioned to create Krypton radionuclides for UK hospitals. It is also the ATLAS-UK irradiation facility and is used to evaluate radiation tolerance for detector components up to their expected lifetime radiation fluence for the HL-LHC upgrade. It also carries out irradiations for industry hardware [117]–[119]. The protons exit the Birmingham cyclotron in a 1cm^2 collimated beam. The beam has an energy of up to 40 MeV and currents up to 2 μA, and can reach fluences in the order of 10^{15} 1 MeV neq/cm^2 in minutes. Beam fluence is determined offline by measuring the activity of nickel foils, or online by using a Faraday Cup (a metal cup which is designed to catch charged particles and measure the resulting current). A switching magnet directs the beam in one of

12 possible directions. This allows for the facility's long term irradiation commitments to have their own experimental 'area'. These include the creation of medical radioisotopes; PEPT, and adapted PET for engineering; radiation hardness testing for the HL-LHC and other partners. Each of these have different irradiation parameters and experimental requirements.

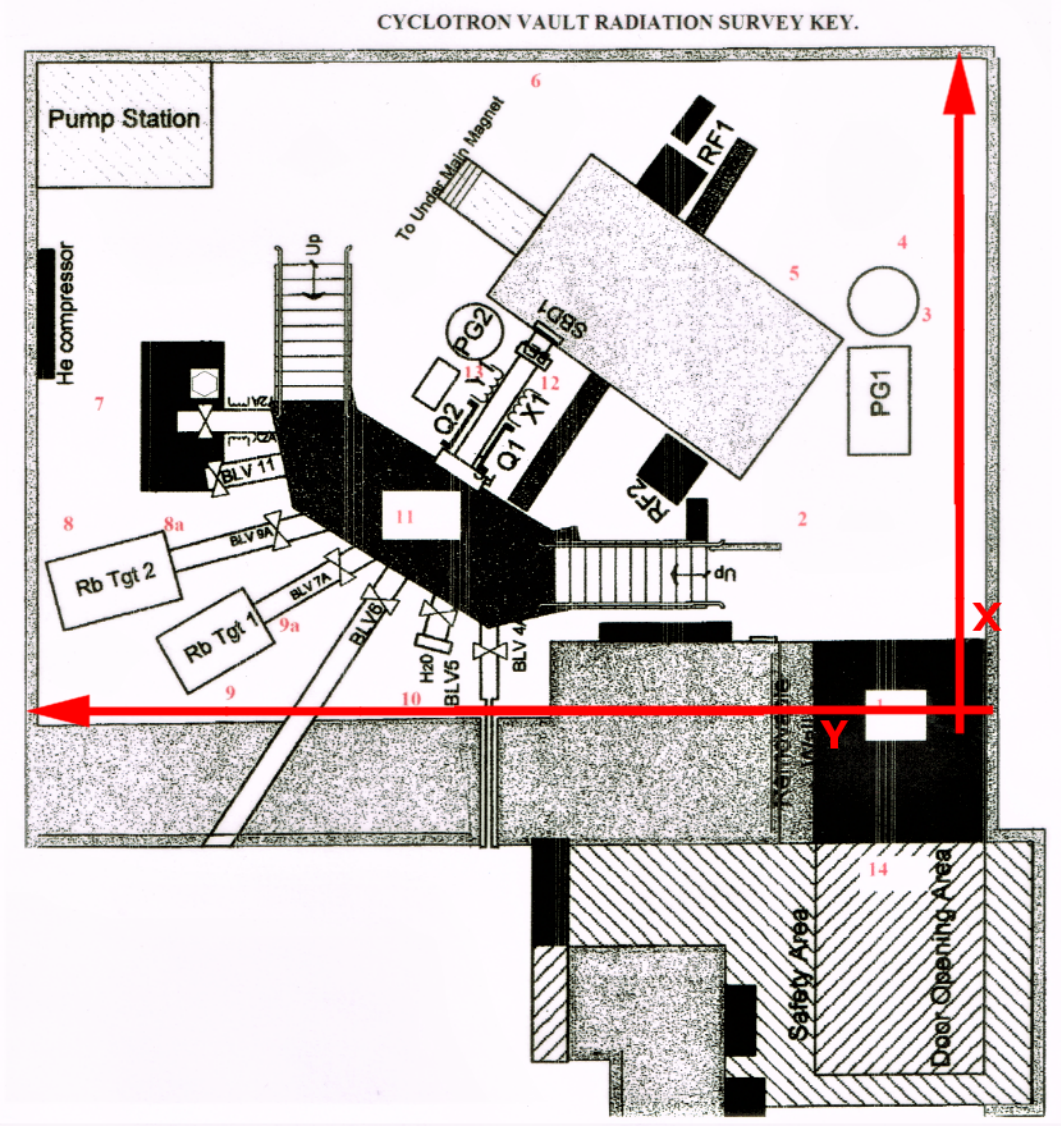

Figure 38: 2D map of the vault, with survey measurement locations. The vault is approx 8.9×8.1 m^2.

The University of Birmingham Physics department take monthly measurements of the background radiation inside the cyclotron vault, however the location of the measurements is strategic to monitor particle backscatter from the cyclotron machine. The location of these measurements is indicated by the red numbers in Figs 38 and 39. The background radiation varies greatly in some areas, providing a well suited environment to conduct a proof of concept

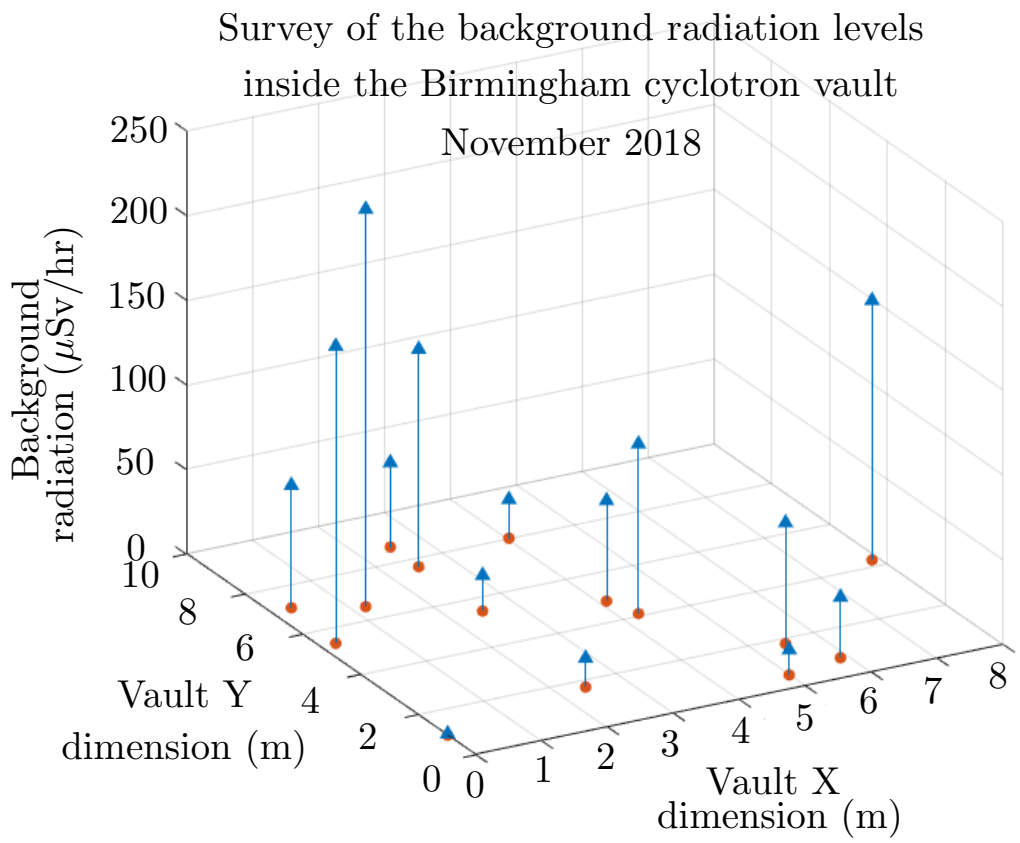

Figure 39: Background radiation levels from the November 2018 survey.

text of the VR platform.

5.3.1 Creating a 3D model of vault

The vault housing the cyclotron at the University of Birmingham is 8.9×8.1 m^2. The interior structures were modelled using the Microsoft Hololens scanning ability [120], backed up by physical measurements and simplified geometry.

Fig. 40 shows a comparison of photos taken from inside the vault with screen-caps taken from Virtalis Visionary Render. Scenic details that didn't impede human movement, such as wiring, were considered unnecessary to recreate. Inaccessible areas were deliberately made impenetrable in the virtual environment. For example, there is an access hole in the floor - shown by either the physical ladder handles or as a white square near the virtual person in Fig. 40a. This was made impenetrable to prevent unphysical actions, such as falling through the access hole or stepping in mid-air. The geometry of some constructs which were less relevant for the work were simplified by using convenient 3D stock models (the virtual red barrel replacing the physical white electrics box) instead of a more faithful recreation.

5.3.2 Creating a 3D dose-map from physical measurements

The background survey measurements are too granular and do not provide enough coverage to use as a comprehensive radiation dose map in the VR platform. Instead a new set of measurements was required to create the radiation dose map with the requisite accuracy.

The cyclotron is used overnight to create radionuclides for UK hospitals, therefore the machine has a strict availability cut-off each afternoon. The radiation profile within the vault is affected by the recent run parameters of the cyclotron, so the measurements for the dose map need to be taken in one day. The vault is only accessible with the cyclotron turned off, such as when the machine is undergoing its scheduled weekly maintenance. The measurements were taken manually using a Tracerco Personal Electronic Dosimeter (PED) Blues [121]. The measurements were taken in a grid system. The origin of the grid was the corner of the vault next to the doorway, and the floor was marked where measurements were taken. The time constraints severely limited the number of measurements it was possible to make. A 2 m pole with 0.5 m notches was used to measure the grid points. Measurements were taken from floor level to a maximum 3.8 m high. The measurements were taken across the accessible areas inside the vault, from the floor to 2 m in Z. The radiation levels across the bridge (which is 1.8 m tall) was also measured, meaning the final dose map covers 0 to 3.8 m in Z. As each successive grid point relies to the accuracy of its predecessor, the XY position of the measurements has greater uncertainty further from the grid origin, especially in places where the position measurement was restricted, such as around the beamlines. Previously unknown gaps in the cyclotron shielding were discovered while the background radiation survey was

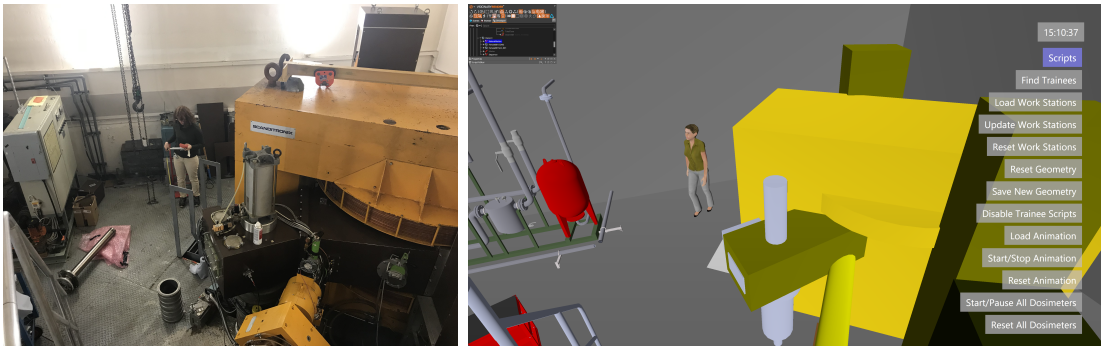

(a)

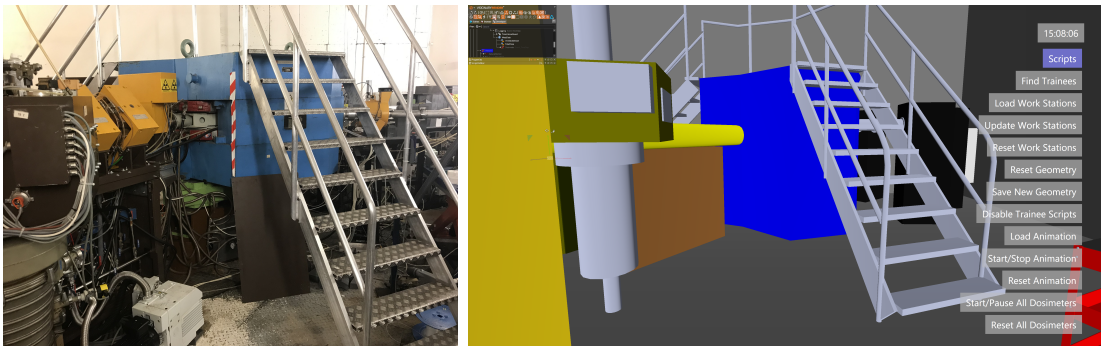

(b)

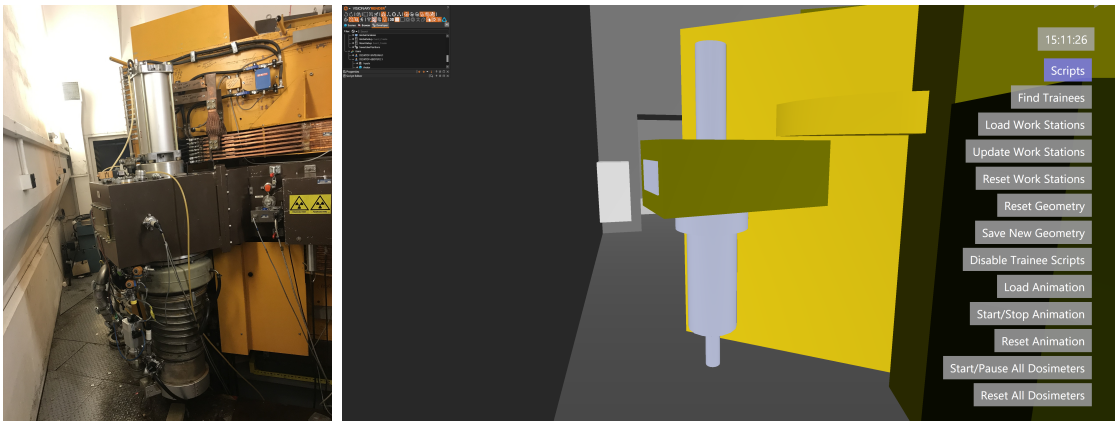

(c)

Figure 40: Comparison of the Vault with its virtual double. The cyclotron casing is the large yellow cube, the gantry above the beamlines is blue.
a) From the gantry above the beam lines towards the cyclotron.
b) From the back of the cyclotron towards the gantry.
c) From behind the cyclotron towards the entrance.

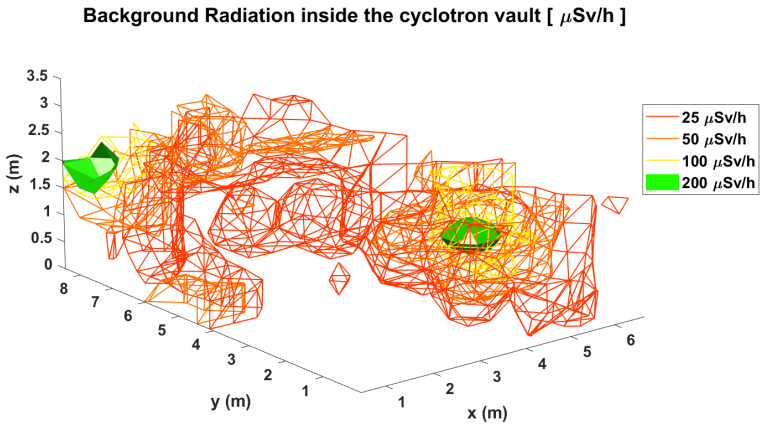

Figure 41: Intermediary radiation dose map, resolution 0.5 m.

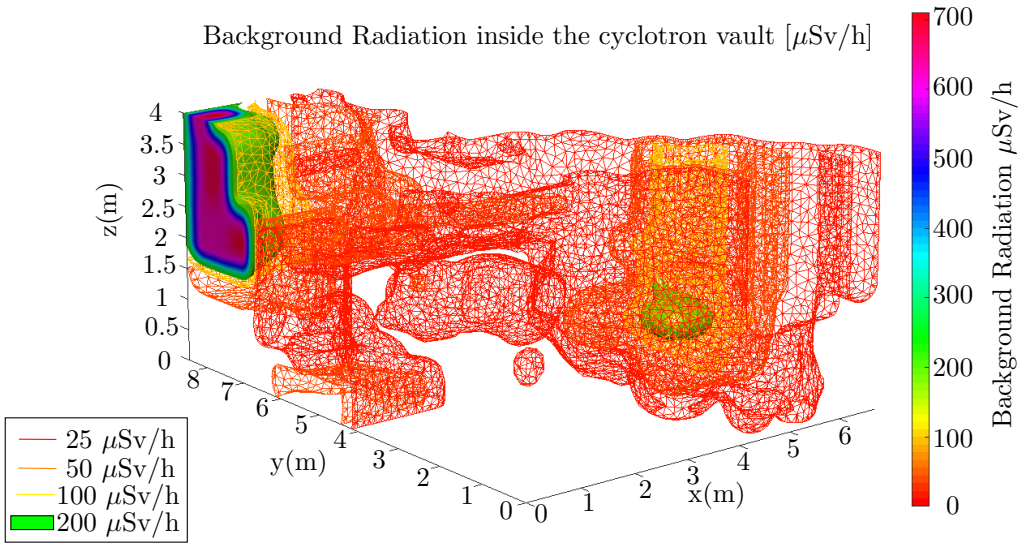

Figure 42: Final radiation dose map, resolution 5 cm.

being conducted - however these radiation spikes did not necessarily align with points on the measurement grid. This demonstrates the limitation of using a grid system to map background radiation. The radiation spike was not detected in proximity to the gap in the shielding, and so were not accurately tracked in the radiation map. Instead it was measured several meters away. This means there is a beam of high radiation inside the vault that the radiation map does not document. The spike was likely unnoticed as it was identified in above the beamlines in the vault, and area that was difficult to access. However, once the gap in the shielding had been identified, technicians at the cyclotron could work to rectify the problem and make the vault safer for future maintenance work. Any changes in the shielding would have a knock-on effect to the map. Unfortunately due to time constraints, subsequent radiation measurements inside the vault were not possible.

The raw data only provided the background radiation within the empty space inside the vault. It had gaps in the inaccessible areas where measurements couldn't be taken, such as within the cyclotron machine, and in between the beamlines. This raw data was initially interpolated used Matlab's Scattered Interpolant function using the nearest neighbour method to fill in the gaps in the grid, from which the first radiation map was plotted, Figure 41. The map was created using Iso2mesh [122], a 3rd party Matlab toolbox designed to create 3D volumetric images. The plotting function required the gaps in the grid to be filled before the mesh could be created.

The intermediate map consisted of a grid of 0.5 m granularity. There were regions were the rate of change of the radiation was significant, so the granularity of this map was considered insufficient. A second interpolation was performed to improve the resolution. This used MATLAB's makima interpolation method [123], and created the final radiation dose map [124].

The result is a 5 cm resolution Cartesian coordinate dose map of the background radiation in the vault, shown in Fig. 42. The location of key objects in the vault can be discerned by looking at the peaks in the radiation map. The green lump on the right is the location of the cyclotron, where the backscatter from the protons has activated the cyclotron casing. The higher-radiation area on the left is towards the end of the beamlines. Some gaps in the beamline shielding were identified during the radiation measurements, which explain the much higher radiation levels in this area.

There is a danger of skewing the accuracy of the map by using multiple interpolation methods and extrapolating data in areas where there is no measurement. However, the radiation measurements are unchanged in the interpolation and were taken at intervals of 50 cm across the accessible regions. The map is most likely to diverge from reality in the inaccessible areas, where there were fewer data points for the algorithm to rely on - for example, the map at 3.8 m high is only accurate in proximity to the bridge. These areas are blocked from reach in the VR, to mirror the physical world inside the vault [124].

Breakdown of Radiation dose exposure μSv/h		
Point	Real World	in VR
Point 1	14 ± 1	13 ± 1
Point 2	87 ± 14	55 ± 1
Point 3	27 ± 7	35 ± 4
Point 4	60 ± 8	59 ± 4
Point 5	89 ± 8	86 ± 8
Point 6	13 ± 4	13 ± 1
Total exposure μSv	2.9 ± 0.3	2.6 ± 0.2

Table 5: Comparison of average radiation exposure between virtual and physical walkthroughs. The route was traced 3 times in both cases to provide statistical uncertainty (standard deviation).

5.3.3 Results

In order to compare the results of the VR radiation dose exposure prediction with physical measurements, a route through the vault was planned, shown in figure 43.

There were six easily identifiable points - in both the physical and virtual environments - inside the vault. Dose measurements were taken by a person following the route, standing at each point for 30 seconds. The instantaneous radiation levels were noted for each stage, and at the end of the route their integrated radiation dose was also noted. The virtual route was marked by the guidance points described in section 5.2. The guidance point timers were set to 30 seconds, allowing the user more time to concentrate on noting the radiation measurements.

The route was followed 3 times. The mean radiation dose measured in real-life inside the cyclotron vault was recorded as 2.9 ± 0.3 μSv. The same route was followed using the HTC Vive headset in the virtual environment. With the guidance points and dosimeter visible, the mean radiation dose was 2.6 ± 0.2 μSv. These integrated dose values are comparable and well within the accuracy of standard dosimeters (±20%).

A comparison between the real-world radiation exposure and the virtual estimate are shown in table 5. The table compares the instantaneous radiation dose measured at each point, as well as the total dose exposure at the end of each route.

The technician took the measurements around the vault 3 times, in both the real world and the virtual environment. This provides the statistical uncertainty provided in the table.

However, there are many factors at play that contribute to the uncertainties of this experiment: the large cell size of the data taking (0.5 m), the progressive deterioration of the grid measurement, the fluctuation of the radiation, and the extent of the interpolation, all contribute to the uncertainties with the map itself. There is also the alignment of the map within the virtual environment, and human error as the technician walked the route to consider. The accuracy of the result is reliant on the technician accurately recreating the

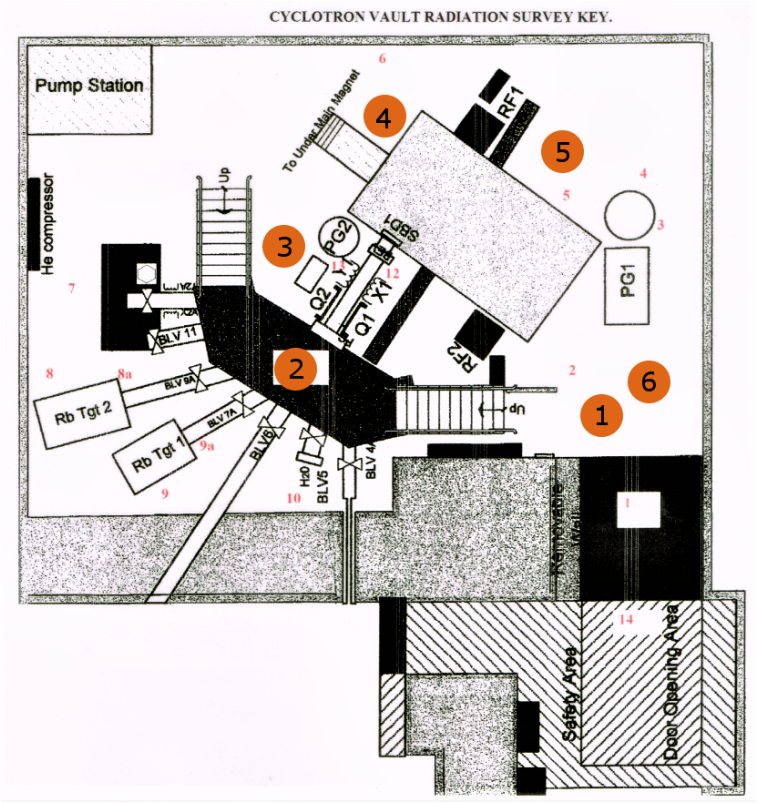

(a) Aerial view of the 6 points along the route overlaid onto the map of the vault

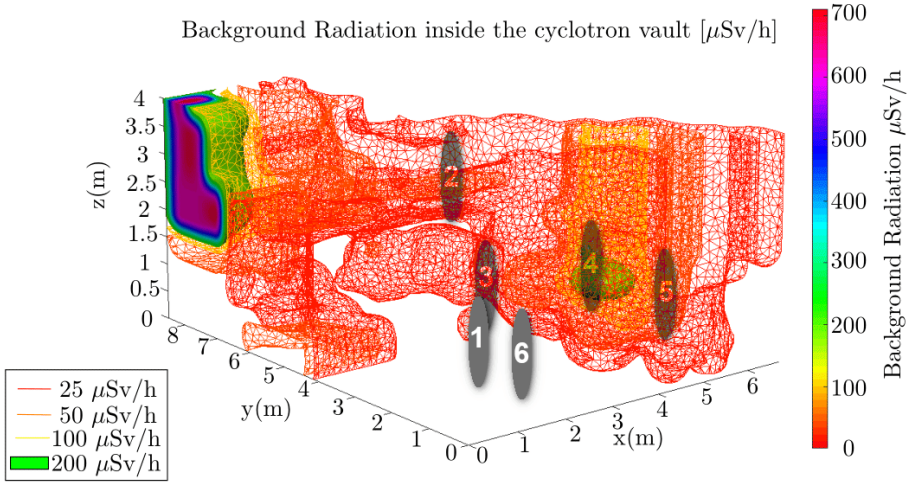

(b) The 6 points of the route around the vault overlaid onto the 3D radiation map.

Figure 43: Route around the vault. The technician recorded the instantaneous radiation dose over 30s before moving to the next point. The integrated radiation exposure was recorded after the 30s at point 6.

route taken through the vault multiple times, both in reality and in the virtual environment. There are certain aspects that VR couldn't recreate, such as the feedback of climbing the stairs to cross the bridge. Fig. 44 shows the gradient of the dose map. The largest gradients

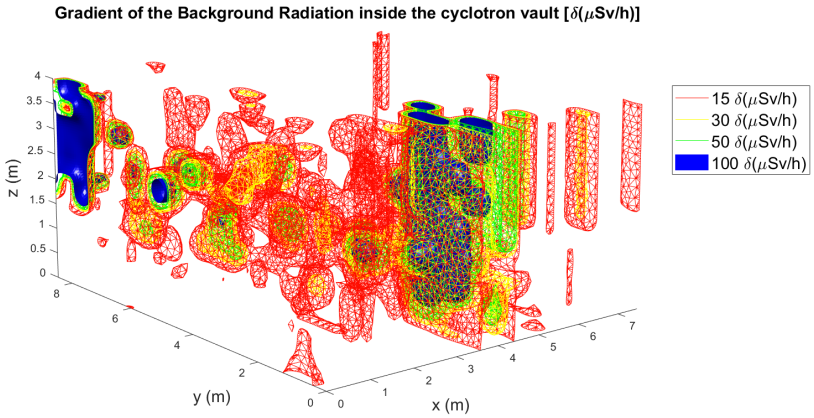

Figure 44: Gradient of the final radiation dose map

are close to the areas of high radiation - the cylcotron and the beamlines. However there is also a high gradient over the bridge. The 2nd point in table 5 shows a large uncertainty from the real world run-throughs, while the value for the VR run through has a large discrepancy with the real world value. The measurements on the bridge showed radiation levels of circa 40-50 μSv/h nearer to the cyclotron, however further away from the cyclotron the measured radiation rose to circa 80 μSv/h. This is shown on the gradient map, Fig. 44, as an volume of yellow and green mesh. The high gradient of the dose rate in the region shows that it is likely either the technician did not stand in the correct location due to human error or a misalignment with the dose map. It is also possible that the radiation data measurement across the bridge was insufficient to record the true peak of the radiation dose rate.

The background radiation fluctuated significantly inside the vault. It is likely that the radiation levels in the vault changed between when the measurements for the map were taken, and the vault walkthroughs were conducted. At Point 3 there were uncertainties as high as 27% between walkthrough measurements, which were conducted back-to-back. Fluctuations in radiation levels are not present in the VR platform, leading to lower uncertainties at individual points.

Despite this, the integrated radiation exposure values between the VR platform and the Real World are comparable. The main contribution to the uncertainty of the radiation estimate is the uncertainty of the radiation dose map and its alignment. With an accurate dose map and reliable location data, the platform will produce reliable results. The conclusion

drawn from the study determined that the accuracy of the virtual dosimeter depended on the accuracy of the dose maps, and the location data [124].

6 Using the Integrated System for Radiation Personnel Intervention Planning for the decommissioning of the ATLAS Inner Detector in combination with LED Motion Capture

Once the proof of concept was established (see chapter 5), the platform could be deployed to evaluate intervention scenarios. The first intervention where the platform was deployed was the decommissioning of the ATLAS Inner Detector, which will be replaced by the new ITk [13] (see chap 3.3.4). For this intervention scenario the platform was used to predict the expected radiation dose accumulated by the technicians during the ID decommissioning.

To improve the estimate of the accumulated radiation dose, a motion capture system was used to accurately track the technicians steps. This was necessary, as one of the weaknesses of pure virtual reality without haptic feedback is the ease of tasks. The user does not encounter the resistance of the screws while removing them, and does not need to exert force to pull wires out of their couching after they have been cut. To balance this, the use of motion capture was proposed.

Performing the motion capture (MoCap) data recording on the ATLAS detector itself would defeat the RP purpose of the work, so the ATLAS ID Mockup was used as an accurate substitute. A technician would go through the physical motions of decommissioning the Inner Detector on the Mockup, and the movements would be imported into the VR platform. This way the dose estimation could be performed with context, and the timing and location of the work would be accurate.

The MoCap simulation represents around three hours of decommissioning work within the cavern. The work simulated are the preparatory steps to remove the most radioactive components of the ID: The beampipe and Pixel removal. As see in Chapter 3.3.4, all their services (electrical, optical, cooling, etc.) must be removed before these components can be taken out of the detector. The steps of the services' removal are shown in Figs. 25 and 26 in chapter 3.3.4. The service removal requires the technicians to be in close proximity to the beampipe and Pixel, and so the work is considered the most concerning aspect of the decommissioning from a radiation exposure point of view. Once these are removed, the radiation background within the cavern drops significantly. However the whole ID decommissioning is planned over the course of a year, from preparation steps such as installing the scaffolding and removing the ID endplates, up to removing the last services inside the cryostat bore.

6.1 Experimental setup

This section will discuss the MoCap setup and collection of the raw motion data, then through the steps of processing the data to be imported into the VR Intervention Planning Platform.

The technician, Valery Akhnazarov, was involved with the Inner Detector installation originally. He was fitted with a set of MoCap LEDs (see section 6.1.1 for details) and performed crucial decommissioning tasks on the ATLAS ID Mockup while his location and position were recorded. Given the detector's symmetric design, certain steps will be repeated around the detector cylinder and on either side of the detector (sides A and C), such as the removal of the sub-detector services. Rather than record the same process multiple times, instead the technician performed the task once on a segment of the Mockup, and the final simulation multiplies the dose added to the dosimeter at the end of the required section of work.

Integrating the LED MoCap data into the VR Intervention Planning Platform was a multistage process. Fig. 45 shows the different stages of data gathering and processing from the Motion Capture setup at CERN, to the VR platform. The raw point data of the technician's movements were first processed to create skeletal movement data, then processed further to remove artefacts and ensure the movements of the final animated avatar were natural. This 'clean' data was then imported into the platform.

The platform calculated the radiation exposure while the animated avatar followed the technician's movements. It provided a integrated radiation dose estimation and identified 'problem points' where the technician incurred a sudden spike in radiation dose, or where the work required them to stand over a radiation hotspot. The platform also provided context for the technician's movements, as sections of the virtual detector were scripted to (dis)appear as necessary as the avatar worked.

6.1.1 Motion Capture Setup

A commercial MoCap system called PhaseSpace was used to record the technicians movements [125]. Its setup comprises of eight stereo cameras set up at varying heights in an approximate circle, and forty battery powered LEDs. The LEDs are grouped in sets of 8, and are not attached to a harness, as such the optimal method of LED attachment needed to be determined before the data recording could be undertaken. The LEDs pulse at individual frequencies, enabling the system to track each of them independently. Fig. 46 shows the positioning of LEDs on the wearer. This method of motion capture requires continued line-of-sight to the LEDs to track them accurately. An obstruction preventing line-of-sight (occlusion) between an LED and the cameras prevents the system from successfully calculating the LED's 3D location.

Due to time constraints, it would not be possible to refit the Mockup for multiple recordings. The data recording with the technician interacting with the Mockup could

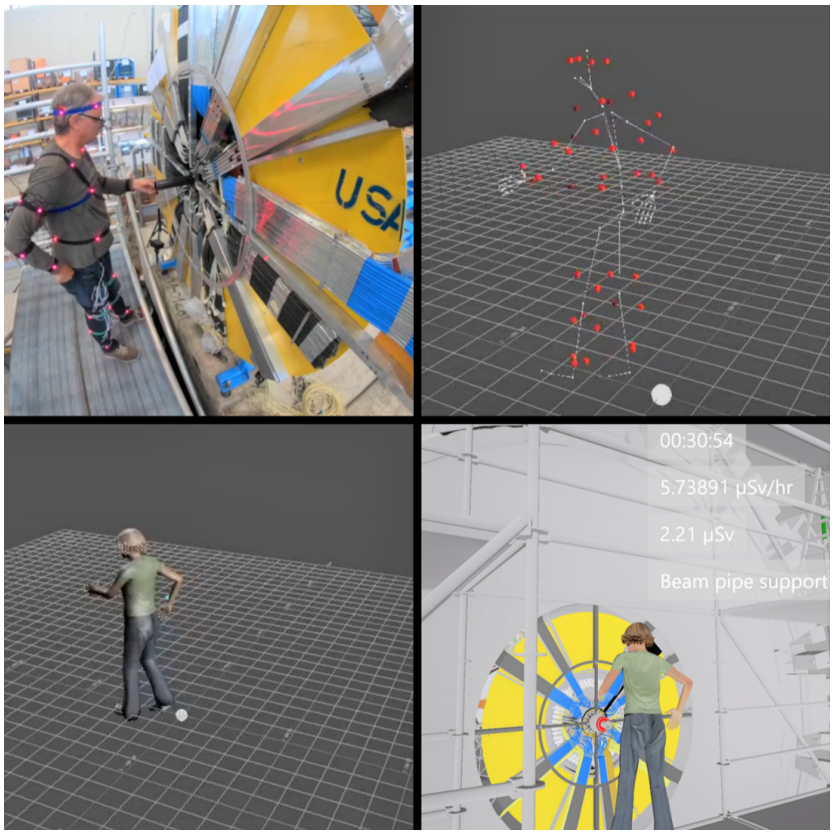

Figure 45: Top left: Technician performing decommissioning step with LEDs for motion capture; Top right: The MoCap data with Skeleton in PhaseSpace; Bottom left: The MoCap data with actor in MotionBuilder; Bottom right: The MoCap data in the Intervention Planning Platform.

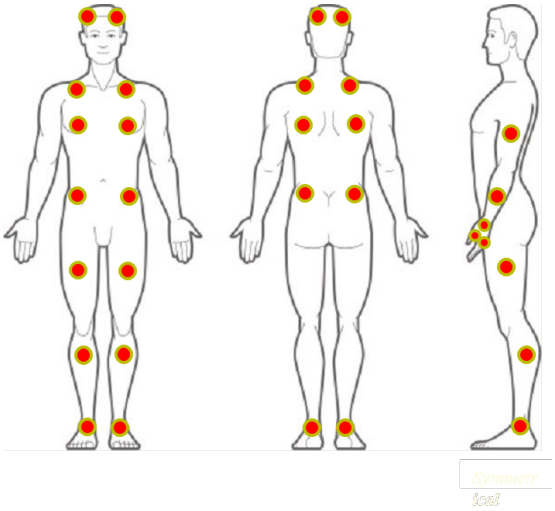

(a) The placement of LEDs on the body

(b) The author wearing the LEDs to calibrate the system and test for occlusions. Velcro strips were used to attach the LEDs to the body.

Figure 46: LED placement was determined through trial-and-error to determine the best setup with the least obtrusive occlusions.

only be conducted once. It was therefore crucial that potential problems with the recording be identified beforehand, and solutions found, to ensure the final recording was successful. Several iterations of the motion capture set up were trialled to determine the optimum LED configuration, as well as learn the best techniques for data processing and refinement (which will be explored further in Chapter 6.1.2).

The first attempts at attaching the LEDs to the MoCap test subject included using adhesive tapes on clothing, however this proved to be a fragile setup. The adhesive required constant monitoring for degradation, and fixing LEDs which came loose. This often interrupted the motion capture data taking. The clothing was baggy as it was intended to be worn by multiple people. Overall this setup did not give reliable results as the LEDs could move independent to the wearer, causing problems in the data-processing algorithms. It was also uncomfortable to wear, which could affect the technician's movements during the data taking. To begin with, only 4x8 LEDs were used, however this provided insufficient coverage of the body, as multiple LEDs were required at different orientations on the same body-part or joint to prevent issues caused by occlusions. Initially the LED wires were not long enough to cover limb lengths and needed to be extended. In order to resolve the issues with the LED placement, the LEDs were sewn onto velcro squares, and velcro strips were cut to create strips for them to attach onto. The strips could be used to create an adjustable harness, and could be fastened at strategic points on the body, such as around the wrist, head, leg, torso, shoulders. The velcro squares with the LEDs could then be attached in the locations

desired. Using LEDs sewn to velcro had several advantages: it was more secure and unlike the adhesive tape it didn't require constant maintenance; it kept the LEDs skin-tight, whereas LEDs attached to baggy clothing gave sub-optimal results after data processing; it gave the setup flexibility and could easily be adjusted for different wearers instead of a one-size-fits-all approach; it simplified the trial of different LED positions to find the best configuration of LED placements; and it was easy to wear. The velcro proved to be a much more successful as an adjustable, reusable and secure method to creating a motion capture harness [126].

The ATLAS ID Mockup features scaffolding around the ID Endplate to accurately portray the technician's work area. The MoCap camera had to be set up outside this scaffolding, meaning the target area had numerous obstructions to the cameras. In addition, some of the technician's tasks required reaching inside the Mockup to remove the services - which sometimes blocked line-of-sight to the LEDs on the wrists. Trial and error determined the optimal setup of the cameras and LEDs for the best coverage, however occlusions could not be totally avoided. This was not ideal for MoCap data collection, however through further processing, extrapolation of the LED locations was possible.

The best configuration was determined to be forty LEDs arranged as follows:

- 4 LEDs around the head
- 2 on each shoulder (one front and back)
- 2 on each upper arm
- 1 on each lower arm
- 2 on each wrist
- 4 on the upper torso (two front, two back)
- 4 LEDs around the hips
- 2 on each upper leg
- 2 on each lower leg
- 3 around each ankle

The wires and drivers were tucked into the LED harness to avoid the wires pulling or trailing during the recording.

Fig. 47 shows the position of the stereo cameras. The PhaseSpace software calculates their whereabouts in space from an initial calibration using LEDs embedded in a baton. The yellow pyramids show the cameras field of vision.

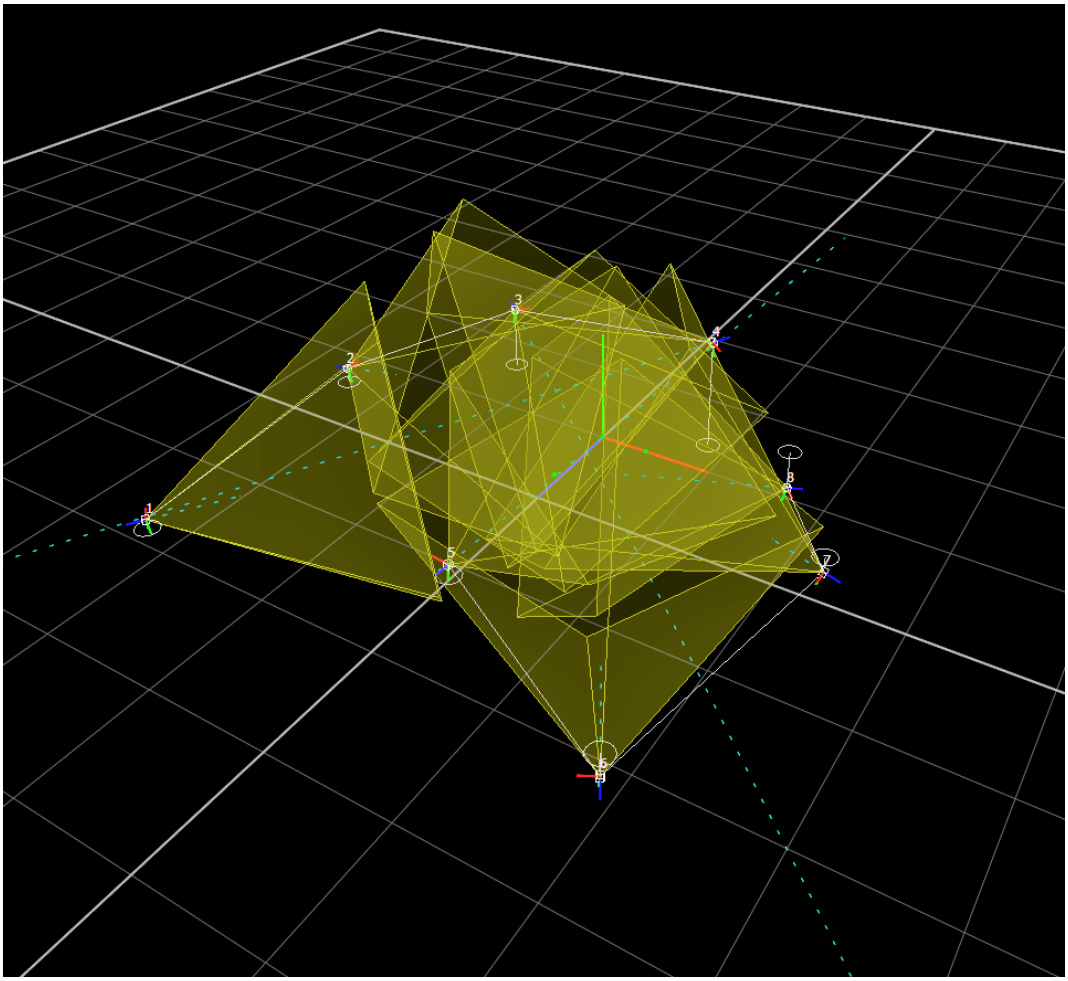

Figure 47: The position of the stereo cameras shown in PhaseSpace software

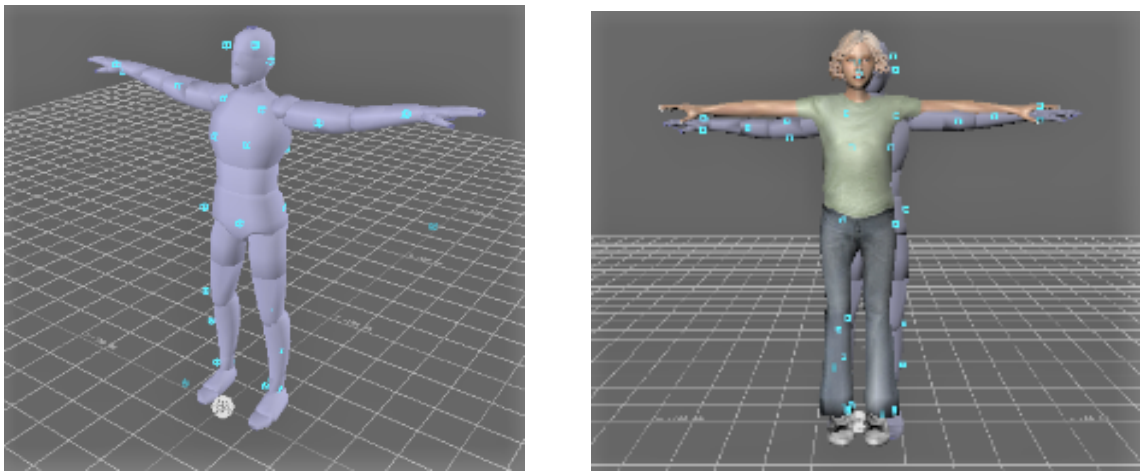

(a) The "actor" is aligned with the MoCap points in Autodesk MotionBuilder

(b) The "character skin" is added to the actor in Autodesk MotionBuilder

Figure 48: Autodesk MotionBuilder was used to process the data, moving from an animated skeleton to a character

6.1.2 Motion Capture Data Processing

After the motions were recorded by the cameras, the data was then processed using PhaseSpace's associated software Recap2 [125]. This transformed the initial disassociated individual moving points to the recognisable structure of a human skeleton. Attempts to use MoCap algorithms with only the upper-torso and arms were unsuccessful, as motion capture algorithms tuned to the human body expect to be able to construct a human skeleton (head, two arms, two legs, and a torso) from the disassociated points. Without the full skeleton, the algorithm had difficulty orientating the base of the spine - the section which determines the avatar's location within the virtual environment, see Chapter 4.1.2. The skeleton and 3d point data was then imported and further processed in Autodesk MotionBuilder [127].

Occlusions obstruct the camera's view of the LEDs, which causes the system to lose their point in space. While the software is aware that the LED is not visible, it creates an approximate location based on the previous point seen and its motion prior to losing the LED's position. The longer an LED is occluded, the more its location data deteriorates, which can lead to many unpredictable un-physical effects to the skeleton's movements which have to be 'cleaned' from the raw data.

The MotionBuilder interface shows the gaps in the motion capture timeline between the recorded position and the occluded points where the location is approximate. The occluded points can be cleaned individually, by creating interpolations between the gaps in the LED positions. However this is very time consuming as individual LEDs must be cleaned one at a time. MotionBuilder has an algorithm to auto-interpolate the missing location data using

'rigid bodies'. Rigid bodies work by grouping LEDs together and imposing that they do not move relative to one another. Rigid bodies are useful in the case of an occlusion, as the system is able to extrapolate where the missing LED is located, despite not being able to detect it directly. Rigid bodies were most effective when defining a cross section of the body, for example: grouping the four hip LEDs, or the four head LEDs together. As these are defined by the size of the cranium and the pelvis, it can be assumed these LEDs won't move relative to each other. Rigid bodies used for this work included the head, chest, hips and clavicles [128]. Defining a rigid body over the front chest area was less effective, as the LEDs would move relative to one another when the technician crouched or stretched. This contradicts the principles of a rigid body, and the extrapolation of the missing LED's position was less successful.

Next, an actor and a character skin were added to the MoCap data. The actor adds bulk to the skeleton using body segments. These are mapped to the relevant LEDs, and will rotate with these LEDs and the skeleton as they move over time. A character skin was then applied on top. The character skin is not only cosmetic, it also ensures the actor segments do not detach from the skeleton. This was liable to occur if a significant joint LED was occluded, such as the shoulder. Fig. 48 shows the actor and character skin being added.

Not all LEDs are given equal weighting by the MoCap data processing algorithms. Some have greater influence on the avatar's pose and position than others. For example, an occluded foot LED could be decisive in establishing the avatar's location, despite contradicting information from all the other LEDs. Although the previous steps were successful in addressing most of the issues, problems such as these were identified by a technician examining the output avatar's movements for anomalies. Once found, the issues were then corrected in MotionBuilder by modifying MotionBuilder's interpolation between the times when the LED data was accurately identified. Human judgement on smooth and natural movement was used determine the best fit on a case-by-case basis. This step, and determining the parameters of the previous data-cleaning processes are subjective to the notion of 'natural movement', and required introducing a 'best-estimate' of the occluded LED's position for the algorithms to reassess. Long duration occlusions were rare, and were more likely in the extremities such as the hand and feet. Cues on the correct LED positions could be taken from the position of the actor, and the spatial locations of the unoccluded LED points. As this work relies on the torso location for dose estimation, errors that affected the actor's 3D positioning were prioritised.

6.1.3 Virtual Reality implementation

Once the optimal MoCap setup was established, sequences of the ID decommissioning were recorded with the technician working on the Mockup. After the data was processed it could

then be imported into the VR platform.

Initially the import was attempted using BVH. BVH is an ascii file which details the structure of the (humanoid) skeleton, then each channel's relative position and 3D angles, for each frame of the motion capture data [129]. It was expected that using a custom lua script to import a BVH file would be a faster and more flexible as the animation would be created directly from the BVH timing, positioning and rotation data. However, Virtalis Visionary Render only permits user scripts to specify Euler angles of objects, despite the platform using quaternions by default (see chapter 4.1.3). While BVH files also use Euler angles and specify the order in which they should be applied, the angles could not be successfully recreated. Due to timing constraints, the BVH method was abandoned in favour of using the proprietary filmbox (.FBX) format, which required an additional license [126].

There is a limit to the animation length of the MotionBuilder FBX export, so the data was transferred in small segments in multiple FBX files. Each FBX segment included its own avatar linked to the segment of MoCap animation, as well as the animation of all the motion capture LED points. All this extra data caused Visionary Render to slow down to the point where it was almost inoperable. Steps to reduce the bloat needed to be taken to keep the platform usable. This included removing the LED points and their animations as these were no longer needed, and mapping each new MoCap animation imported from the FBX files onto the 'original' avatar, before deleting the (now superfluous) copies. Animations can be run individually, combined together or run in parallel in Visionary Render. For simplicity, the MoCap animation segments were first grouped by decommissioning step, then the steps were added to an overall decommissioning animation sequence. The start and end times of each MoCap segment, and of their parent animation sequence, had to be aligned carefully to avoid overlaps. Lua scripts can also be added to an animation. These animation scripts can be inserted at any time-point of the animation, and the timing is specified by the user - it is defined as the time in seconds from the beginning of the sequence. The scripts then run when the animation reaches that point in the playthrough. This added script functionality permitted interim dose measurements to be taken at strategic points of the simulation, as well as allowing the multiplication of the dose exposure for specific decommissioning steps, when only a quarter-section (for example) had been recorded in motion capture. Contextual effects were added as well, such as removing sections of the detector as the decommissioning was simulated. This further allowed the worker's movements to be put in context within the virtual environment, by making the environment respond to the simulated actions and illustrate how the decommissioning steps are progressing within the simulation. The platform also dynamically changes the radiation dose map when the simulation has removed a section of radioactive material.

In the VR platform, the virtual environment has one or more associated dose map(s) which the system uses to calculate the instantaneous radiation exposure, and the running

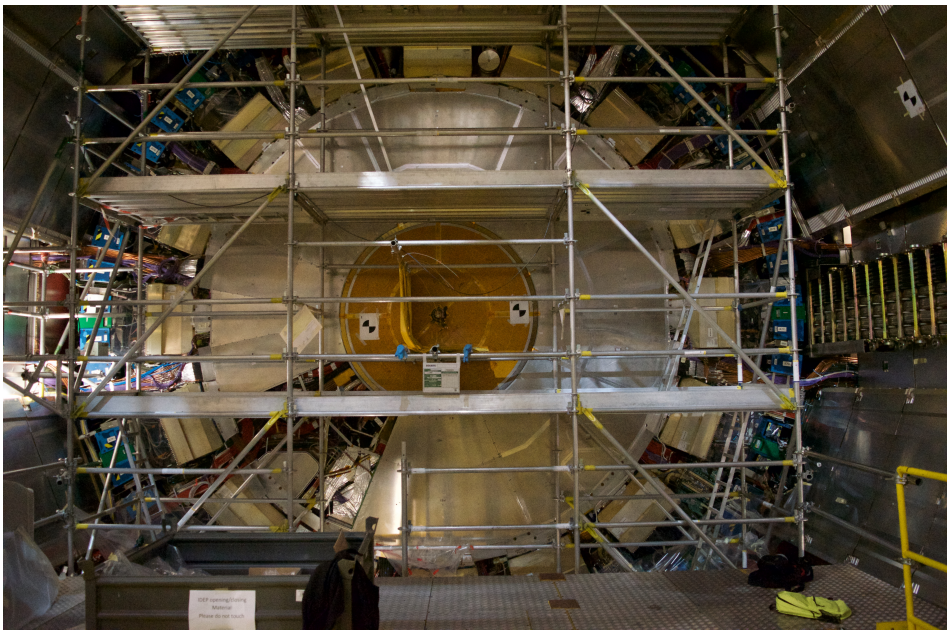

(a) The scaffolding around the ATLAS ID Endplate

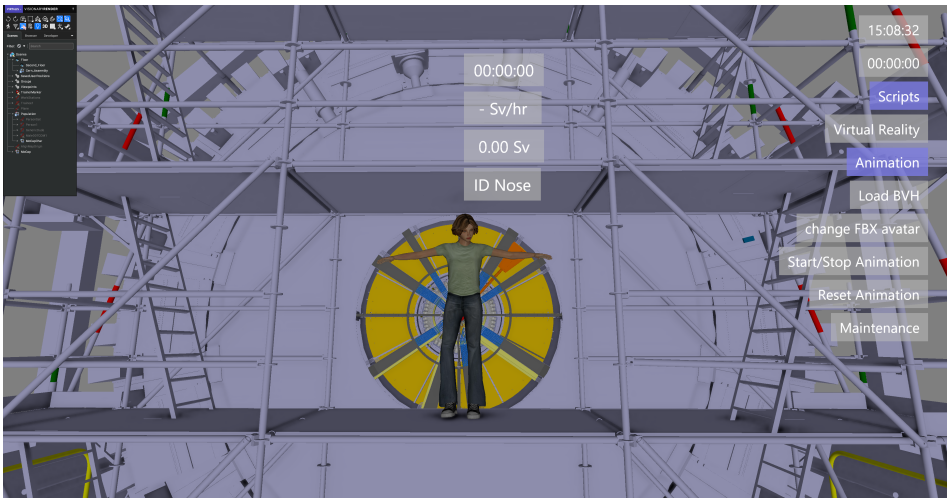

(b) A technician on the scaffolding and ATLAS Endplate in the VR Intervention Planning Platform

Figure 49: The ATLAS detector and its Virtual copy inside the Intervention Planning Platform. The T-pose is the standard starting pose for MoCap data recording

total of the accumulated radiation dose. The radiation dose maps used for the ATLAS ID decommissioning estimate were provided by CERN's radiation protection team [130]. Two maps were used. The first was after 181 days cooldown, and had the ATLAS geometry intact, shown in Fig. 50a. It shows the highest radiation areas nearest to the beamline. The Inner detector is in the lower left-corner. The gradient of the radiation map is shown in Fig. 50b. A zoomed-in version of the dose map with the ID geometry overlaid can be seen in 51. The second was again at 181 days cooldown, however the beampipe has been removed. As mentioned in chapter 3.3.3, the simulations to create the maps are lengthy, and therefore the background radiation maps were only created for significant phases of the decommissioning process, where a significant change in the background radiation is anticipated.

Fig. 49 shows the scaffolding around the ATLAS Endplate, and its the virtual copy inside the Intervention Planning Platform. The avatar's dosimetry information is shown in Fig 49(b) above the technician's avatar's head including the timer for the work, instantaneous radiation exposure rate, accumulated dose, and the work section currently being simulated. The dosimetry scripts use the chest location as the position for the dose rate. The animation and dosimetry scripts are activated using the Start/Stop animation button, shown on in the HUD GUI on the right of Fig 49(b). There is also a script at the end of the animation that deactivates the dosimetry. Otherwise, the dosimetry scripts run independent of the animation and functions identically for the animated avatar as for a user with a headset, periodically looking up the instantaneous radiation dose for a specified position - in this case the avatar's chest - integrating it with respect to the time lapsed, and adding the result to the aggregate integrated dose. The T-pose is the default start pose for motion capture algorithms, and each new motion capture required the T-pose at the start.

6.2 Results and Discussion

A breakdown of the simulation results is given in table 6. The decommissioning steps performed would take 3 hours 7 min and the technician would accrue 14.75 μSv $\pm$ 13%. Due to a binning error in the previous work [126], the values presented here cannot be directly compared.

For this thesis, a deeper investigation was required to understand how small variations in positioning, or a map misalignment could influence the dose estimation. More simulations were run, with variation on the origin of the radiation map. There was one central run conducted (where the origin did not change), then $\pm$ 0.1 m in x,y,z axis[v], giving a 20 cm displacement variation on the map positioning. A 20 cm displacement is not large, however the work area of the scaffold is approximately 2 m by 1 m and the technician's movements are limited by the location of decommissioning tasks. It is therefore reasonable to assume there

[v] excepting (-0.1,+0.1,+0.1) which was missed

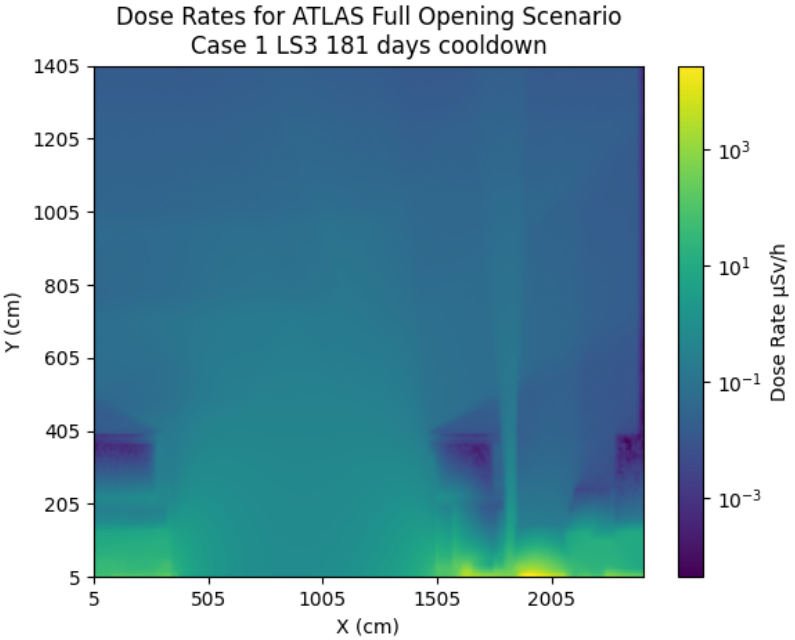

(a) Dose map for case 1 (full geometry) of the ATLAS Full opening scenario, after 181 days cooldown

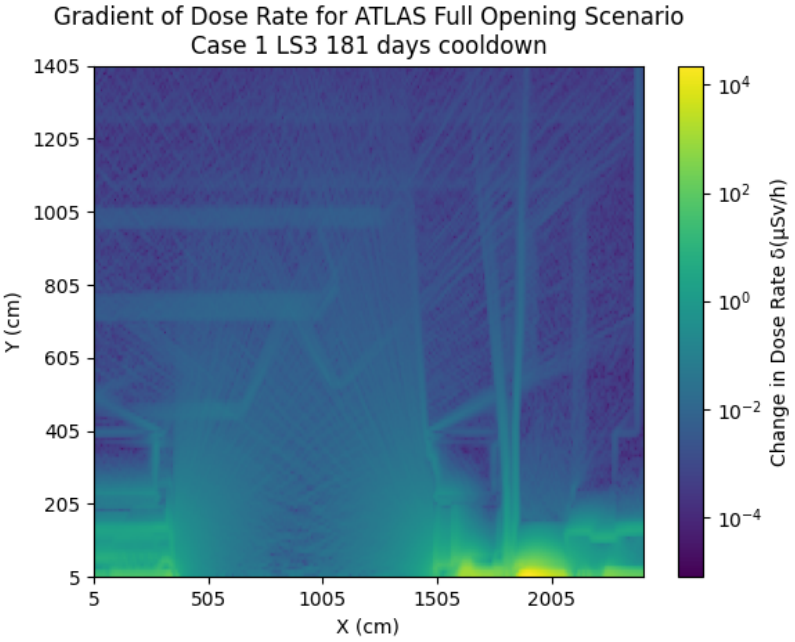

(b) The gradient of the first dose map for case 1 (full geometry) of the ATLAS Full opening scenario, after 181 days cooldown. Echoes of the ATLAS geometry can be seen in the gradient change.

Figure 50: The first dose map used in the Motion Capture Scenario dose estimation simulation

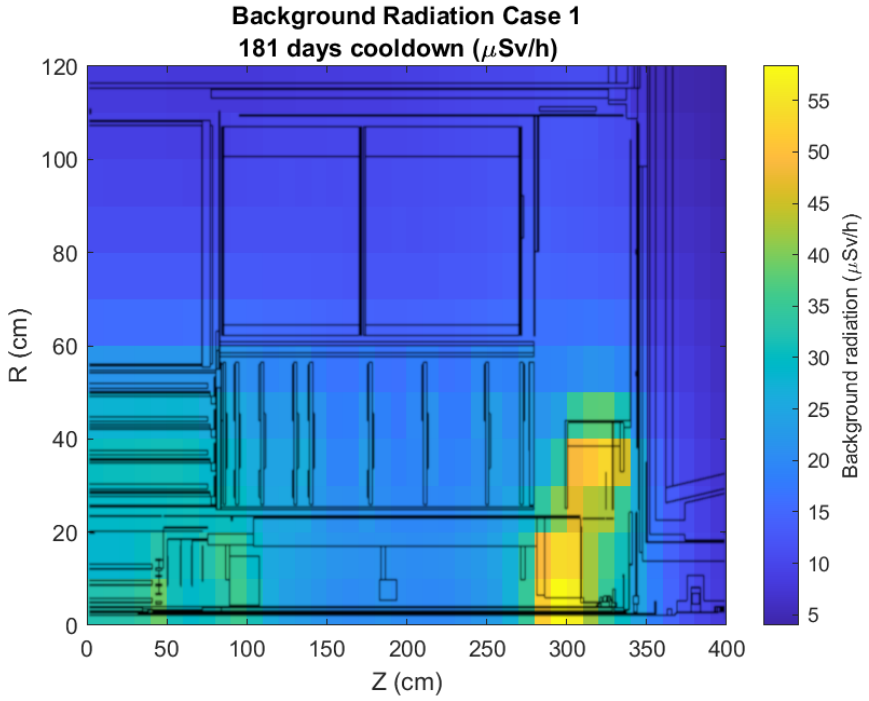

Figure 51: Close up of Figure 50a, with the ATLAS ID geometry superimposed

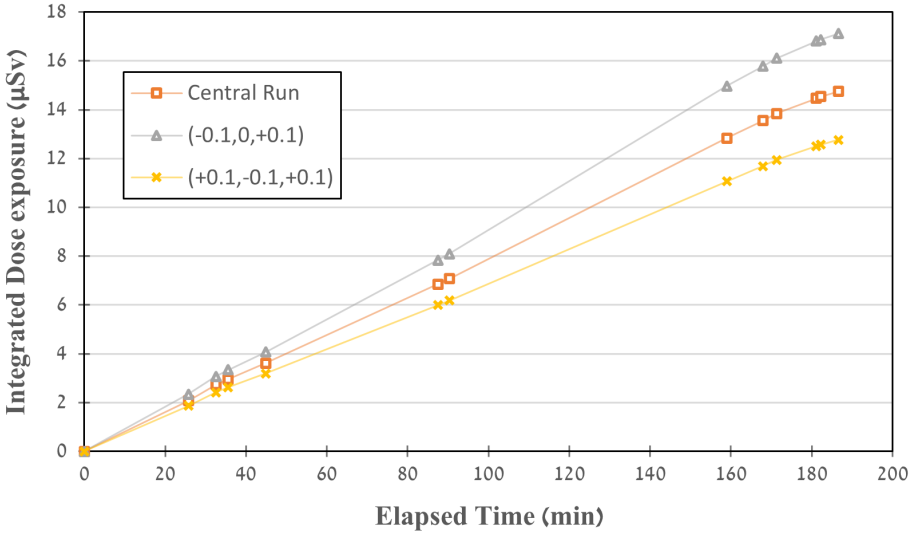

Figure 52: Integrated Radiation exposure by elapsed time in minutes. For legibility, only 3 simulation runs are shown. The central run was at (0,0,0) map alignment, the simulations with the lowest and highest exposure has a map alignment of (+0.1,-0.1,+0.1) and (-0.1,0,+0.1) respectively.

would only be small variations the technician's positioning.

The graph in Figure 52 shows how the variation in the map alignment affects the integrated dose estimate for specific runs. The dose estimate varies between 12.77 μSv and 17.12 μSv, an envelope of 4.35 μSv, $\approx 25\%$. This gives the central run value of 14.75 μSv an approximate uncertainty of $\pm 13\%$. The variations in radiation exposure appear from the beginning, and the divergence steadily increases over time. The Variation in slope for the longer sections of work have the biggest impact on the

The radiation restrictions for occupational exposure for both France and Switzerland is 20 mSv/year [37] (see chap 2.4.3). CERN itself aims for worker exposure below 3 mSv/year [131], which is approximately an individual's annual background exposure. The steps recorded in the motion capture are expected to have the largest radiation exposure of the Inner Detector decommissioning, however the estimated exposure during the work is 200 times lower than CERN's RP target, and an order of magnitude below the legal limit of annual radiation exposure - these estimations are low enough that human intervention for the ID decommissioning is still acceptable.

Valery Akhnazarov carried out the decommissioning steps for the motion capture, shown in the top left of Fig. 45. He was familiar with the expected decommissioning tasks as he was involved with the original ID installation, and is anticipated to carry out the real ID decommissioning during the LS3 shutdown. During the real decommissioning, he will be wearing the appropriate Personal Protective Equipment (PPE) as expected for ATLAS work. These will be an operational dosimeter, helmet, and safety shoes. A self-rescue mask will be provided and available nearby, but not worn. However in this work concessions were made for the MoCap data processing algorithms, which returned the best results when the LEDs had body contact. The effect of the extra PPE on the technician's movements is considered negligible [126].

The data recording was undertaken just once due to time constraints, but can be repeated when needed. While the training aspect of the platform was not utilised in this work, the estimation provides a baseline for radiation exposure for an experienced technician familiar with the required tasks. This baseline can be used as a reference for training.

By analysing the data collected in this work, it is now possible to minimise the received dose by adjusting the location and posture of the technician. It was noted that during the motion capture, the technician spent a significant amount of time with his chest or head directly in front of the beam pipe, which is the most radioactive section of the detector. He worked with no direct knowledge of the background radiation levels or the dose accumulation. He also had no restrictions on where he stood on the scaffold as he worked. It is possible that knowledge of the radiation area and dose accumulation could have affected where he decided to stand, and his subsequent approach to the different decommissioning tasks. However, the estimation of the amount of time it would take for the Pixel removal was revised down

due to the practise decommissioning for the MoCap being much faster than anticipated. Changing the technician's posture and positioning could result in increasing the duration of the decommissioning and potentially increasing the integrate radiation dose.

A lead lined vest such as those worn by X-ray hospital staff was briefly considered to mitigate the higher radiation exposure, however it was decided that this would be counter-productive, as its weight would slow operations whilst not altering the exposure risk, as lead is ineffective to the type of radiation in question. The effectiveness of different shielding concepts can be analysed by updating the radiation maps and directly comparing the corresponding estimated doses. This will become more significant for future HL-LHC shutdowns where the is expected to be significantly higher background radiation [126].

Objective	**Steps**	**Duration** hh:mm:ss	**Dose Estimate** μSv
Remove IDEP	Remove inner IDEP Nose	25:44	2.08
	Remove outer IDEP Nose		
Clear BeamPipe/IBL support structures	Remove rad monitor quarter circles, BP support beams, and BP sliding ring	6:49	0.65
	Remove outer quarter ring	3:02	0.23
Clear IBL and pixel services	Cut IBL services and Remove IBL service guide	9:18	0.65
	Remove heater trays and tubing	42:36	3.24
	Cut ER bundle	2:48	0.22
	Cutting internal Pixel services	1:08:40	5.76
Prepare Pixel for extraction	Remove PST seal plate	8:56	0.72
	Install PST rail interface	3:23	0.29
	Install pixel support ring	9:51	0.63
	Install internal transition rails	1:07	0.06
	Install intermediate rail and frogs	4:20	0.22
	Total	3:06:47	14.75

Table 6: Results of the Motion Capture dose estimation. The result is 14.75 μSv $\pm$ 13%. Due to a binning error in the previous work, the value presented here cannot be directly compared with those from [126].

6.3 Future development planned for the system

VR removes many of the constraints around the exploration of harsh environments by providing an accurate facsimile of the situation without the associated risk. Further investigation of this technology will be crucial to future time and location sensitive projects [124].

Trivial actions such as (un)bolting, cutting, and moving objects take time that VR does not currently realistically reproduce. While motion capture does provide a counter to a purely virtual setup, it was a lengthy process to record the data and import it into the system. This was partly due to the numerous occlusions caused by the scaffolding, but also due to Visionary Render slowing down as the FBX imports bloated the VR platform. A more streamlined approach to data processing, and a target area free of obstacles could help in the first case, however the FBX filesize to be imported was proportional to the length of MoCap animation. It would be feasible to use multiple instances of the VR platform to import the MoCap data, however this would preclude the convenience of having one radiation dose estimate completed

in one instance of the software.

It is important to recognise the limits of the platform. The radiation prediction becomes less reliable as the environment geometry changes. The radiation dose maps are static external files. These are pre-loaded into the scene on opening, and can be changed by script triggers such as the movement of a specific object, or a time lapse. While this saves computational resources, the radiation dose maps were constructed with strict parameters and any unplanned or transitory change in geometry could expose, move or cover a radiation source.

Unfortunately, it is not feasible for the ATLAS experiment to simulate every permutation of geometry movement during the ID decommissioning. The extraction of the Pixel tracker is estimated to take circa 8 hours. A proposed addition is the development of dynamic dose maps, which would allow for a gradual movement of parts of the detector instead of an instantaneous removal by switching between static dose maps as implemented currently. This would make the platform more flexible in its possible applications.

The virtual environment used in the platform is a static representation, influenced only by users within the setup. An animation may move objects around, but this is predefined movement and inorganic. Digital Twins is a concept where a robot or any other dynamic object is rendered in VR, and linked so the two physically and virtually mirror each other, no matter which one is programmed to move. This is accomplished by enabling the physical robot to broadcast its joints' position through a TCP/IP server, which the platform would receive and apply to the virtual copy. The VR copy would also act as a controller for the physical robot, and any changes made by the VR user to the VR robot's position or motions would be transmitted to the physical robot through the same TCP/IP connection.

The platform was designed to help reduce human exposure to radiation, the introduction of a robot would be a logical progression. The virtual environment would still enable exploration of the harsh environment and invention planning. It would also provide an extra point of view to oversee the robot's execution - beyond camera and sensor feedback. Similarly to the implementation of motion capture for dose estimation, observing the digital twin in the virtual environment would provide context to the robot's actions, especially if the Digital Twin can interact with the virtual environment in the same way as a user. Adding to this, once the radiation tolerance of the robotic components is known, malfunctions or mechanical failures can be anticipated and the repairs planned - including ordering spare components in advance, which reduces down time.

7 Characterising lifetime radiation exposure of a CMOS Camera and robot manipulator for extreme environment applications

This chapter will cover the characterisation of radiation tolerance for specific robotic components, with the view to creating a baseline for use in future digital twin applications of the VR platform.

While robots are more resilient to radiation damage than biological systems, their electronics still degrade when subjected to high and/or long term radiation exposure. Anticipating the necessary radiation tolerance needed for new detector components is very important. Simulating radiation damage to the detector, and testing the sensors response will determine firstly how the damage affects their output, and if their lifetime durability is suitable for use in the HL-LHC.

At the HL-LHC and in other highly irradiated environments, silicon chips are used in readout and sensor electronics. Radiation hard Complementary Metal Oxide Semiconductors (CMOS) have been tested for the HL-LHC by the RD48 and the RD53 Collaborations, for example in Ref [132]. Primarily these studies evaluate sensor chips to be used in the new ITk, for example: a higher luminosity inside the beam will cause higher radiation levels in the detectors. The target hardness for new electronics is 10^7 Gy total accumulated dose (inclusive of a safety factor of 1.5) [89], [133]. It is therefore crucial to study the response of proposed replacement CMOS chips before and after high radiation exposure [134].

There is also a requirement to design and evaluate robotic systems for future detector interventions or decommissioning, as the simulated radiation levels would severely restrict human intervention. Developing radiation tolerant or radiation hardened electronics has applications in several different areas, the most notable are space science, medical physics and high energy physics. Robotic grasping systems and end effectors are an important element of any robot required to interact with its environment with precision [135]. As the ATLAS detector was designed to be maintained and decommissioned by humans, there is no framework installed within the ATLAS detector to aide robotic interventions. Any robots working on the detector would need to operate with human-like dexterity and strength to accomplish the work while also ensuring they do not damage the detector. Such damage could occur by dropping a loose screw as it is unfastened, or exerting too much force on the components as they are removed. The operators of these robotic systems will also require visual feedback to inspect the ID and manoeuvre the robot and its manipulators effectively. Camera sensors will therefore also need evaluating to assess their suitability to high radiation environments. In the following, radiation tolerance of a robotic manipulator and a commercial CMOS camera were tested for their general suitability in high-radiation environments. The specific choice

of device was driven by a collaboration with industrial partners, i3D robotics [136] and the Shadow Robot Company [137].

7.1 Using the Birmingham Cyclotron proton beam to benchmark radiation tolerance

The HEP area of the Birmingham cyclotron facility, introduced in Section 5.3, is mainly used to irradiate silicon sensors for the HL-LHC upgrade. It was chosen for this irradiation due to previous collaboration work, and ease of access to the facility as the ESIM group [116] would also be supplying an upgraded radiation box prior to the benchmark test. The instrumental setup comprises of a chilled radiation box on top of a XY-axis Cartesian robotic system, shown in Fig. 53. The robot has two motors at 90 degrees that move the box in a plane normal to the beam. One motor moves the box horizontally across the radiation window, and the other moves it vertically. The box is moved through the beam at constant velocity in a raster pattern. The horizontal rows are offset by half the beam width to ensure that the samples inside are irradiated homogeneously to a pre-set dose [117].

The proton beam area is 1 cm^2 considered homogeneous [118]. To ensure a uniform distribution of radiation, deeper samples must be irradiated multiple times in different orientations [117]. The beam trajectory is serpentine, making long horizontal passes and vertically moving when outside the sample. Due to possible irregularities in the beam, the vertical displacement is only half the beam width - this means with each full profile scan of the sample, the proton beam will have passed twice over each point of the sample. The beam is considered to have a penetration depth of 7.8 mm. 28 MeV protons through liquid water have a range of 0.78 cm cm^2/g (value taken from the NIST PSTAR database [138]). As the density of water is approx 1 g/cm^3, the penetration depth of 28 MeV protons through liquid water is therefore 7.8 mm.

The beam transfers a large amount of energy into the samples over a relatively small area which can cause thermal damage to the surface. Annealing, where the silicon lattice in a sensor attempts to knit itself back together, increases with temperature and modifies the immediate damage from the radiation beam (see chap 2). To mitigate these effects and improve the sample analysis, the box's temperature is maintained at -27°C throughout the irradiation using either a HAAKE Kryo-Thermat 140 Glycol chiller or a Norhof Liquid Nitrogen dewer and pump.

7.1.1 Experimental Setup

7.1.1.1 Setup for the camera

The first irradiation target was an ImagingSource camera provided by our industrial partner, i3D robotics [136]. It is $29 \times 29 \times 57$ mm^3 in size, with 0.8 mm thick aluminium casing, and

(a) Photo of the Cartesian robot system with radiation box.

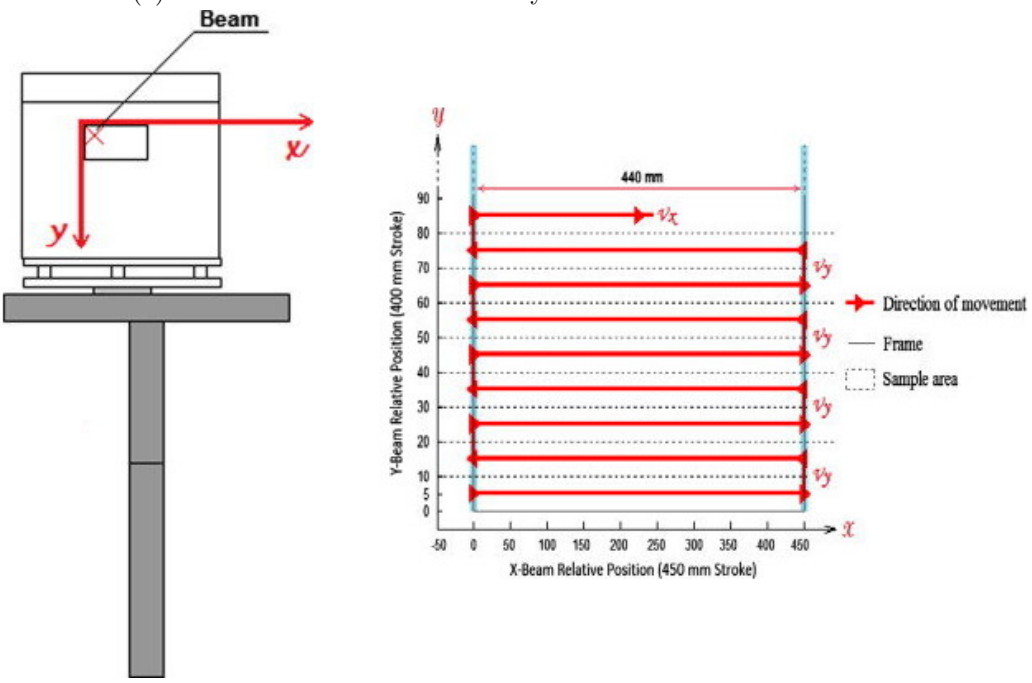

(b) Diagram of the Cartesian robot system. The origin of the axes for both the cartesian robot and the irradiation scanning is the top left hand corner of the irradiation window. The horizontal rows are offset by half the beam width causing an overlap, meaning each section of the target crosses through the beam twice. This is to mitigate beam inconsistencies.

Figure 53: Depositing an even dose across a surface area larger than the beam profile requires a scanning the beam over the target. This is achieved by moving the target box in a raster pattern, taken from [117].

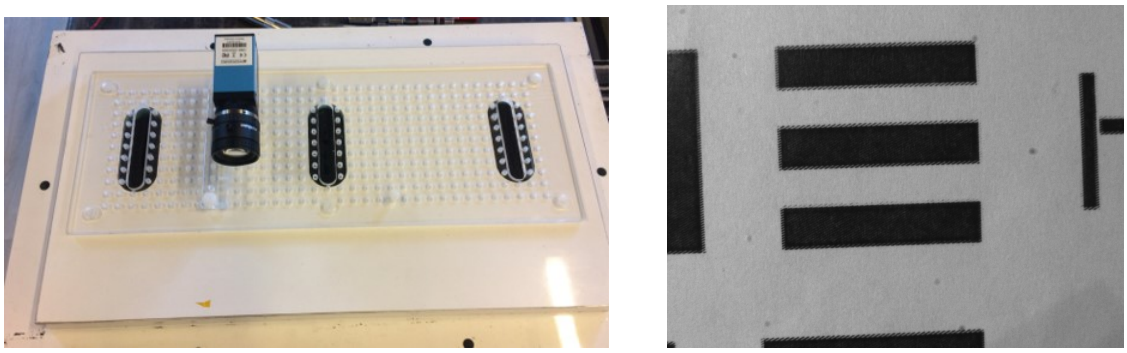

(a) (b)

Figure 54: a) Camera secured to the box lid. b) Pre-irradiation photo of the target taken by the camera.

uses a single Ethernet cable for both power and data. The camera was mounted to the lid of the box (shown in Fig. 54a) and pointed towards a two-tone geometric target (Fig. 54b). The camera irradiation was setup to conducted 3 profile scans, lasting 5 min58 s each. During the irradiation, the camera sent one photo per second to the computer. This was to monitor pixel degradation, and also gave a timing estimate for when the camera failed, allowing an accurate estimate of the total dose received.

The Cartesian robot was programmed to move the box through the proton beam in its raster scanning motion across the camera profile, as it is larger than the 1 cm^2 beam area. To avoid thermal damage, a radiator controlled by a HAAKE Kryo-Thermat 140 glycol chiller [139] (shown in Fig. 55b) kept the inside of the box at 10°C ± 0.2°C. The radiation is fixed in the bottom of the box, so the cooling of the camera was ambient instead of directed. LN2 cooling was not used for this experiment, as there were concerns the nitrogen vapour would appear as artefacts in the camera's photos.

The target total irradiated dose was initially 300 Gy, with the expectation to increase to 600 Gy, or until the camera broke. Initially the Cartesian robot would be programmed to scan over the camera and the beam to deposit 300 Gy (total dose). Successive repeat scans would be performed until the camera failed.

In order to determine how long the camera would need to be in the beam, the stopping power of the camera was calculated. The approximate stopping power of a compound material is calculated by summing the stopping power of the component materials multiplied by their fractional weight, as expressed below [140]:

$$\Big(-\frac{dE}{d\chi}\Big)_{comp} = \sum_i w_i \Big(-\frac{dE}{d\chi_i}\Big)_i \tag{8}$$

where $dE/d\chi$ is the stopping power of the compound material, w_i is the fractional weight of

the component material, and $dE/d\chi_i$, the stopping power of the component material. The inner of the camera, shown in Fig. 55a, can be considered a solid volume of circuit board material which is a fibre glass composite. Using the NIST database [138] and equation 8, the stopping power of the camera is 16.11 MeV cm^2/g.

The irradiation was setup to take 3 scans lasting 5 min58 s each, with the proton beam of 28 MeV protons at 10 nA[vi].

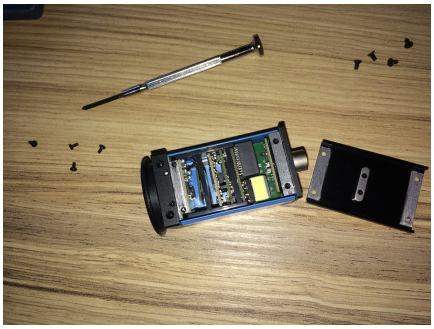

(a)

(b)

Figure 55: a) The camera with panel of casing removed. b) The inside of the radiation box, showing the glycol chiller.

7.1.1.2 Setup for the manipulator

The Shadow Smart Grasping System (SSGS) provided by another industrial partner, the Shadow Robot Company [137], was also irradiated. The SSGS is composed of three identical manipulators and a base unit. It is a highly dexterous robotic end-effector, making it an ideal candidate to be irradiated for this experiment. One of the component manipulators can be seen in Fig. 56. It has three motors that control the three joints. Two finger-like joints along the length that modify their segment's pitch, and the base segment which rolls the whole manipulator sideways. The joints and how they bend are visible in Fig. 57b. The manipulator's casing is PA12 Nylon, and its tip is equipped with a pressure sensor.

The manipulator was placed inside the radiation box (see Fig. 53a). During the irradiation, the manipulator carried out a pre-set routine. Data on the manipulator's movement and other parameters were recorded in logs to be provide further information for analysis. A webcam was used to observe the irradiation (see Fig. 57), however mounting the webcam could only be accomplished without the box lid. With an open lid, the irradiation was carried out without cooling. The manipulator's motions provided a visual indicator for when

[vi]Due to miscommunication, the number of scans was calculated for a 23 MeV proton beam. In the experiment, 3 scans were conducted with a 28 MeV proton beam. The values for the stopping power and results in this work reflect the true setup

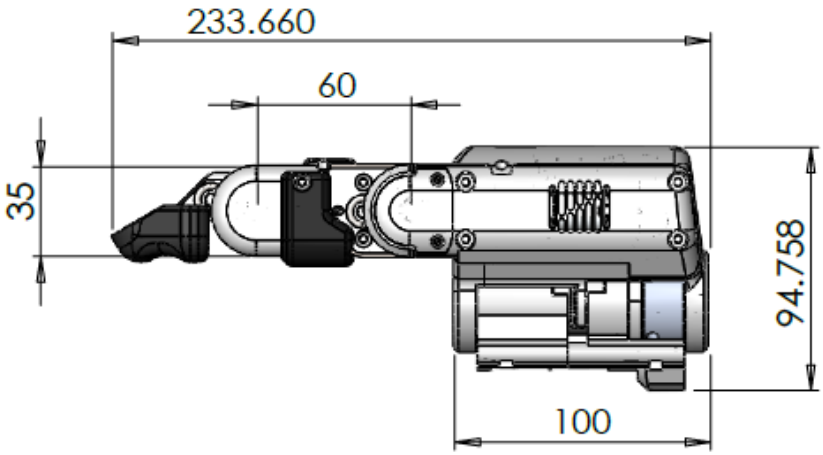

Figure 56: CAD model side view of one SSGS manipulator, with dimensions.

it ceased functioning correctly. The routine involved the movement of two of three motors (see Figs. 58 and 59), and within this study the beam was targeted on one specific motor. With a moving target, it was determined to be simpler to not perform the scanning motion and keep the beam position within the box fixed. The manipulator's routine continuously changed the irradiation target profile, which could not be accounted for by the scanning robot. It would therefore be much more difficult to determine radiation dose to the manipulator if both the target and the beam were moving. Gafchromic film was used to show where the beam had struck the manipulator, and the timing of the routine motions were used to determine how long the finger was in the beam.

The thickness and material of the manipulator casing provide an effective shielding against the beam; and due to concern about time constraints, it was anticipated that two irradiations would need to be assessed. The first irradiation would confirm the effectiveness of the manipulator casing, by directing the beam to enter the target through the base (Fig. 57a), where the casing is 8+ mm thick. Gafchromic film, sensitive to radiation like photographic film is to light, would be placed between the casing and the interior to verify penetration of the beam.

The second irradiation would strategically target one of the manipulator's motor drivers. Electronics are a more susceptible component to radiation, and this driver was also located under casing that was comparatively thin compared to the base. The manipulator would be turned 90°, so the beam would be perpendicular to the manipulator base, shown in Fig. 57b. The manipulator's movement would cause the beam to periodically pass over the target area.

The manipulator's routine was continuous during the irradiation to facilitate the detection of a fault, such as the failure or malfunction of a motor. First the main body joint twists, followed by the curl of the phalanges' joint to form a hook (see Fig. 58b and 59b). The

system then moves back to the original position following the same trajectory, where the fingertip applies pressure to a representative block of plastic directly underneath (see Fig. 58c and 59c). This was implemented to observe how the pressure sensor reacted in the radiated environment. After that, the manipulator relaxes the pressure on the block and commences the routine again.

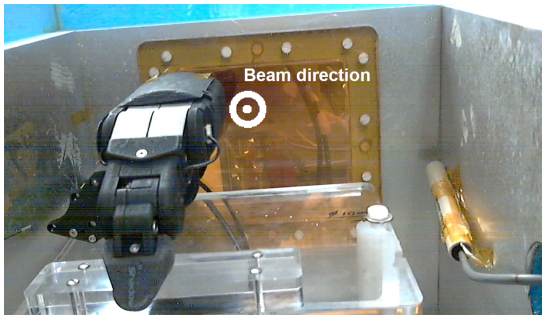

(a) The first orientation, where the beam travels the length of the manipulator, entering at the base. The manipulator is applying pressure on the Pyrex block underneath the tip, the final part of its routine.

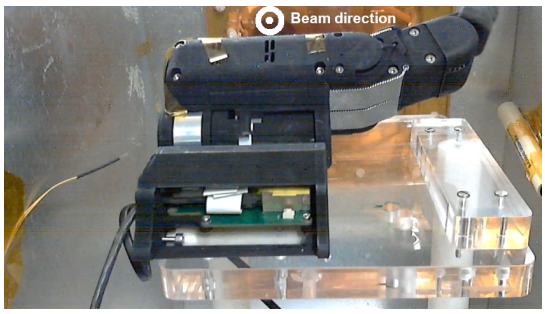

(b) The second irradiation orientation, the beam strikes the manipulator perpendicular to its length. The manipulator joints bend to demonstrate the manipulator is still functional, the second part of its routine.

Figure 57: Webcam images of the manipulator being irradiated. The webcam position is fixed; the proton beam enters the box through the radiation window in the background and exits the page.

7.1.2 Results and Discussion

This section will discuss the results of the two irradiations, first with the camera, and then the manipulator.

7.1.2.1 Camera Results

The camera disconnected after 26 ± 1 seconds, having undergone 7% of one scan. Assuming the beam did not penetrate the entire camera, this gives it a TID of 6.3 ± 0.2 Gy total irradiation.

The experiment was set up expecting at least one full scan to be completed, meaning Gafchromic film - providing a profile from the beam had been incident on the camera - was not present. Instead, the profile of the irradiation before the camera failed was simulated in FLUKA.

Hot pixels were visible during the irradiation, shown in the camera footage in figures 60a and 60b, before the camera failed abruptly. Some slight pixel degradation was measured afterwards, however it was not noticeable to the naked eye during the irradiation.

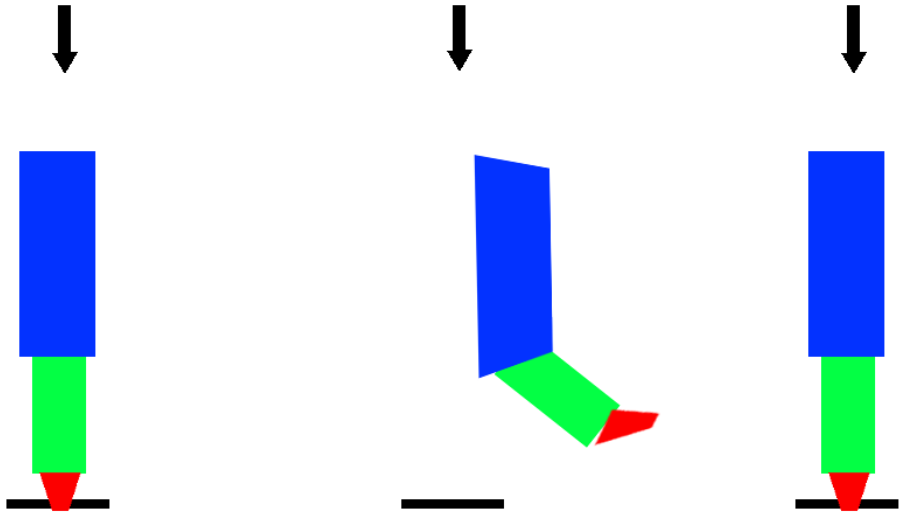

(a) (b) (c)

Figure 58: a) The manipulator starting position. b) The manipulator rotates sideways and curls perpendicular to the beam. c) The manipulator uncurls and applies pressure to the block below.

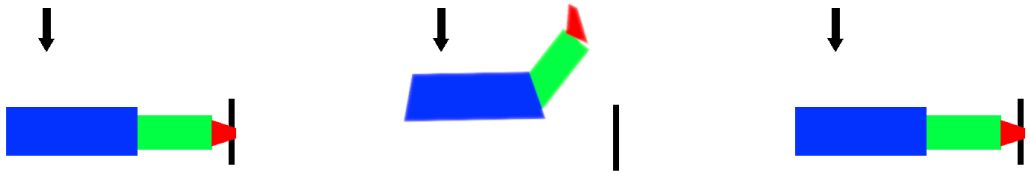

(a) (b) (c)

Figure 59: a) The manipulator starting position. b) The manipulator rotates sideways and curls into the beam. c) manipulator uncurls and applies pressure to the block below.

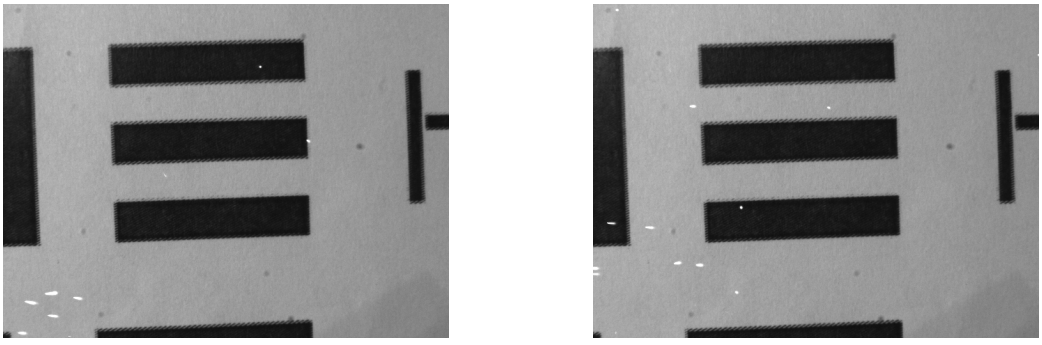

(a) (b)

Figure 60: Comparison between consecutive pictures (interval 1s), showing differing hot pixels caused by the radiation (white spots).

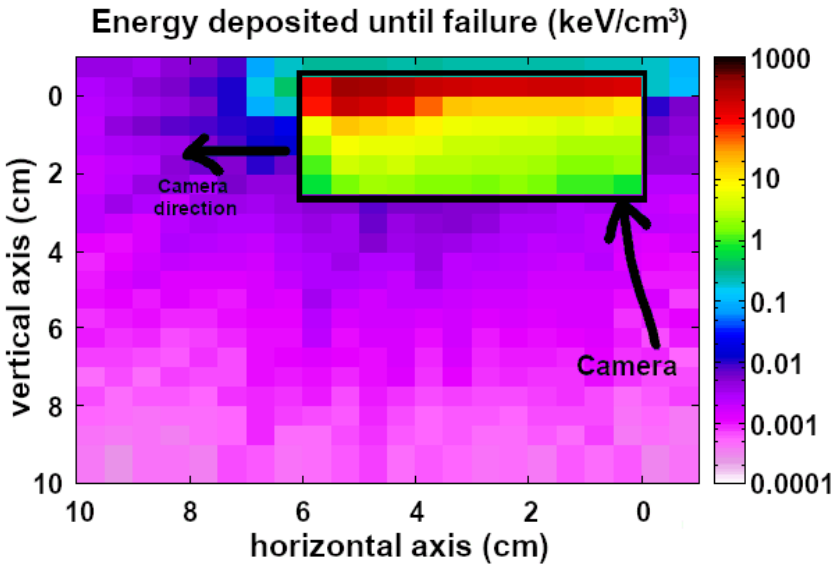

Figure 61: Illustrative FLUKA simulation of the irradiation. The camera profile is circled in black. The red area shows where the beam struck the camera. The yellow and green areas are energy deposited by secondary particles . The camera is in profile, without a lens, and the proton beam is directed through the page.

The camera irradiation was simulated in FLUKA to show where the radiation was deposited in the camera before its failure. The camera geometry was simplified for the simulation as a volume of $29 \times 29 \times 57$ mm^3, the camera dimensions without a lens. The geometry is made of two component volumes: an 0.8 mm thick aluminium shell, and an inner volume of PMMA as an approximate to circuit board (fibreglass bonded with epoxy resin). As there is no lens, it the simplified geometry is symmetrical across X, Y and Z. FLUKA cannot create a continuous movement for the scanning motion of the beam, however it can be approximated by 'pulsing' the beam for 1 s, and then moving it the same distance the beam would have moved during the live irradiation (0.4 cm horizontally, or 0.25 cm vertically at the end of the first row). The results of the simulation (Fig. 61) show how energy was deposited across the camera. The stripe of red high dose shows where the beam struck. It does not cover the entire camera profile because a complete scan of the camera had not been achieved at time of failure. The energy deposited by scattered secondary particles is not negligible, and the rest of the camera profile can be seen in the graph, shown in yellow and green. This shows that despite the small coverage of the beam, the radiation affected the whole camera. The graph is illustrative as the simulation was performed with the beam energy set to 23 MeV.

After the irradiation, indicator lights on rear of camera suggested functionality, but the computer did not recognise a device being connected. This was indicative of electrical failure corresponding to network communications rather than the camera sensor. However, as the camera uses an Ethernet cable for both power and data, it is not possible to determine definitively whether the CMOS chip failed, or the Ethernet port. Several days after the irradiation, the camera was tested and was operational, suggesting that the CMOS sensor and the Ethernet chips recovered from the irradiation.

This camera design is not optimised for use in a radioactive environment. Internal components would perform better if reconfigured - such as removing the Ethernet port from the camera body: keeping the power and data lines separate; using an optical link removing communication to a shielded area.

7.1.2.2 Manipulator results

The stopping power and average density of the manipulator were calculated in order to calculate the TID the manipulator had received. Using equation 8 of compound stopping power, the manipulator's stopping power was 16.57 $\pm$ MeV cm^2/g.

For the first irradiation the manipulator was orientated as in Fig. 57a. Because of the base twisting motion in the routine, it only spent two-thirds of the 15 s routine in the beam, tracing over an area of 7 cm x 1 cm. The irradiation lasted 18 $\pm$ 0.5 minutes, with no signs that the manipulator was degrading from the radiation exposure. After the irradiation, examining the gafchromic film indicated that the beam did not penetrate beyond the casing. This would mean the electronics behind the film were unirradiated. Using the stopping power

of nylon, the localised area received a total dose of 35.6 ± 1 kGy with no apparent loss of casing integrity [135].

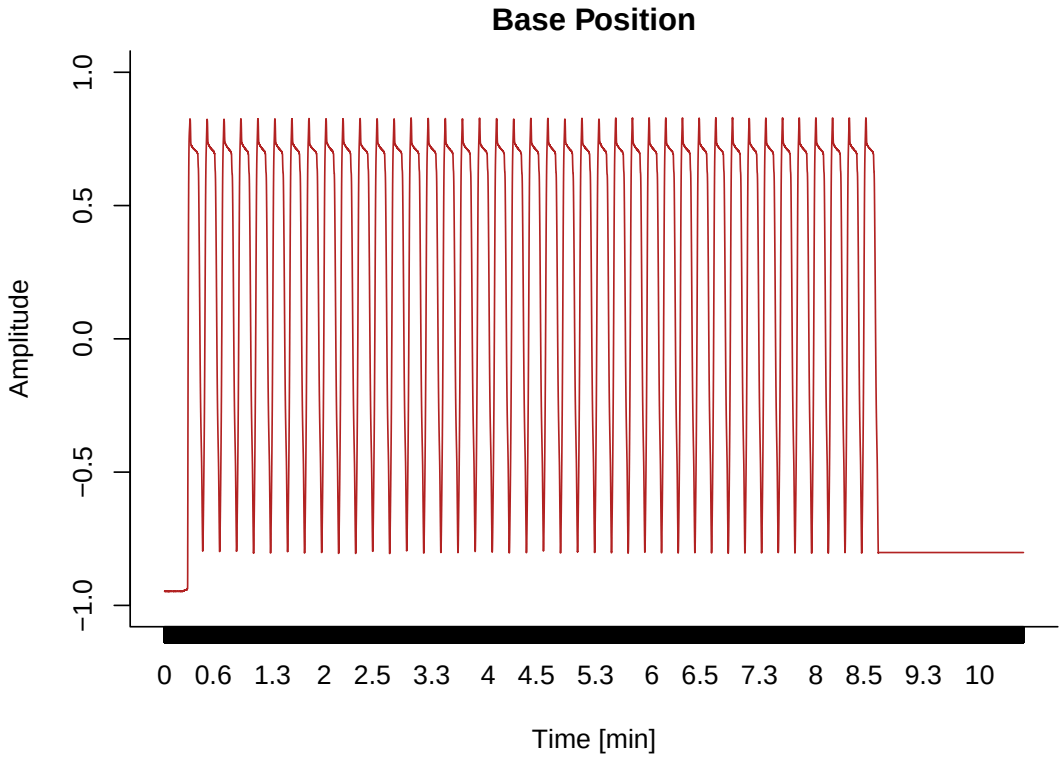

Figure 62: Base position of the manipulator for the second irradiation by time. The movement ceased after the 9 ± 0.5 minutes.

In the second irradiation the manipulator was orientated as in Fig. 57b. The cyclotron experienced some current drift, so the irradiation was carried out with a beam current of 5 nA. In this new orientation, the routine only manipulator spent one third of the integrated radiation time in the beam, however this was directly over the targeted motor driver, under 2 mm thick casing. As seen in Figure 62, the base of the manipulator stopped moving after 9 ± 0.5 minutes, signalling a failure of the motor's driver. Calculating from the stopping power for the whole manipulator, it received 4 ± 0.7 kGy at this 7 cm x 1 cm specific area irradiation.

Table 7 presents a summary of the irradiations' results. The robotic manipulator received ± kGy targeted over its motor driver at time of failure, and its casing survived 35.6 ± kGy, while the camera failed after 3.5 ± 0.1 Gy. The radiation levels expected for the ATLAS decommissioning have a maximum radiation estimated at 93 mSv/h after 28 days cooldown[vii].

[vii]The decommissioning of the ATLAS ID will be carried out by human technicians, work is not expected to begin until 257 days cooldown time.

-	**Camera**	**Manipulator 1st irradiation**	**Manipulator 2nd irradiation**
Beam Parameters	28 MeV, 10nA	28 MeV, 10 nA	28 MeV, 5 nA
Type of irradiation	scanning	static	static
Length of irradiation	26 s	18 min	9 min
TID (Gy)	3.5 ± 0.1	35600 ± 1000	4000 ± 700
Destructive?	yes	no	yes

Table 7: Comparison table of the irradiation results.

Converting Grays to Sieverts (see Section 2.4.2), the TID is multiplied by a weighting factor which is determined by the radiation type. For protons, this is $W = 2$. Therefore the robotic manipulator's motor driver failed at 42 $\times 10^6$ mSv, and the camera at 22 $\times 10^3$ mSv. This would theoretically allow them to work for at least 45000 hours and 235 hours respectively - though this estimate is not adjusted for the different radiation profile inside the ATLAS cavern, or the gradual decrease in radiation as the detector cools down. The manipulator's high radiation tolerance is beneficial, as a robot's manipulators would be closer to, and physically interacting with, radioactive sources or activated materials. The camera's comparatively low tolerance can be accommodated by strategically mounting it further away from the high fluence areas, or providing it with extra shielding.

By contrast, a human radiation worker's dosage is limited by the ICRP in 2007 to 50 mSv/year maximum, and 20 mSv average over 5 years [35].

7.2 Follow-up experiment inside the cyclotron vault

A collimated proton beam does not accurately reflect the radiation profile of a decommissioning scenario. Radiation originating from activated materials will have varying energies, multi-directional, and different particles. Therefore a second experiment inside the cyclotron vault is proposed. The experiment would be placed in the vault and parasitically absorb the backscatter radiation from the active cyclotron. This backscatter would primarily be very high gamma and fast neutrons, estimated in the order of Sv/h for gamma, and ten times that for neutrons. As seen at the end of 2.1, the main components of the radiation field inside the ATLAS cavern are neutrons and gamma. The parasitic approach would also permit the experiment to run for an indefinite amount of time, and not impinge on the cyclotron's other commitments. Using the cyclotron vault introduces new challenges. The intensity of the radiation would fluctuate, as the cyclotron is activated or not. There would also likely be a non-negligible time lapse between the component malfunctioning, and safe access to the vault (cyclotron safely powering down, radiation dissipating to safe levels etc). It would therefore be crucial to measure each of those fields in real time, to accurately calculate the amount of radiation to which the target had been subjected.

Standard personal dosimeters are likely to saturate as these levels are beyond their expected operating parameters. For example, the Tracerco PED Blue overloads at 0.1 Sv/h (or 1 Sv/h for the extended range) and is sensitive to X-ray and Gamma ray radiation between 33keV to 3MeV (48keV to 3MeV) [121]. Personal dosimeters would therefore be unsuitable to measure the radiation field inside the vault.

Two possible methods to measure the mixed radiation field are available. The first method utilises two complementary ionization chambers. One ionization chamber would use tissue equivalent plastic (TE), sensitive to both neutrons and gamma rays; and the second would be aluminium or graphite, sensitive to gamma rays only. The neutron field can be assumed from the difference between the two signals. This is an established method for characterising mixed gamma-neutron fields [141]. Assembly in situ would be required, however the experiment's electronics would be kept outside the vault, protected from the radiation.

The second method would make use of RADMON radiation monitors, which are used inside the LHC tunnel and the experimental caverns where the radiation is also mixed gamma-neutron. The RADMON unit comprises of two different types of sensors: p-channel MOS transistors (also known as RadFETs) and p-i-n diodes. These measure the TID and the neutron equivalent fluence respectively [142]. As they have been designed to work in close proximity to the ATLAS-ID (high radiation levels with limited access), the RADMON unit would be suitable to monitor the radiation inside the cyclotron vault. Using a RADMON unit over the ionisation chambers will simplify the experimental setup and data taking. As the beamline experiment showed, both the camera and the manipulator had definitive point of failures. These can be monitored remotely, with a program to alert at time-of-failure. Given an accurate time of failure and the RADMON unit recording the radiation profile, the experiment could be left unattended until the components failed and needed retrieving.

The realisation of this experiment was not possible within the timescale of this thesis.

8 Summary

This thesis presents the development of a Virtual Reality Intervention Planning Platform; its initial design and proof of concept using the Birmingham cyclotron vault in Chapter 5, and the addition of Motion Capture data to simulate the ATLAS ID decommissioning in Chapter 6. By providing a virtual facsimile of the target environment, technicians can train for the required work without entering the hazardous environment. As potential obstacles can be identified using this platform, technicians will be able to approach the work prepared, reducing the amount of time they will spend in the radioactive environment, and decrease their overall exposure and total dose. The proof of concept in chapter 5.3 showed that the platform returns reliable results. However, it is dependant on its radiation dose maps for accuracy. In chapter 6, the motion capture of a technician performing real decommissioning steps on the ATLAS Mockup was added to the platform. The decommissioning tasks simulated using motion capture totalled 3 hours 7 minutes, with a TID exposure of 14.75 μSv, $\pm$ 13%. This simulation revealed that the technician spent significant amounts of time in close proximity to the beampipe, which is the most radioactive section of the detector. Further development of the Virtual Reality Intervention Platform would include the addition of Digital Twins. A physical robot with a linked virtual double, or 'twin', would carry out decommissioning tasks, and be controlled from the Virtual Reality Intervention Platform.

Chapter 7 presented the irradiation of a robotic manipulator and camera. The manipulator failed at 4 $\pm$ 0.7 kGy targeted over one of the motor drivers, however the camera could only withstand 3.5 $\pm$ 0.1 Gy before disconnecting. The manipulator is suited for decommissioning work, while the camera design presented vulnerabilities to a high radiation environment. Both however, can withstand higher doses of radiation that a human technician, though the camera would be better located in an area where radiation is less intense. This experiment was conducted to assess the feasibility of robotic interventions in for future ATLAS decommissioning, in the case where human presence would be limited. A benchmark radiation tolerance provides technician with a lifetime estimation, which can be used for the initial selection of components, and also preempting interruptions due to impromptu mechanical failure. Further continuation of this work includes a follow-up experiment inside the Birmingham cyclotron vault, where the radiation field is gamma-neutron mixed field, similar to the ATLAS cavern and industrial nuclear decommissioning scenarios. This would give a clearer indication of radiation tolerance for the specific work.

Continuing to probe physics beyond the Standard Model requires colliders and detectors of increasing scale, operating at higher energies and intensities. The HL-LHC aims to increase the luminosity of the current machine by ten, and its proposed successor, the Future Circular Collider is already being discussed. The unavoidable byproduct of these experiments is an increase of radiation, as the intense particle collisions activate the detector materials.

Maintenance and decommissioning work are still required despite the hostile environment. However, reliance on human interventions for such tasks is unsustainable and other methods must be researched. Virtual Reality and complex robotics are emerging technologies that are well-suited to be employed for partial or completely remote interventions.

Bibliography

[1] W. Frass, *Passage of particles through matter*, University Lecture Notes, Accessed: 2021-03-16, 2009. [Online]. Available: www2.physics.ox.ac.uk/sites/default/files/Passage.pdf.

[2] Y. S. Kim, "Density effect in dE/dx of fast charged particles traversing various biological materials," *Radiation Research*, vol. 56, no. 1, pp. 21–27, 1973, ISSN: 00337587, 19385404.

[3] M. Tanabashi *et al.*, "Review of particle physics," *Phys. Rev. D*, vol. 98, p. 030 001, 3 Aug. 2018. DOI: 10.1103/PhysRevD.98.030001.

[4] S. Grdanovska, "Characterization of radiation damage to a novel photonic crystal sensor," Ph.D. dissertation, University of Maryland, Jan. 2015. DOI: 10.13016/M2BZ0D.

[5] M. Vins *et al.*, "Determination of impurities concentration inside the silicon monocrystal by the neutron activation analysis," in *2013 3rd International Conference on Advancements in Nuclear Instrumentation, Measurement Methods and their Applications (ANIMMA)*, 2013, pp. 1–4. DOI: 10.1109/ANIMMA.2013.6728096.

[6] M. Verheijke, "Instrumental neutron activation analysis developed for silicon integrated circuit technology," Proefschrift., Ph.D. dissertation, Technische Universiteit Eindhoven, 1992. DOI: 10.6100/IR372911.

[7] G. S. Bauer, "Physics and technology of spallation neutron sources," *Nuclear Instruments and Methods in Physics Research Section A: Accelerators, Spectrometers, Detectors and Associated Equipment*, vol. 463, no. 3, pp. 505–543, 2001.

[8] M. Berger *et al.*, *Xcom: Photon cross section database (version 1.5) [online]*, Accessed: 2021-03-15, National Institute of Standards and Technology, Gaithersburg, MD. [Online]. Available: physics.nist.gov/xcom.

[9] "Interactive web pages for radiation environment exploration of ATLAS," CERN, Geneva, Tech. Rep., Oct. 2020, All figures including auxiliary figures are available at https://atlas.web.cern.ch/Atlas/GROUPS/PHYSICS/PUBNOTES/ATL-SOFT-PUB-2020-003. [Online]. Available: http://cds.cern.ch/record/2742378.

[10] I. Boyko *et al.*, "Measurement of the radiation environment of the ATLAS cavern in 2017–2018 with ATLAS-GaAsPix detectors," vol. 16, no. 01, P01031–P01031, Jan. 2021. DOI: 10.1088/1748-0221/16/01/p01031.

[11] S. Seidel, "Silicon strip and pixel detectors for particle physics experiments," *Physics Reports*, vol. 828, pp. 1–34, 2019, Silicon strip and pixel detectors for particle physics experiments, ISSN: 0370-1573. DOI: doi.org/10.1016/j.physrep.2019.09.003.

[12] F. Hartmann, *Evolution of Silicon Sensor Technology in Particle Physics, Second Edition*, ser. Springer Tracts in Modern Physics 275. Springer, 2017.

[13] The ATLAS Collaboration, "The ATLAS Experiment at the CERN Large Hadron Collider," *Journal of Instrumentation*, vol. 3, no. 08, S08003, 2008.

[14] A. Ahmad *et al.*, "The silicon microstrip sensors of the atlas semiconductor tracker," *Nuclear Instruments and Methods in Physics Research Section A: Accelerators, Spectrometers, Detectors and Associated Equipment*, vol. 578, no. 1, pp. 98–118, 2007, ISSN: 0168-9002. DOI: doi.org/10.1016/j.nima.2007.04.157.

[15] J. Vossebeld, *Particle detection techniques in hep: Lecture 3: Solid state tracking detectors*, accessed: 2021-08-31. [Online]. Available: hep.ph.liv.ac.uk/~gcasse/Postgrad-detectors/Lecture3SolidStateTrackingDetectors.pdf.

[16] N. Pacifico *et al.*, "An annealing study of charge collection efficiency on float-zone p-on-n ministrip sensors irradiated with 24 GeV/c protons and 20 MeV neutrons," *Journal of Instrumentation*, vol. 10, no. 08, P08005–P08005, Aug. 2015. DOI: 10.1088/1748-0221/10/08/p08005.

[17] H. Spieler, "Introduction to radiation-resistant semiconductor devices and circuits," *AIP Conference Proceedings*, vol. 390, no. 1, pp. 23–49, 1997. DOI: 10.1063/1.52282.

[18] I. Mandić *et al.*, "Online radiation dose measurement system for ATLAS experiment," in *2009 1st International Conference on Advancements in Nuclear Instrumentation, Measurement Methods and their Applications*, 2009, pp. 1–7.

[19] H. Feick, "Radiation Tolerance of Silicon Particle Detectors for High-Energy Physics experiments," Presented on Aug 1997, Ph.D. dissertation, Universität Hamburg, 1997. [Online]. Available: cds.cern.ch/record/335685.

[20] R. Harper, "Radiation damage studies of silicon detectors and searching for an intermediate mass Higgs boson at ATLAS," Ph.D. dissertation, University of Sheffield, 2001.

[21] The ATLAS SCT Collaboration, "Beam tests of ATLAS SCT silicon strip detector modules," *Nuclear Instruments and Methods in Physics Research Section A: Accelerators, Spectrometers, Detectors and Associated Equipment*, vol. 538, no. 1, pp. 384–407, 2005, ISSN: 0168-9002. DOI: 10.1016/j.nima.2004.08.133.

[22] I. V. Gorelov, "A Leakage Current-based Measurement of the Radiation Damage in the ATLAS Pixel Detector," CERN, Geneva, Tech. Rep., Dec. 2014. DOI: 10.1088/1748-0221/10/04/C04024. arXiv: 1501.07192.

[23] M. Moll, "Displacement damage in silicon detectors for high energy physics," *IEEE Transactions on Nuclear Science*, vol. 65, no. 8, pp. 1561–1582, 2018. DOI: 10.1109/TNS.2018.2819506.

[24] I. Dawson, Ed., *Radiation effects in the LHC experiments: Impact on detector performance and operation*, ser. CERN Yellow Reports: Monographs. Geneva: CERN, 2021, vol. 1/2021, ISBN: 978-92-9083-590-5. DOI: 10.23731/CYRM-2021-001.

[25] *Radiation damage in 2015-2017 atlas preliminary ibl figure 02*, 2021-08-2021, 2021. [Online]. Available: atlas.web.cern.ch/Atlas/GROUPS/PHYSICS/PLOTS/PIX-2018-005.

[26] R. A. Powsner *et al.*, *Essentials of Nuclear Medicine Physics and Instrumentation*. John Wiley & Sons, Incorporated, 2013.

[27] S. N. Ahmed, "Dosimetry and radiation protection," in *Physics and Engineering of Radiation Detection*, Second Edition. Elsevier, 2015, ch. 11, p. 677, ISBN: 978-0-12-801363-2. DOI: 10.1016/B978-0-12-801363-2.00011-5.

[28] *Medical Management of Radiation Injuries*, ser. Safety Reports Series 101. Vienna: INTERNATIONAL ATOMIC ENERGY AGENCY, 2020, ISBN: 978-92-0-107019-7. [Online]. Available: https://www.iaea.org/publications/12370/medical-management-of-radiation-injuries.

[29] K. Cohen *et al.*, *Medical Management of Radiation Accidents*. Taylor & Francis, 2001, ISBN: 9781420037197.

[30] D. E. Green and C. T. Rubin, "Consequences of irradiation on bone and marrow phenotypes, and its relation to disruption of hematopoietic precursors," eng, *Bone*, vol. 63, pp. 87–94, Jun. 2014, S8756-3282(14)00064-7[PII], ISSN: 1873-2763. DOI: 10.1016/j.bone.2014.02.018. [Online]. Available: https://doi.org/10.1016/j.bone.2014.02.018.

[31] S. J. McMahon, "The linear quadratic model: Usage, interpretation and challenges," *Physics in Medicine & Biology*, vol. 64, no. 1, 01TR01, Dec. 2018. DOI: 10.1088/1361-6560/aaf26a.

[32] D. W. Kufe *et al.*, *Holland-Frei Cancer Medicine*, 6th Edition. Decker Periodicals Publ Incorporated, 2003.

[33] W. B. Oatway *et al.*, "Ionising radiation exposure of the UK population: 2010 review," Public Health England, Apr. 2016.

[34] D. Hart *et al.*, "Frequency and collective dose for medical and dental x-ray examinations in the UK, 2008," Health Protection Agency, Dec. 2010.

[35] ICRP, "The 2007 Recommendations of the International Commission on Radiological Protection. ICRP Publication 103," *Annals of the ICRP*, vol. 37, no. 2-4, 2007.

[36] IAEA, "Deterministic effects on the central nervous system and lethal doses," in *Health Effects and Medical Surveillance*, ser. Practical Radiation Technical Manual 3 (Rev. 1). Vienna: IAEA, 2004, ch. 14, p. 30.

[37] EURATOM, *Directive 2013/59/Euratom - protection against ionising radiation*, Accessed: 2021-03-15, 2013.

[38] D. F.-W. et al, "Radiation protection aspects Proceedings, LHC Performance Workshop (Chamonix 2014): Chamonix, France, September 22-25, 2014," M. Draper, Ed., ser. CERN Yellow Reports: Conference Proceedings, Geneva: CERN, 2015, p. 276. DOI: 10.5170/CERN-2015-002.

[39] R. P. Group, *How to obtain a dosimeter*, Accessed: 2021-03-15, CERN Occupational Health & Safety and Environmental Protection Unit. [Online]. Available: dosimetry.web.cern.ch/dosimeters/how-obtain-dosimeter.

[40] ICRP, "Objectives of radiation protection," *Annals of the ICRP*, vol. 1, no. 3, pp. 2–3, 1977, PMID: 29742853. DOI: 10.1016/0146-6453(77)90002-1.

[41] D. J. Strom *et al.*, "Collective dose as a performance measure for occupational radiation protection programs: Issues and recommendations," Tech. Rep., 1998, PNNL–11934, p. 63. [Online]. Available: osti.gov/servlets/purl/291000.

[42] D. Forkel-Wirth *et al.*, "Radiation protection at CERN," in *Proceedings, CERN Accelerator School on High Power Hadron Machines*, 2013, pp. 415–436. DOI: 10.5170/CERN-2013-001.415. arXiv: 1303.6519 [physics.acc-ph].

[43] D. Forkel-Wirth, *Zonage radiologique au CERN - Area Classification*, 2006. [Online]. Available: edms.cern.ch/document/810149/1.

[44] T. Shears, "The Standard Model," *Philosophical Transactions of the Royal Society A: Mathematical, Physical and Engineering Sciences*, vol. 370, no. 1961, pp. 805–817, Feb. 2012. DOI: 10.1098/rsta.2011.0314.

[45] E. Mobs, "The CERN accelerator complex - 2019. Complexe des accélérateurs du CERN - 2019," Jul. 2019, General Photo. [Online]. Available: cds.cern.ch/record/2684277.

[46] J. T. Boyd, "LHC Run-2 and Future Prospects," 2020. arXiv: 2001.04370 [hep-ex]. [Online]. Available: arxiv.org/abs/2001.04370.

[47] E. Torrence, *Luminositypublicresultsrun2*, Accessed: 2021-03-15. [Online]. Available: twiki.cern.ch/twiki/bin/view/AtlasPublic/LuminosityPublicResultsRun2.

[48] T. G. Vincenzo Chiochia Günther Dissertori, *Accelerators and collider experiments*, Feb. 2010.

[49] A.-L. Poley, "Studies of adhesives and metal contacts on silicon strip sensors for the ATLAS Inner Tracker," Ph.D. dissertation, Humboldt Universität, Berlin, Hamburg, 2018. DOI: 10.3204/PUBDB-2018-01870.

[50] The ATLAS Collaboration, "ATLAS Inner Detector: Technical Design Report, 1," CERN, Geneva, Tech. Rep., 1997. [Online]. Available: cds.cern.ch/record/331063.

[51] The ATLAS Collaboration, "ATLAS pixel detector electronics and sensors," *Journal of Instrumentation*, vol. 3, P07007, 2008. DOI: 10.1088/1748-0221/3/07/P07007.

[52] The ATLAS Collaboration, "Combined performance tests before installation of the ATLAS semiconductor and transition radiation tracking detectors," *Journal of Instrumentation*, vol. 3, no. 08, P08003–P08003, Aug. 2008. DOI: 10.1088/1748-0221/3/08/p08003.

[53] The ATLAS Collaboration, "ATLAS Liquid Argon Calorimeter: Technical Design Report," CERN, Geneva, Tech. Rep., 1996. [Online]. Available: cds.cern.ch/record/331061.

[54] The ATLAS Collaboration, "Readiness of the ATLAS Tile Calorimeter for LHC collisions," *The European Physical Journal C*, vol. 70, no. 4, pp. 1193–1236, 2010.

[55] J. Pequenao, "Computer generated image of the whole ATLAS detector," Mar. 2008, [Online]. Available: cds.cern.ch/record/1095924.

[56] J. Pequenao, "Computer generated image of the ATLAS Inner Detector," Mar. 2008, [Online]. Available: cds.cern.ch/record/1095926.

[57] M. Capeans *et al.*, "ATLAS Insertable B-Layer Technical Design Report," CERN, Tech. Rep. CERN-LHCC-2010-013. ATLAS-TDR-19, Sep. 2010. [Online]. Available: cds.cern.ch/record/1291633.

[58] B. Mindur *et al.*, "Gas gain stabilisation in the ATLAS TRT detector," *Journal of Instrumentation*, vol. 11, no. 04, P04027–P04027, Apr. 2016. DOI: 10.1088/1748-0221/11/04/p04027.

[59] H. Pernegger, "The Pixel detector of the ATLAS experiment for LHC Run-2," *Journal of Instrumentation*, vol. 10, no. 06, p. C06012, 2015.

[60] M. Backhaus, "The upgraded Pixel Detector of the ATLAS Experiment for Run 2 at the Large Hadron Collider," *Nuclear Instruments and Methods in Physics Research Section A: Accelerators, Spectrometers, Detectors and Associated Equipment*, vol. 831, pp. 65–70, 2016, Proceedings of the 10th International "Hiroshima" Symposium on the

Development and Application of Semiconductor Tracking Detectors, ISSN: 0168-9002. DOI: 10.1016/j.nima.2016.05.018.

[61] D. Robinson *et al.*, "Silicon microstrip detectors for the ATLAS sct," *Nuclear Instruments and Methods in Physics Research Section A: Accelerators, Spectrometers, Detectors and Associated Equipment*, vol. 485, no. 1, pp. 84–88, 2002, Proceedings of the 5th International Conference on Large Scale Applications and Radiation Hardness of Semiconductor Detectors, ISSN: 0168-9002. DOI: 10.1016/S0168-9002(02)00536-3.

[62] A. Abdesselam *et al.*, "The ATLAS semiconductor tracker end-cap module," *Nuclear Instruments and Methods in Physics Research Section A*, vol. 575, pp. 353–389, 2007. DOI: 10.1016/j.nima.2007.02.019.

[63] A. Bingul, "The ATLAS TRT and its performance at LHC," *J. Phys. Conf. Ser.*, vol. 347, S. A. Cetin *et al.*, Eds., p. 012 025, 2012. DOI: 10.1088/1742-6596/347/1/012025.

[64] The ATLAS TRT Collaboration, "The ATLAS TRT end-cap detectors," *Journal of Instrumentation*, vol. 3, no. 10, P10003–P10003, Oct. 2008. DOI: 10.1088/1748-0221/3/10/p10003.

[65] The ATLAS Collaboration, "Technical Design Report for the ATLAS Inner Tracker Strip Detector," CERN, Geneva, Tech. Rep., Apr. 2017. [Online]. Available: cds.cern.ch/record/2257755.

[66] O. Solovyanov and A. Collaboration, "Status and progress on the ATLAS Phase-II detector upgrades," Jul. 2021. [Online]. Available: https://cds.cern.ch/record/2775148.

[67] J. Pequenao, "Computer Generated image of The ATLAS Calorimeter," Mar. 2008, [Online]. Available: cds.cern.ch/record/1095927.

[68] M. Livan and R. Wigmans, "Misconceptions about Calorimetry," *Instruments*, vol. 1, no. 1, p. 3, 2017. DOI: 10.3390/instruments1010003. arXiv: 1704.00661 [physics.ins-det].

[69] H. Zhang, A. L. A. C. Group, *et al.*, "The ATLAS Liquid Argon calorimeter: Overview and performance," in *Journal of Physics: Conference Series*, IOP Publishing, vol. 293, 2011, p. 012 044.

[70] J. Turner, "Upgrade plans for atlas forward calorimetry for the hl-lhc," *Physics Procedia*, vol. 37, pp. 301–308, 2012, Proceedings of the 2nd International Conference on Technology and Instrumentation in Particle Physics (TIPP 2011), ISSN: 1875-3892. DOI: doi.org/10.1016/j.phpro.2012.02.376.

[71] M. Brice, "Installing The ATLAS Calorimeter. Vue centrale du détecteur ATLAS avec ses huit toroides entourant le calorimètre avant son déplacement au centre du détecteur," Nov. 2005, [Online]. Available: cds.cern.ch/record/910381.

[72] H. Rammer, "Novel Technique for the UX15 Cavern Vault Support System," no. CERN-ST-2000-021, 5 p, Jan. 2000. [Online]. Available: cds.cern.ch/record/435991.

[73] I. Dawson and V. Hedberg, "Radiation in the USA15 cavern in ATLAS," 2004. [Online]. Available: cds.cern.ch/record/734133.

[74] S. Dailler, "ATLAS underground works, axonometric view.. Point 1: zone d'expérience ATLAS, vue axonométrique et vue en plan.," AC Collection. Legacy of AC. Pictures from 1992 to 2002., Jul. 1997, [Online]. Available: cds.cern.ch/record/842353.

[75] C. Marcelloni, "Installation of the ATLAS pixel detector into the cavern," Jun. 2007, [Online]. Available: cds.cern.ch/record/1043639.

[76] H. H. Ten Kate, "Atlas magnet system nearing completion," *IEEE transactions on applied superconductivity*, vol. 18, no. 2, pp. 352–355, 2008.

[77] D. E. Baynham *et al.*, "Atlas end cap toroid final integration, test and installation," *IEEE Transactions on Applied Superconductivity*, vol. 18, no. 2, pp. 391–394, 2008. DOI: 10.1109/TASC.2008.920668.

[78] S. Palestini, "Status of the commissioning of atlas," *Nuclear Physics B - Proceedings Supplements*, vol. 197, no. 1, pp. 3–8, 2009, 11th Topical Seminar on Innovative Particle and Radiation Detectors (IPRD08), ISSN: 0920-5632. DOI: 10.1016/j.nuclphysbps.2009.10.023.

[79] I. Dawson, "Radiation background simulation and verification at the LHC: Examples from the ATLAS experiment and its upgrades," *PoS*, vol. Vertex2012, p. 015, 2013. DOI: 10.22323/1.167.0015.

[80] S. Baranov *et al.*, "Estimation of Radiation Background, Impact on Detectors, Activation and Shielding Optimization in ATLAS," Jan. 2005. [Online]. Available: cds.cern.ch/record/814823.

[81] A. Fasso *et al.*, "Predicting induced radioactivity at high-energy electron accelerators," in *Proceedings, 9th International Conference on Radiation Shielding: Tsukuba, Japan, October 17-22, 1999*, vol. 37, 2000.

[82] Z. Zajacova, "Assessment of radiological risks at the ATLAS experiment," Ph.D. dissertation, Slovak University of Technology, 2009. [Online]. Available: inis.iaea.org/collection/NCLCollectionStore/_Public/47/127/47127159.pdf.

[83] D. P. Landau and K. Binder, *A Guide to Monte Carlo Simulations in Statistical Physics*. Cambridge, UNITED KINGDOM: Cambridge University Press, 2000, ISBN: 9780511151224.

[84] W. L. Dunn and J. K. Shultis, Eds., *Exploring Monte Carlo Methods*. Amsterdam: Elsevier, 2012, ISBN: 978-0-444-51575-9.

[85] M. Hanada, *Markov Chain Monte Carlo for Dummies*, Aug. 2018. arXiv: 1808.08490 [hep-th].

[86] M. Di Castro, "A Novel Robotic Framework for Safe Inspection and Telemanipulation in Hazardous and Unstructured Environments," Presented 27 Sep 2019, 2019. [Online]. Available: cds.cern.ch/record/2729727.

[87] The ATLAS Collaboration, "Technical Design Report for the ATLAS ITk Pixel Detector," CERN, Geneva, Tech. Rep. ATL-COM-ITK-2018-019, Mar. 2018. [Online]. Available: cds.cern.ch/record/2310230.

[88] K. Veale *et al.*, "Decommissioning procedure for the Inner Detector during LS3," 2008, [Online]. Available: edms.cern.ch/document/2003719/1.

[89] "ATLAS Phase-II Upgrade Scoping Document," CERN, Geneva, Tech. Rep. CERN-LHCC-2015-020. LHCC-G-166, Sep. 2015. [Online]. Available: cds.cern.ch/record/2055248.

[90] P. Barker, "Virtual reality: Theoretical basis, practical applications," *Research in Learning Technology*, vol. 1, no. 1, Jan. 1. DOI: 10.3402/rlt.v1i1.9463.

[91] C. Flavián *et al.*, "The impact of virtual, augmented and mixed reality technologies on the customer experience," *Journal of Business Research*, vol. 100, pp. 547–560, 2019, ISSN: 0148-2963. DOI: 10.1016/j.jbusres.2018.10.050.

[92] Virtalis, *Visionary Render (2019.2)*, Accessed: 2021-03-16, 2019. [Online]. Available: virtalis.com.

[93] W. R. Sherman and A. B. Craig, *Understanding Virtual Reality: Interface, Application, and Design*. San Francisco, CA, USA: Morgan Kaufmann Publishers Inc., 2002, ISBN: 9780080520094.

[94] R. Schroeder, "Defining virtual worlds and virtual environments," *Journal For Virtual Worlds Research*, vol. 1, no. 1, Jan. 1970. DOI: 10.4101/jvwr.v1i1.294.

[95] C. Girvan, "What is a virtual world? definition and classification," *Educational Technology Research and Development*, vol. 66, no. 5, pp. 1087–1100, Feb. 2018. DOI: 10.1007/s11423-018-9577-y.

[96] Solidworks, *3D CAD Design Software*, Accessed: 2021-03-15. [Online]. Available: solidworks.com.

[97] A. Benini, "Localization and navigation of autonomous systems in complex scenarios," Ph.D. dissertation, Oct. 2010. DOI: 10.13140/RG.2.2.17142.40007.

[98] HTC, *HTC Vive*, Accessed: 2021-03-16, 2020. [Online]. Available: vive.com.

[99] J. Perret and E. Vander Poorten, "Touching virtual reality: A review of haptic gloves," Jun. 2018.

[100] H. Son *et al.*, "Realwalk: Haptic shoes using actuated mr fluid for walking in vr," in *2019 IEEE World Haptics Conference (WHC)*, 2019, pp. 241–246.

[101] TeslaSuit, *Teslasuit*, Accessed: 2021-03-16, 2020. [Online]. Available: teslasuit.io.

[102] D. Trinitatova and D. Tsetserukou, "Deltatouch: A 3D haptic display for delivering multimodal tactile stimuli at the palm," in *2019 IEEE World Haptics Conference (WHC)*, 2019, pp. 73–78.

[103] B. Kleinsman-Leusink-Hill *et al.*, "Thermal and haptic interface design: Adding sensory feedback to vr/ar," in *2018 IEEE International Instrumentation and Measurement Technology Conference (I2MTC)*, 2018, pp. 1–6.

[104] N. Ranasinghe *et al.*, "Ambiotherm: Simulating ambient temperatures and wind conditions in VR environments," Oct. 2016, pp. 85–86, ISBN: 9781450345316. DOI: 10.1145/2984751.2985712.

[105] K. T. Wave, *VR Sense*, Accessed: 2021-03-16, 2017. [Online]. Available: koeitecmo.co.jp/news/2017/06/vr-vr.html.

[106] E. Kerruish, "Arranging sensations: Smell and taste in augmented and virtual reality," *The Senses and Society*, vol. 14, no. 1, pp. 31–45, 2019. DOI: 10.1080/17458927.2018.1556952.

[107] J. J. Cummings and J. N. Bailenson, "How immersive is enough? a meta-analysis of the effect of immersive technology on user presence," *Media Psychology*, vol. 19, no. 2, pp. 272–309, 2016. DOI: 10.1080/15213269.2015.1015740.

[108] W. Wirth *et al.*, "A process model of the formation of spatial presence experiences," *Media Psychology*, vol. 9, no. 3, pp. 493–525, 2007. DOI: 10.1080/15213260701283079.

[109] A. Spagnolli *et al.*, "Mediated presence: Virtual reality, mixed environments and social networks," *Virtual Reality*, vol. 13, no. 3, pp. 137–139, Sep. 2009, ISSN: 1434-9957. DOI: 10.1007/s10055-009-0128-z.

[110] A. Lécuyer, "Playing with senses in VR: Alternate perceptions combining vision and touch," *IEEE Computer Graphics and Applications*, vol. 37, no. 1, pp. 20–26, Jan. 2017. DOI: 10.1109/MCG.2017.14.

[111] H. Akiduki *et al.*, "Visual-vestibular conflict induced by virtual reality in humans," *Neuroscience letters*, vol. 340, no. 3, pp. 197–200, Apr. 2003, ISSN: 0304-3940. DOI: 10.1016/s0304-3940(03)00098-3.

[112] S. Weech *et al.*, "Presence and cybersickness in virtual reality are negatively related: A review," *Frontiers in Psychology*, vol. 10, p. 158, 2019, ISSN: 1664-1078. DOI: 10.3389/fpsyg.2019.00158.

[113] A. Jacquard and H. Planes, *Petite philosophie a l'usage des non-philosophes*, ser. Livre de poche. Librairie generale francaise, 1999.

[114] Valve, *Steamvr*, Accessed: 2021-03-15. [Online]. Available: steamcommunity.com/steamvr.

[115] A. Cryer *et al.*, "Advantages of virtual reality in the teaching and training of radiation protection during interventions in harsh environments," in *2019 24th IEEE International Conference on Emerging Technologies and Factory Automation (ETFA)*, 2019, pp. 784–789. DOI: 10.1109/ETFA.2019.8869433.

[116] E. S. for Intelligent Manufacturing, *Cyclotron*, Accessed: 2021-03-15. [Online]. Available: esim.ac.uk/project/cyclotron.

[117] P. Dervan *et al.*, "The Birmingham irradiation facility," *Nuclear Instruments and Methods in Physics Research Section A: Accelerators, Spectrometers, Detectors and Associated Equipment*, vol. 730, pp. 101–104, 2013.

[118] P. Dervan *et al.*, "Upgrade to the Birmingham irradiation facility," *Nuclear Instruments and Methods in Physics Research Section A: Accelerators, Spectrometers, Detectors and Associated Equipment*, vol. 796, pp. 80–84, 2015.

[119] H. Marin-Reyes *et al.*, "Pre-configured xy-axis cartesian robot system for a new ATLAS scanning facility," in *Mobile Service Robots*. World Scientific, 2014, ch. 8, pp. 477–483.

[120] Microsoft, *Microsoft hololens*, Accessed: 2021-03-15. [Online]. Available: microsoft.com/en-us/hololens.

[121] Tracerco, *Personal electronic dosimeter (ped blue)*, Accessed: 2021-03-15, 2021. [Online]. Available: tracerco.com/monitors/ped-blue.

[122] Q. Fang, *Iso2mesh*, 2021. [Online]. Available: github.com/fangq/iso2mesh (visited on 08/01/2021).

[123] The MathWorks, Inc., *Matlab r2019a*, Accessed: 2021-03-15, 2019. [Online]. Available: mathworks.com/products/matlab.html.

[124] A. Cryer *et al.*, "Proof of concept for a virtual reality intervention evaluation and training platform for highly radioactive environments," vol. 1643, p. 012 202, Dec. 2020. DOI: 10.1088/1742-6596/1643/1/012202. [Online]. Available: https://doi.org/10.1088/1742-6596/1643/1/012202.

[125] PhaseSpace, *Phasespace*, Accessed: 2021-03-16, 2019. [Online]. Available: phasespace.com.

[126] A. Cryer *et al.*, "Integrating motion capture in a virtual reality intervention planning platform to study radiation protection measures for the ATLAS inner detector decommissioning," *Journal of Instrumentation*, vol. 16, no. 03, P03020, Mar. 2021. DOI: 10.1088/1748-0221/16/03/p03020.

[127] Autodesk, *Autodesk motionbuilder*, Accessed: 2021-03-16, 2019. [Online]. Available: autodesk.com/products/motionbuilder.

[128] A. Steel, "Phasespace motion capture user guide," Jul. 2019.

[129] M. Meredith and S. Maddock, "Motion capture file formats explained," *Production*, Jan. 2001.

[130] J. C. Armenteros *et al.*, "Fluka studies of dose rates in the atlas standard opening scenario," in *13th International Topical Meeting on Nuclear Application of Accelerators, AccApp'17*, 2017, pp. 62–71.

[131] D. Forkel-Wirth *et al.*, "Radiation protection aspects Proceedings, LHC Performance Workshop (Chamonix 2014): Chamonix, France, September 22-25, 2014," M. Draper, Ed., ser. CERN Yellow Reports: Conference Proceedings, Geneva: CERN, 2015, p. 276. DOI: 10.5170/CERN-2015-002.

[132] G. L. et al., "Radiation hard silicon detectors, developments by the RD48 (ROSE) Collaboration," *Nuclear Instruments and Methods in Physics Research Section A: Accelerators, Spectrometers, Detectors and Associated Equipment*, vol. 466, no. 2, pp. 308–326, 2001, 4th Int. Symp. on Development and Application of Semiconductor Tracking Detectors. DOI: 10.1016/S0168-9002(01)00560-5.

[133] B. Hiti, "Radiation Hardness of CMOS detector prototypes for ATLAS Phase-II ITk upgrade. Sevalna odpornost detektorjev CMOS za nadgradnjo notranjega sledilnika ATLAS," Presented 2020, Ph.D. dissertation, University of Ljubljana, 2020. [Online]. Available: cds.cern.ch/record/2733027.

[134] L. Ding *et al.*, "Radiation tolerance study of a commercial 65nm CMOS technology for high energy physics applications," *Nuclear Instruments and Methods in Physics Research Section A: Accelerators, Spectrometers, Detectors and Associated Equipment*, vol. 831, pp. 265–268, 2016. DOI: 10.1016/j.nima.2016.03.096.

[135] R. French *et al.*, "Evaluating the radiation tolerance of a robotic finger," in *Towards Autonomous Robotic Systems*, M. Giuliani *et al.*, Eds., Cham: Springer International Publishing, 2018, pp. 103–111.

[136] i3D Robotics, *Industrial 3d robotics*, Accessed: 2021-08-31, 2021. [Online]. Available: i3drobotics.com.

[137] S. R. Company, *Shadow robot company*, Accessed: 2021-08-31, 2021. [Online]. Available: shadowrobot.com.

[138] M. Berger *et al.*, *Estar, pstar, and astar: Computer programs for calculating stopping-power and range tables for electrons, protons, and helium ions (version 1.2.3) [online]*, Accessed: 2021-03-15, National Institute of Standards and Technology, Gaithersburg, MD., Jan. 2018. [Online]. Available: physics.nist.gov/Star.

[139] ThermoHaaKE, *Instruction manual water r2circulator kryo-thermat 45/90/140*.

[140] Leroy and Rancoita, "Electromagnetic interaction of charged particles in matter," in *Principles of Radiation Interaction in matter and detection*. World Scientific, 2016, ch. 2, p. 74.

[141] P. Zarand, "An ionization chamber system for high dose-rate-measurements in mixed n-gamma field," Hungarian Academy of Sciences, Hungary, Tech. Rep., 1973, KFKI–73-18, p. 15. [Online]. Available: inis.iaea.org/search/search.aspx?orig_q=RN:05141916.

[142] F. Ravotti, "Development and Characterisation of Radiation Monitoring Sensors for the High Energy Physics Experiments of the CERN LHC Accelerator," Presented on 17 Nov 2006, 2006. [Online]. Available: cds.cern.ch/record/1014776.